Optimization of Caesium Dynamics in Large and Powerful RF Sources for Negative Hydrogen Ions

Dissertation

zur Erlangung des akademischen Grades
Dr. rer. nat.

eingereicht an der
Mathematisch-Naturwissenschaftlich-Technischen Fakultät
der Universität Augsburg

von

Alessandro Mimo

Augsburg, Februar 2018

Universität
Augsburg
University

Vorgelegt am 07.02.2018

Tag der mündlichen Prüfung: 24.05.2018

Erste Gutachterin: Prof. Dr.-Ing. Ursel Fantz

Zweiter Gutachter: Prof. Dr. Achim Wixforth

Contents

1 Introduction

Power plants based on magnetically confined nuclear fusion plasma are a promising source to achieve a sustainable energy production in the future. These systems will rely on the fusion reaction between two hydrogen isotopes, deuterium and tritium, with the consequent production of helium nuclei, neutrons and release of energy [1].

In order to demonstrate the feasibility of this technology, the experimental tokamak reactor ITER, based on an international collaboration, is currently under construction in Cadarache, France. For the fusion reactions to occur, deuterium and tritium ions need to be heated up to high temperature (10^8 K) to overcome the Coulomb barrier. Magnetic fields are used to confine the plasma inside the toroidal vessel of the reactor. The target of ITER will be to achieve 500 MW of fusion power with an energy gain factor of 10, i.e. by using a maximum heating power of 50 MW to sustain the plasma [2].

The following step in the road map for fusion will be to build the demonstration power plant DEMO, which need to fulfil all the requirements of an industrial power plant, i.e. net electric energy production in the order of 500 MW of power with high reliability [3].

External plasma heating and current drive systems are needed in order to increase the deuterium and tritium temperature and sustain the discharge. In ITER most of the heating power will be provided by Neutral Beam Injection (NBI) [4]. Neutral Beam Injection heating relies on the injection of high energy neutral deuterium particles inside the tokamak: the energy will be transferred to the fuel by means of collisions. In addition, the injection of energetic particles can contribute to drive the toroidal current necessary for the stability of the magnetic confinement. The injected particles need to be neutral, in order to be able to penetrate across the magnetic field inside the reactor.

The generation of the high energy neutral beam is presently based on the neutralisation of an accelerated ion beam by means of a gas neutraliser. Positive ion based sources are nowadays the standard technology for neutral beam injection, but they are not suitable for the required beam energy for ITER, i.e. 1 MeV in D. At this energy the neutralisation efficiency of negative ions for an optimized gas neutraliser is around 60% whereas for positive ions is negligible, therefore the ITER-NBI source needs to rely on negative D^- ions. However, the generation of negative ions is technically more challenging than the case of positive ions due to the low binding energy of the additional electron. An additional difficulty that needs to be faced in negative ion sources is that together with negative ions, also electrons from the plasma are extracted. The amount of co-extracted electrons needs to be limited to avoid an excessive heat load on the second grid of the acceleration system, where the electrons are dumped before being fully accelerated. In order to achieve the high negative ion current (48 A) that has to be delivered by the ITER-NBI negative ion source, the most efficient way of negative ion production have to be chosen, i.e. the surface conversion of neutral atoms and positive ions (generated in a low temperature plasma environment) on a low work function surface.

At present, negative ion sources are based on the evaporation of Cs inside the source, which is deposited on the converter surface (typically Mo, W). The deposited Cs reduces the work function of the surface and increases the negative ion production yield [5]. The stability of the work function of the converter surface is fundamental to maintain a high negative production yield and consequently a high negative ion extracted current for the required time up to one hour.

A Radio Frequency (RF) prototype negative hydrogen ion source with a size of $0.6\,\mathrm{m} \times 0.3\,\mathrm{m}$ (1/8 of the ITER-NBI source) has been developed at IPP in Garching [6] and it has been chosen as the reference design for the ITER-NBI source [7]. The ITER requirements for the negative ion current density and the ratio of co-extracted electrons to ions have been successfully achieved with the prototype source at the BATMAN test facility. Another source is currently in operation at the ELISE test facility, with a size of $0.9\,\mathrm{m} \times 1\,\mathrm{m}$ (1/2 of the ITER-NBI source). The ELISE test facility is capable of performing long plasma pulses up to 1 hour with pulsed extraction (i.e. 10 s extraction phases every 150 s). The aim of this test facility is to verify the feasibility of the ITER requirements concerning the negative ion extracted current and the co-extracted electrons for a large beam ($1000\,\mathrm{cm}^2$) and in long pulses (hundreds of seconds).

The usage of caesium in these sources poses many issues in terms of control and stability of the source performance. Cs dynamics, i.e. the redistribution of Cs in the source and its interaction with the source surfaces, is in fact very complex in negative ion sources and depends on the operative regime. The source operates in a pulse mode with two phases: the vacuum phase in which no plasma is present (background pressure of $\sim 10^{-5}$ Pa, typical time of the order of minutes) and the plasma phase, in which the discharge takes place (pressure of 0.3 Pa, typical time from seconds for the prototype source at BATMAN up to one hour at ELISE). Cs is continuously evaporated in the source in both phases by means of Cs ovens, in which the evaporation rate can be adjusted by setting the temperature of a liquid Cs reservoir, i.e. the vapour pressure. The Cs deposited during a vacuum phase can leave the surface due to thermal desorption and plasma assisted removal (via chemical and physical sputtering): the removed Cs is then redistributed by means of collisions with the background gas and the plasma particles.

Due to the vacuum conditions, which are far from ultra-high vacuum, and to the high reactivity of Cs, the formation of stable Cs compounds with the background particles (such as hydrogen, oxygen and water) occurs. This can lead to a degradation of the work function of the converter surface if a sufficient Cs flux onto the surface is not maintained during the plasma phase: instability or spatial inhomogeneity of the Cs flux onto the surfaces can be related to instability or inhomogeneity of the work function and then of negative ion production. The knowledge of how the Cs flux onto the plasma grid is affected by the plasma parameters (plasma density and potential, electron temperature) and by the source operative parameters (pulse time and duty cycle) is crucial to achieve a high reliability.

A consistent and complete understanding of all the phenomena driving the Cs dynamics is yet to be achieved. The identification of the knobs which allow for a better management of the source caesiation can be achieved by using numerical simulations in comparisons with experimental measurements.

The Monte Carlo test particle code CsFlow3D was developed in 2009 at IPP to perform simulation of Cs transport and redistribution in a negative ion source [8]. To study the transport of Cs the full source geometry needs to be considered. The code simulates the evaporation of Cs and its consequent deposition on the source surfaces as well as the redistribution due to the plasma. CsFlow3D allows for the calculations of the Cs fluxes and coverage on the inner surfaces of the source. This numerical tool can be therefore used to simulate different operative scenarios, such as different duty cycles of the source operations, different Cs evaporation configurations and to study the effect of the plasma parameters (e.g. plasma density and temperature profiles) and the surface condition (e.g. adsorption and reflection probability of Cs) on Cs dynamics. Preliminary simulations were performed for the prototype source and important qualitative insights on Cs dynamics were obtained [9].

The purpose of this work is in a first stage to quantitatively benchmark the code against the experimental data of the prototype source at the BATMAN test facility. To perform this benchmark the code needs to be updated with the possibility of calculating neutral Cs density, which can be directly measured in the experiments. In a second stage, the simulation domain is extended to the larger negative ion source at the ELISE test facility, for which besides the general benchmark also predictions are made.

The results of these studies are needed to develop a recipe for an efficient and optimized caesiation of the source, i.e. the maintenance of a stable Cs flux to avoid the work function degradation of the converter surface. A better Cs management (e.g. optimal duty cycle, Cs evaporation configuration) will help also to reduce the Cs consumption and therefore the maintenance requirement of the NBI-sources, which is fundamental both for the case of ITER and of the industrial scale power plants such as DEMO.

Another important aspect is the scalability towards the full size ITER-NBI source with continuous extraction. For these investigations the CsFlow3D code can act as predictive tool. First results for the full size source are presented, with particular attention on the effect of the size scaling and of the different Cs oven nozzle configuration on the Cs consumption, in comparison with the ELISE test facility.

2 Negative ion sources for fusion

A future nuclear power plant will rely on the fusion reaction between deuterium and tritium for the production of energy:

$$\mathrm{D} + \mathrm{T} \longrightarrow {}^{4}\mathrm{He}\,(3.5\,\mathrm{MeV}) + \mathrm{n}\,(14.1\,\mathrm{MeV}) \tag{2.1}$$

in which a ^{4}He nucleus and a neutron are produced. Most of the fusion energy (14.1 MeV out of the total 17.6 MeV) is delivered to the neutron. By observing the plot in figure 2.1, which shows the reaction rates of three different fusion reactions (i.e. D+D, T+T and D+^{3}He) as a function of temperature, it can be noticed that the chosen D-T reaction is the one with highest reaction rate at the lowest temperature. In order to have a reaction rate high enough to produce a sufficient amount of energy, a high temperature is needed (~ 20 keV). At this temperature deuterium and tritium are completely ionized and the gas mixture is in the plasma state. Strong magnetic fields

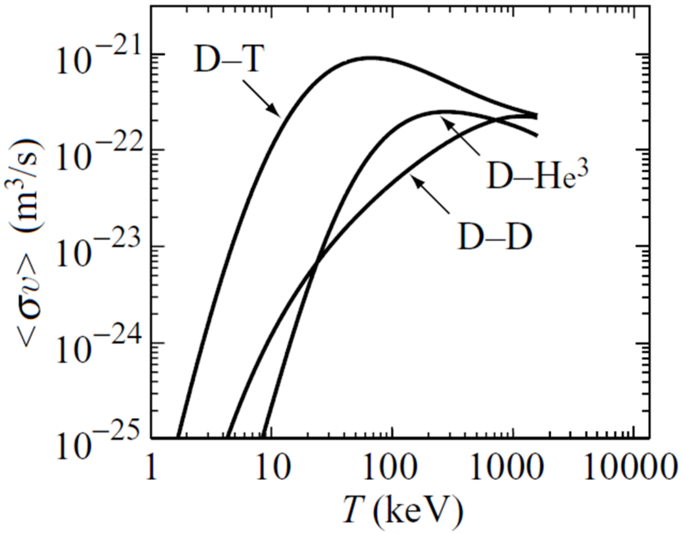

Figure 2.1: Reaction rate $\langle\sigma \mathrm{v}\rangle$ as function of temperature for different fusion reactions: deuterium-deuterium (D-D), deuterium-tritium (D-T) and deuterium-helium (D-^{3}He) [10].

are needed in order to increase the confinement time of the plasma. Plasma heating mechanisms are needed for the achievement of the required plasma temperature.

A good confinement of the plasma can be reached inside a torus-shaped vessel by means of magnetic fields both in toroidal and poloidal direction. Two possible configurations of such a machine were developed: the stellarator and the tokamak [1]. In the first case the complex magnetic field structure is generated solely by external coils: a sketch of a possible configuration can be seen in figure 2.2 (a). In the case of the tokamak, schematised in figure 2.2 (b), the external coils provide only the toroidal magnetic field (with a typical strength of some T), while the poloidal field is generated by means of a toroidal current flowing, from several kA up to MA. The plasma is in fact used as the secondary coil of a transformer, with the primary being a coil in the center of the torus. By ramping up a current in the primary coil, a toroidal current is induced in the plasma. Since the current on the primary coil cannot be increased or decreased indefinitely, this system does not allow for continuous operations.

The ITER experiment is based on the tokamak configuration and the size of the torus will be 6.2 m for the major radius and 2 m for the minor radius. Three experimental phases are foreseen for the ITER operations: at the beginning the non-nuclear phase using hydrogen plasma, in order to run the first test of the machine in a non-nuclear environment, further on the deuterium phase and finally the deuterium-

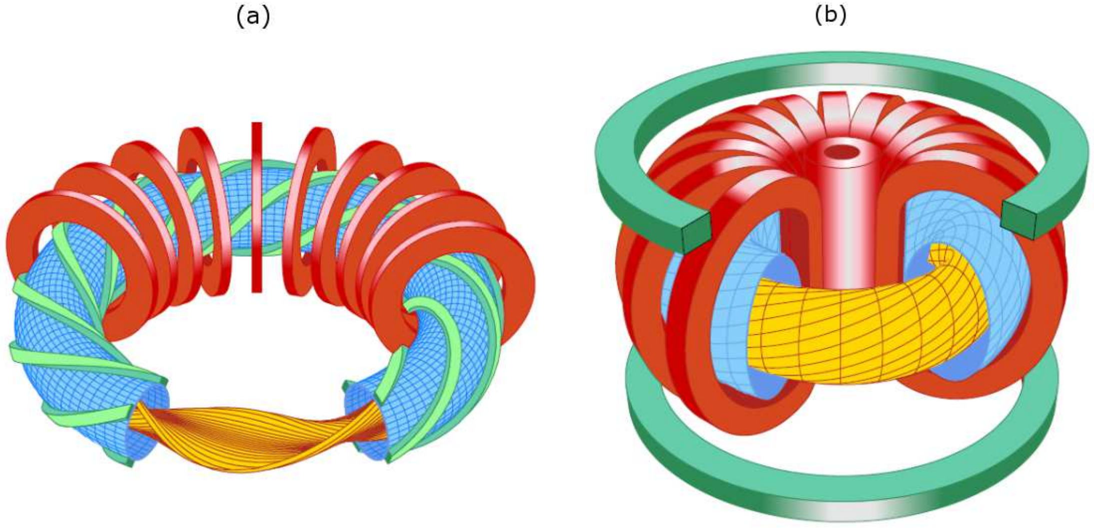

Figure 2.2: (a) Schematic of a stellarator: the complex coil system generates both the toroidal and poloidal component of the magnetic field; (b) Schematic of a tokamak: the coils for the generation of the toroidal magnetic field as well as the primary coil in the center are shown.

tritium operations. The target of ITER for the deuterium-tritium operations is to reach a fusion energy gain factor equal or greater than 10, i.e. to obtain a total fusion power of 500 MW by using a maximum heating power of 50 MW. In order to reach the temperature needed for a sufficient fusion reaction rate, plasma heating systems are needed. One intrinsic heating mechanism of the plasma inside a tokamak is the Ohmic heating due to the toroidal current up to 15 MA. This system is anyway not sufficient to heat up the plasma to the desired temperature. The Joule dissipation is proportional to the plasma resistivity, which decreases with increasing temperature: therefore the efficiency of the Ohmic heating strongly decreases with increasing temperature. For this reason also external heating systems need to be used.

Most of the heating power (i.e. 33 MW [4]) is deposited to the plasma by means of Neutral Beam Injection (NBI), i.e. the injection of high energetic neutral particles which transfer their energy and momentum through collisions. By exploiting tangential injection, NBI can also be used in order to drive part of the toroidal current needed for generating the poloidal magnetic field: NBI is therefore useful to increase the pulse length, from hundreds of seconds to steady state operations.

The NBI systems for ITER can either be operated in hydrogen or deuterium: operations will be in hydrogen during the first operative phase of ITER, while during D-D and D-T operations, deuterium will be used.

2.1 Neutral beam injection for ITER

The injection of an energetic neutral beam delivers power to the fusion plasma by means of collisions. The beam needs to be neutral in order to penetrate into the plasma core through the magnetic confinement field. Once the fast neutral particles (hydrogen or deuterium) collide with either the electrons or the ions in the plasma, they can get ionised:

$$\mathrm{H}^0_{\mathrm{fast}} + \mathrm{e}^- \longrightarrow \mathrm{H}^+_{\mathrm{fast}} + 2\mathrm{e}^- \tag{2.2}$$

$$\mathrm{H}^0_{\mathrm{fast}} + \mathrm{H}^+ \longrightarrow \mathrm{H}^+_{\mathrm{fast}} + \mathrm{H}^+ + \mathrm{e}^- \tag{2.3}$$

Another relevant reaction that can form fast positive ions is the charge exchange collision:

$$\mathrm{H}^0_{\mathrm{fast}} + \mathrm{H}^+ \longrightarrow \mathrm{H}^+_{\mathrm{fast}} + \mathrm{H}^0 \tag{2.4}$$

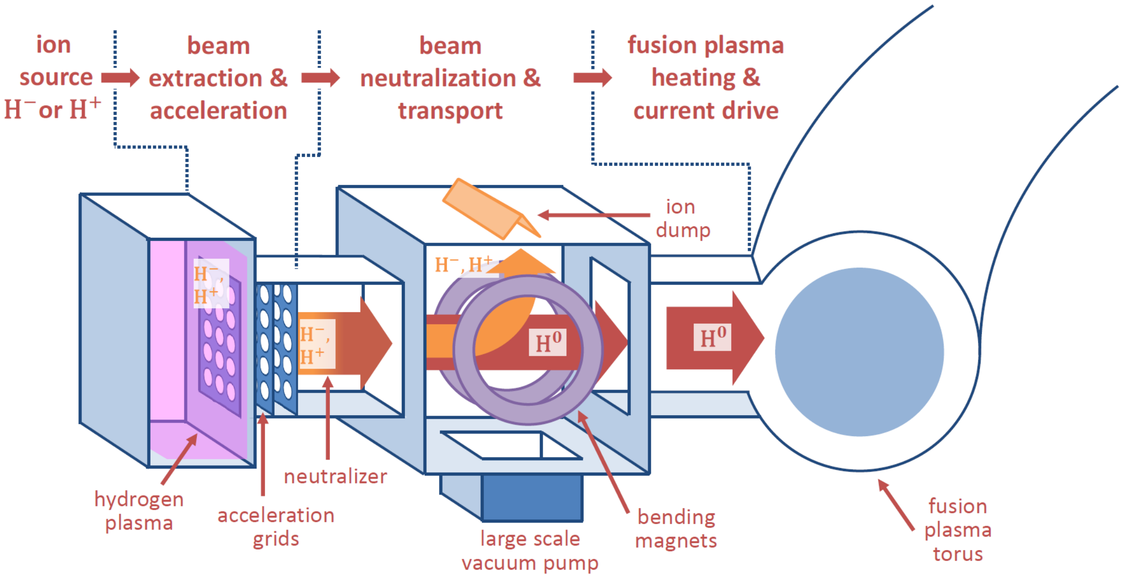

Figure 2.3: Schematic of a Neutral Beam Injector (NBI), with the different stages indicated, i.e. the ion source, the acceleration and the neutralization.

The mean free path of these collisions determines the penetration depth of the neutral beam. In order to reach the plasma core, the required neutral beam energy mostly depends on the cross sections of the ionisation processes, the plasma density and temperature and the dimension of the reactor. In case of the JET tokamak, with a plasma density of $\sim 3 \cdot 10^{19}\,\mathrm{m}^{-3}$ and a minor radius of $\sim 1\,\mathrm{m}$, the energy needed for the NBI is between 100 and 200 keV [10]. In the case of a fusion reactor plasma such as ITER, with a foreseen plasma density higher than that of JET, i.e. $\sim 15 \cdot 10^{19}\,\mathrm{m}^{-3}$ and a double minor radius, i.e. $\sim 2\,\mathrm{m}$, the required energy is of the order of several hundreds of keV. In order to enhance also the current drive efficiency, the beam energy for which the ITER-NBI systems are designed is 1 MeV [11].

Figure 2.3 shows a schematic of a NBI system for a fusion device. The system consists basically of three main parts: an ion source, an accelerator which accelerates the ions to the desired energy and finally the gas neutraliser, in which the ions are neutralised by collisions and the remaining charged particle are bent by magnets and dumped. The ion source can in principle be either a positive or negative ion source: the criterion to choose which one is suitable for the case of the ITER-NBI is given by the neutralisation efficiency at the required acceleration energy. The plot in figure 2.4 shows the neutralisation efficiency of both positive and negative hydrogen/deuterium ions for an optimised gas neutraliser as a function of energy. At higher energies, the neutralisation efficiency for positive ions is almost zero, therefore the only solution is

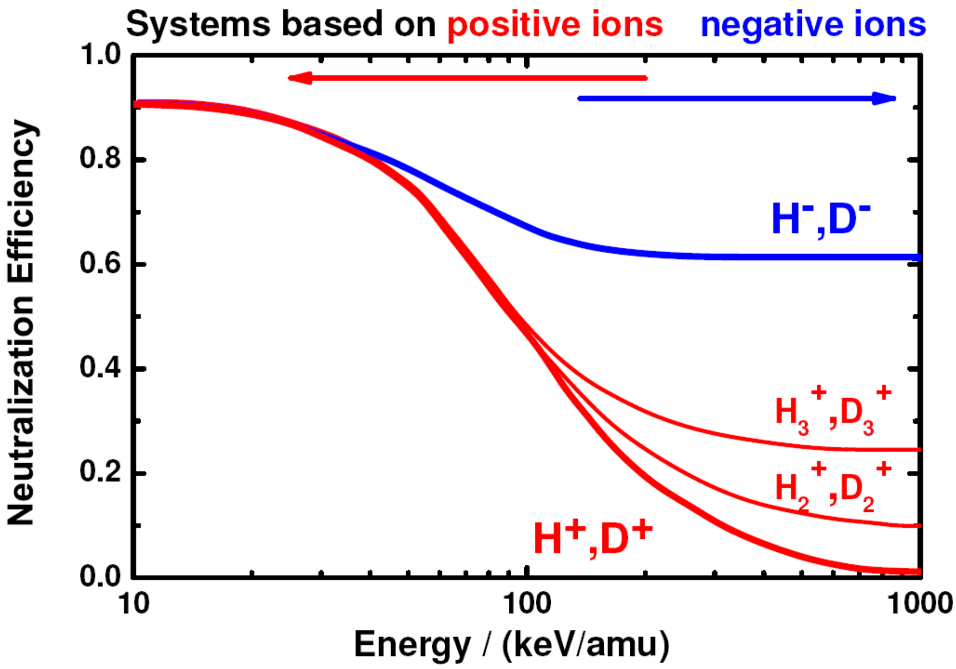

Figure 2.4: Comparisons of the neutralization efficiency by means of an optimized gas neutralizer as a function of energy for positive and negative ions [12].

the usage of negative ion sources.

There are however two major drawbacks of the usage of negative ions with respect to positive ions in order to generate a high current and high energy beam:

- the binding energy of the second electron in a negative hydrogen/deuterium ion is very low (0.75 eV) [13], which leads to a high destruction probability due to electron detachment;
- electrons from the plasma are co-extracted together with negative ions, since they have the same charge. These electrons need to be bent and dumped before fully accelerating them, in order to avoid dissipating power for the acceleration of unwanted species. The thermal load on the surfaces where electrons are dumped poses a strict limit on the acceptable amount of co-extracted electrons.

The generation and destruction processes of negative ions will be described in detail in section 2.2.

Two different source technologies are in use at present for neutral beam injection, for both positive and negative ions: arc sources and Radio Frequency (RF) sources. The main difference is the mechanism of plasma generation. Arc sources rely on thermionic emission of electrons from hot tungsten cathode filaments: by biasing the

	Hydrogen	**Deuterium**
Power	16.7 MW	16.7 MW
Particle energy	0.87 MV	1 MV
Extraction area	2000 cm^2	2000 cm^2
Extracted current density	330 $\mathrm{A/m}^2$	286 $\mathrm{A/m}^2$
Accelerated current	46 A	40 A
Co-extracted electrons to ions ratio	<1	<1
Source pressure	≤0.3 Pa	≤0.3 Pa
Pulse length	1000 s	3600 s
Beam inhomogeneity	<10%	<10%

Table 2.1: Requirements for each ITER neutral beam injector in hydrogen and deuterium [4].

filaments negatively w.r.t. the source (∼100 V), these electrons ionise the gas in the chamber and generate the plasma [14]. The main disadvantage of this kind of source is the need for frequent maintenance, such as the substitution of the exhausted tungsten filaments. In the RF sources the plasma is generated by via inductive coupling by means of radio frequency coils [15]. In this case less maintenance is needed also thanks to the fact that the coils are located outside the source.

The ITER-NBI source for plasma heating and current drive will be an RF negative ion source: the negative ions will be extracted and accelerated up to 1 MeV of energy by means of a seven multi-aperture-grid system (an extraction stage at 10 kV and five accelerating stages at 200 keV each). The grids consist of 1280 apertures of 14 mm diameter, for a total extraction area of 2000 cm^2. The target for the extracted current in D (H) is 57 A (66 A) at 1 MeV (0.87 MeV) of energy. The beam needs to be delivered for up to 3600 s in deuterium, with an inhomogeneity of the extracted current below 10%. The limit for the co-extracted electron current density $j_\mathrm{e} \leq j_{\mathrm{H}^-}$ is given by the thermal heating limit of the grid where co-extracted electrons are dumped. The source pressure needs to be ≤ 0.3 Pa in order to limit the electron stripping inside the accelerator. The table 2.1 summarizes these requirements [4].

Negative ion based NBI systems have been routinely used at LHD[1], with a nominal injection energy of 180 keV [16], and at JT60-Upgrade[2], with a maximum achieved energy of 416 keV [17]. The feasibility of 1 MeV acceleration energy for negative ions have been proven at the MeV accelerator in Japan, but for pulse length and extracted current still below those required for the ITER-NBI [18].

---

[1] Large Helical Device

[2] Japan Torus

In order to investigate the feasibility of the ITER-NBI requirements for the RF negative ion source and to test and improve this technology, two test facilities are in operation at IPP Garching:

- the **BATMAN**[3] test facility in which a RF prototype source for negative ions (1/8 of the ITER-NBI source size) is installed. This source has been developed at IPP Garching [6] and became the reference for the design of the ITER-NBI source [4]. The test facility is designed to run short plasma pulses up to $\sim$ 7 s (due to limitation in the HV power supply and vacuum systems), with a maximum RF power of 150 kW and a maximum negative ion energy of 22 kV. A detailed description of BATMAN will be given in section 2.3.1;
- the **ELISE**[4] test facility with a source which is half of the ITER-NBI source size [19] (beginning of operation in 2013). The source is designed for plasma operation up to one hour with pulsed extraction (i.e. 10 s of beam extraction every 150 s). The target of ELISE is to verify the feasibility of the ITER requirements for the negative ion current density and co-extracted electron current density, in a large beam (extraction area of 1000 cm^2) and in long pulses. Section 2.3.2 will give a detailed description of ELISE.

Figure 2.5 shows the size scaling of the two negative ion sources at the test facilities BATMAN and ELISE in comparison with the source for the ITER-NBI. Investigations on the full size source will be carried on at the test facilities PRIMA[5], currently under construction at Consorzio RFX (Padova, Italy) [20]. PRIMA consists of two experiments: SPIDER[6] (start of operations foreseen for 2018), a full size ITER-NBI RF negative ion source, designed for CW extraction operations with acceleration energy up to 100 keV and which will be dedicated to the optimization of the full size ion source by means of several diagnostics and MITICA[7](operative in 2022), the full 1:1 prototype of heating neutral beam injector of ITER with 1 MeV acceleration together with the beam neutraliser.

---

[3] BAvarian Test MAchine for Negative ions

[4] Extraction from a Large Ion Source Experiment

[5] Padova Research on ITER Megavolt Accelerator

[6] Source for Production of Ion of Deuterium Extracted from RF plasma

[7] Megavolt ITER Injector & Concept Advancement

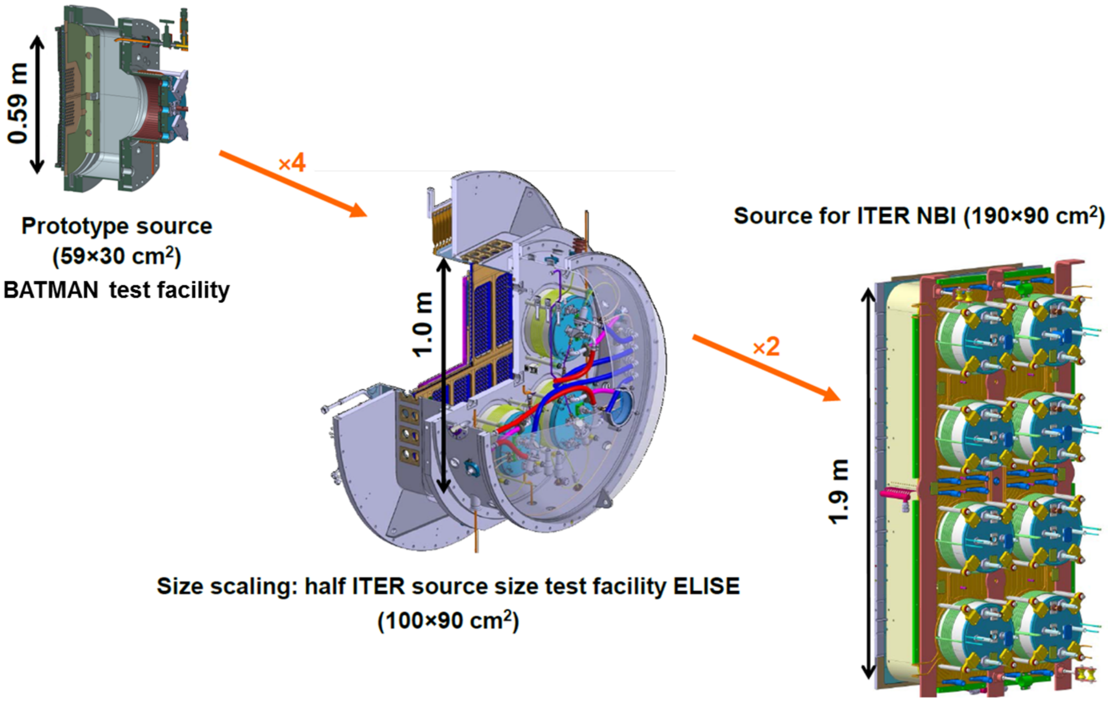

Figure 2.5: Schematic showing the size scaling between the test facilities in operation at IPP, i.e. the prototype source at BATMAN (1/8 of the ITER-NBI souce size) and ELISE (half the ITER-NBI source size) and the full source for ITER.

2.2 Negative ion generation and destruction processes

There are basically two processes that contribute to negative ion generation in a low temperature plasma environment: volume production [21] and surface production [5].

Volume production

The volume production of negative hydrogen ions relies on the dissociation of molecular hydrogen in a high vibrational state ν by means of collisions with electrons (dissociative attachment) [22]:

$$H_2\,(\nu) + e^- \longrightarrow H^- + H. \tag{2.5}$$

The efficiency of the dissociative attachment depends both on the vibrational state of the molecule and on the electron temperature [23]. Figure 2.6 (a) shows the peak value of cross section of dissociative electron attachment both for hydrogen and deuterium molecules as a function of the vibrational quantum number ν (data taken from [24]). It can be seen that for higher vibrational states the cross section is considerably

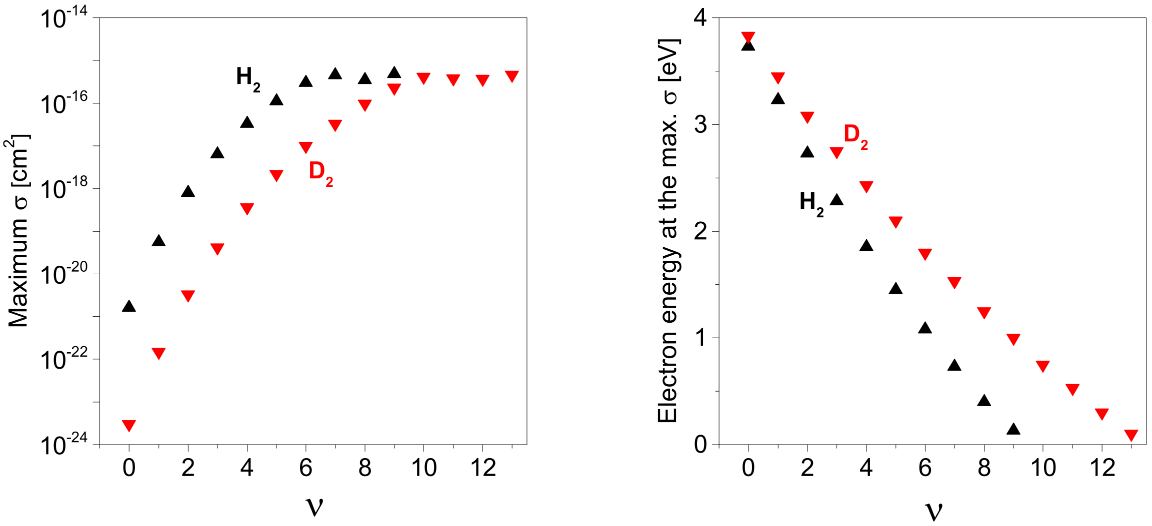

Figure 2.6: (a) Maximum cross section of dissociative attachment as a function of the vibrational quantum number of the H_2 (D_2) molecule and (b) electron energy at which the cross section is maximum [24].

higher ($\nu \geq 5$ for H and $\nu \geq 8$ for D). The electron energy at which the cross section is maximum is shown in figure 2.6 (b), again as a function of the vibrational state for both H_2 and D_2 molecules. Therefore, an efficient volume production of negative ions occurs for electron temperature below 1 eV (assuming a Maxwellian EEDF).

On the other side, the excitation of the hydrogen molecule to high vibrational states is achieved by means of collision with electrons at $T_e \geq 5$ eV:

$$H_2 + e^- \longrightarrow H_2(\nu) + e^- . \tag{2.6}$$

A source that relies on negative ion volume production needs therefore two different plasma regimes: one with high electron temperature for the population of the high vibrational states of the hydrogen molecule, and another with low electron temperatures for the dissociative attachment and the generation of the negative ions. Volume production H^- sources of this kind were developed for example at the Lawrence Berkeley Laboratory, University of California [25] or at the Deutsches Elektronen-Synchrotron DESY [26]. Since the species needed for the generation of the negative ions according to the reaction (2.5) and (2.6) are H_2 and e^-, the efficiency of the process increases for increasing molecular hydrogen density and electron density. An high molecular hydrogen density means high pressure, which is incompatible with the pressure requirement for the ITER-NBI, i.e. below 0.3 Pa. In addition, the drawback of operating at a high electron density is the significative amount of co-extracted

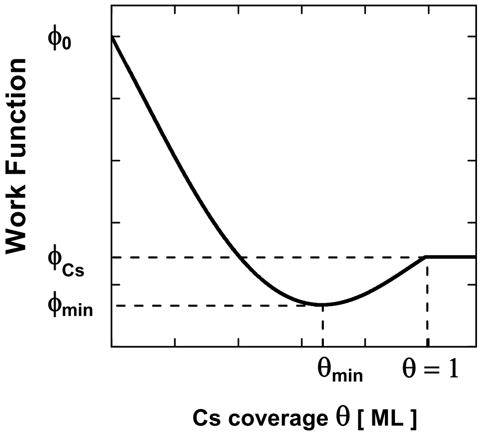

Figure 2.7: Work function of a caesiated metal as a function of the Cs coverage.

	ϕ_0(eV)	ϕ_{min}(eV)
C	4.39	1.67
W	4.52	1.62
Ni	4.47	1.49
Cu	4.47	1.58
Mo	4.27	1.62

Table 2.2: Values of ϕ_0 und ϕ_{min} for different caesiated metals [28].

electrons: such a source could not fulfil the requirements of ITER-NBI sources of table 2.1 (high negative ion current density with low co-extracted electron current density). Negative ion sources for neutral beam injection at ITER need therefore to rely on another production system which exploits surface processes.

Surface production

Another production method of negative ions is based on a surface effect: an electron from the Fermi level of a metallic surface can be transferred to the electron affinity level of an atom by quantum tunnelling:

$$\mathrm{H} + \mathrm{e}^-_{\mathrm{surface}} \longrightarrow \mathrm{H}^-. \tag{2.7}$$

Also positive ions can be converted into negative ions by means of a two-step process:

$$\mathrm{H}^+ + \mathrm{e}^-_{\mathrm{surface}} \longrightarrow \mathrm{H} + \mathrm{e}^-_{\mathrm{surface}} \longrightarrow \mathrm{H}^-. \tag{2.8}$$

At first the positive ion is neutralized and successively converted into a negative ion via the same process of formula (2.7).

The probability p that an atom with electron affinity E_a is converted to a negative ion by surface process depends exponentially on the difference between E_a and the work function ϕ of the metal surface [27]. A decrease of the work function of the metal will therefore enhance the efficiency of the surface conversion.

The element with the lowest work function is Cs, with $\phi = 2.14\,\mathrm{eV}$ [29]. However, Cs cannot be used as a bulk material for the production of a converter surface, due to its very low melting point at 28°C [30] and its high reactivity. Cs is therefore evaporated in the source: the deposition of Cs on the converter surface allows for a reduction of the work function and a consequent enhancement of the negative ion production yield. The work function of a metal coated with Cs depends on the Cs coverage and can be reduced to a value even below that of pure Cs in case of a sub-monolayer Cs coverage. Figure 2.7 shows the work function ϕ of the metal surface in dependence of the Cs overage θ expressed in monolayers (ML). An increase of the Cs coverage decreases the work function of the surface down to a minimum value ϕ_{min} at θ_{min}. By increasing further the coverage, the work function increases up to the one of bulk Cs, for multilayers coverage (i.e. $\theta \geq 1$ monolayer). The minimum achievable work function can be estimated by the empirical formula [28]:

$$\phi_{\mathrm{min}} = 0.62\,(V_{\mathrm{i}} + E_{\mathrm{a}}) - 0.24\phi_0 \tag{2.9}$$

where V_{i} and E_{a} are respectively the first ionization potential and the electron affinity of Cs atoms, while ϕ_0 is the work function of the metal substrate. In the case of Cs $V_{\mathrm{i}} + E_{\mathrm{a}}$ equals 4.35 eV, the smallest of all the elements. The minimum achievable work function is ~ 1.5 eV at a partial Cs coverage between 0.5 and 0.7 monolayers. These values slightly depends on the metal substrate, whether it is amorphus or with some specific crystal orientation. Table 2.2 lists the value of ϕ_0 and ϕ_{min} for different caesiated metal substrate.

In negative ion sources based on surface conversion, Cs is evaporated inside the source from a liquid Cs reservoirs by means of a specific Cs oven: Cs evaporation will be described in section 3.3. A detailed description of Cs properties will be given in chapter 3.1.

Since the generation of negative hydrogen ions relies mostly on the conversion of atomic hydrogen, the dissociation of the hydrogen molecules into hydrogen atoms is fundamental to ensure a sufficient flux of atomic hydrogen onto the converter surface. A higher electron temperature is helpful to increase the dissociation of the hydrogen molecules, but it has the drawback of increasing the destruction probability of the negative ions by means of electron stripping.

Similarly to sources based on volume production, surface production sources are therefore based on the tandem concept, i.e. they consists of two regions: the one where the plasma is generated with a higher electron temperature (~ 10 eV) in order to enhance the dissociation of the molecules, and the region where the negative ions are produced in which the electron temperature is lower (~ 1 eV), so to limit the destruction process. The cooling of the electrons is achieved by means of a magnetic filter field.

Negative ion distruction processes

The low binding energy of the additional electron to the negative hydrogen ion leads to a high destruction probability. The negative ions can be destructed via different processes, which are reported in table 2.3: the rate coefficient of these processes are plotted in figure 2.8 as a function of electron temperature for reaction (1) and of the negative ion temperature for the others.

Electron stripping is the most effective destruction process in the case of electron temperature $T_e > 2\,\text{eV}$: a low electron temperature is needed in the region where negative ions are produced in order to limit the stripping.

By considering the rate coefficient, the other relevant processes at the typical energy of negative ions ($\sim 1\,\text{eV}$) are the mutual neutralisation, both due to the positive hydrogen (2) and caesium ions (3), and the associative/collisional detachment due to the atomic hydrogen (4)+(5). Despite the rate coefficient is higher for the mutual neutralisation processes (2) and (3) than the associative detachment (4), the latter is dominant due to the higher density of atomic hydrogen w.r.t. the density of positive hydrogen or caesium ions. As a matter of fact in these kind of sources the density of atomic hydrogen ($n_H \sim 10^{19}\,\text{m}^{-3}$) is at least two order of magnitudes higher than that of positive hydrogen ions ($n_{H^+} \sim 10^{17}\,\text{m}^{-3}$) and of caesium ions ($n_{Cs^+} \sim 10^{15}\,\text{m}^{-3}$) [32]. In the case of surface process production, in which a high density of atomic hydrogen is necessary for the surface conversion, the collisional detachment with H is an unavoidable destruction process that cannot be reduced.

Electron stripping	$H^- + e^- \longrightarrow H + 2\,e^-$	(1)
Mutual neutralization	$H^- + H_x^+ \longrightarrow H + H_x$	(2)
	$H^- + Cs^+ \longrightarrow H + Cs$	(3)
Associative detachment	$H^- + H \longrightarrow e^- + H_2$	(4)
Collisional detachment	$H^- + H \longrightarrow e^- + 2\,H$	(5)
	$H^- + H_2 \longrightarrow e^- + H + H_2$	(6)

Table 2.3: Negative ion destruction processes.

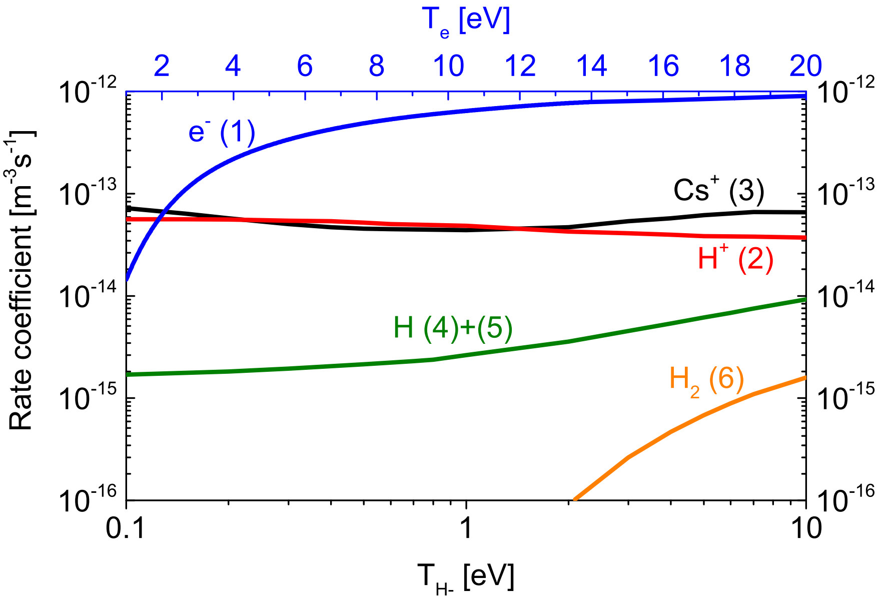

Figure 2.8: Rate coefficient for destruction processes of negative hydrogen ions with different collision partners as a function of the electron temperature (for collision with electrons) or of the negative ion temperature (see table 2.3). For reaction (1) $T_{\mathrm{H}^-} = 0.8\,\mathrm{eV}$, for reactions (2)-(6) $T_{\mathrm{H}^+}, T_{\mathrm{H}} = 0.8\,\mathrm{eV}$, $T_{\mathrm{H}_2} = 0.1\,\mathrm{eV}$. Cross sections from [31].

2.3 Radio-frequency driven ion sources

The sources that have been identified for the ITER-NBI will be RF sources which will rely on surface production of negative hydrogen and deuterium ions. In this section a detailed description of the negative ion sources developed by IPP Garching and in operation at the two test facility BATMAN and ELISE will be presented.

2.3.1 Prototype source at the BATMAN test facility

The IPP prototype source at the BATMAN test facility is an RF negative ion source with a size of 1/8 of the ITER-NBI source. It was developed at IPP Garching with the aim to study the negative ion source technology for neutral beam injection. Thanks to the flexible access for diagnostics, the source can provide a better understanding of the plasma dynamics, including H^- production, transport and extraction.

The main operative parameters of the test facility are reported in table 2.4 and figure 2.9 shows a vertical section of the source. From left to right four main regions can be identified, where different processes take place: the driver, the expansion region, the converter surface (plasma grid) and the extraction and acceleration system.

The plasma is generated in a cylindrical driver (diameter of 24.5 cm and 16.6 cm in length) by inductive coupling with a RF coil. The typical plasma parameters in the driver are $n_\mathrm{e} \sim 10^{18}\,\mathrm{m}^{-3}$ and $T_\mathrm{e} \sim 10\,\mathrm{eV}$: at this parameters the dissociation of H_2 into atomic hydrogen, which is needed for the production of negative ions, can occur. The achievable dissociation degree $n_\mathrm{H}/n_{\mathrm{H}_2}$ can be up to 0.4 [33].

The electron temperature of the driver is too high to significantly limit the destruction of negative ions by means of the electrons stripping (explained in section 2.2): the plasma is therefore allowed to expand and cool down in the so called expansion region. This region consists of a chamber with a volume of $30 \times 60 \times 25\,\mathrm{cm}^3$: a diagnostic flange is attached on the opposite side of the expansion chamber w.r.t. the driver, as visible in the figure. The plasma parameters measured in the driver and close to the PG are reported in table 2.5.

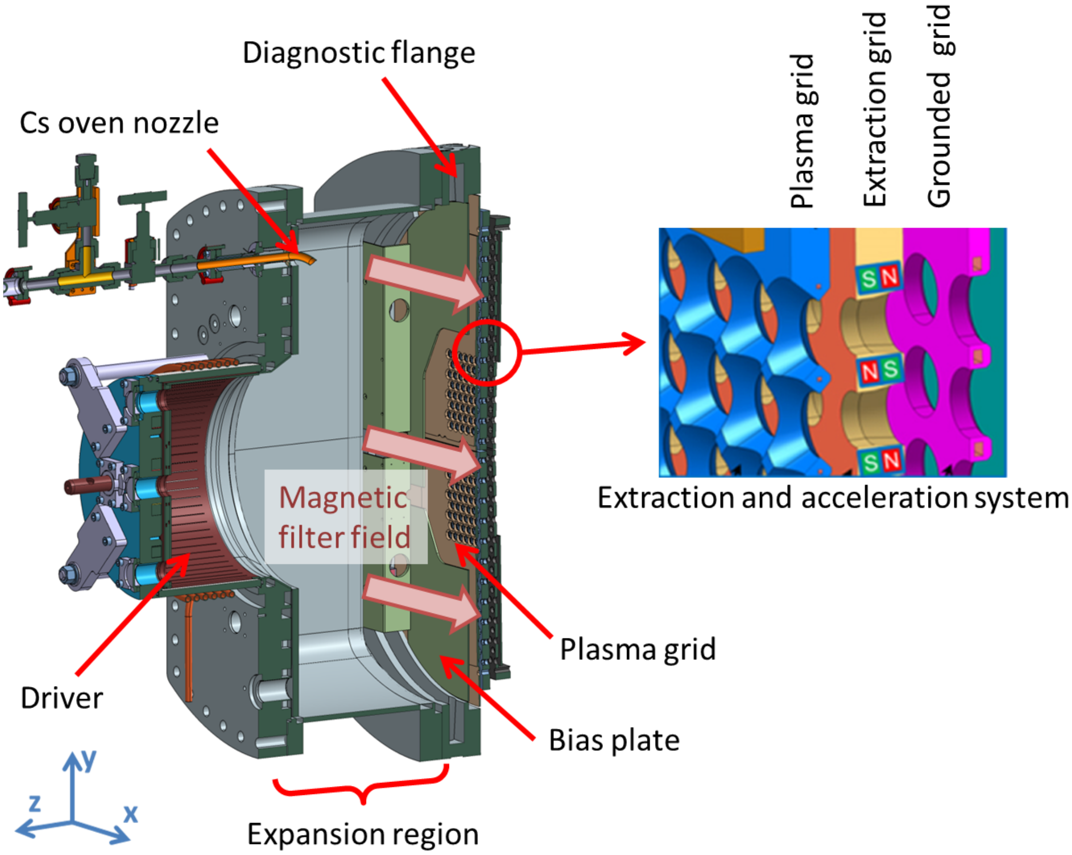

Figure 2.9: Vertical cut of the prototype source at the BATMAN test facility.

	BATMAN
Maximum RF power	150 kW
RF frequency	$\sim$ 1 MHz
Total acc. voltage	22 kV
Plasma phase length	$\leq$ 7 s
Beam phase length	$\leq$ 4.5 s

Table 2.4: Operative parameters of the BATMAN test facility.

The high temperature electrons coming from the driver are cooled down by means of a magnetic filter field, which needs to be perpendicular to the beam direction. The filter field is generated by permanent magnets, which can be installed either inside the diagnostic flange (standard configuration) or outside the expansion chamber, where they can be moved axially along the z-axis. The permanent magnets generate a horizontal magnetic field: the strength of the field close to the centre of the PG is$\sim$ 8 mT, as it is shown in detail in appendix B.

The presence of the horizontal magnetic fielter field can cause $\mathrm{E} \times \mathrm{B}$ drifts as well as diamagnetic drifts, which can lead to a vertical asymmetry of the plasma distribution inside the source: this asymmetry has been observed experimentally in the prototype source [34, 35] and also in numeric simulations [36]. Figure 2.10 shows the characteristic curve of two Langmuir probes placed on the top and on the bottom of the diagnostic flange. The measurements were performed after the caesiation of the source. A high vertical asymmetry in plasma density is observed: in the top the density is $\sim 10^{17}\,\mathrm{m}^{-3}$, while in the bottom is more than six times lower, i.e. $\sim 1.6 \cdot 10^{16}\,\mathrm{m}^{-3}$.

Atomic hydrogen as well as positive hydrogen ions is converted into negative ions by surface conversion on a metallic multi-aperture grid, the plasma grid (PG). The PG consists of 126 chamfered apertures with a diameter of 8 mm, for a total extraction area of $63.3\,\mathrm{cm}^2$. In the region close to the PG both plasma density and electron temperatures are reduced to $n_{\mathrm{plasma}} \sim 10^{17}\,\mathrm{m}^{-3}$ and $T_{\mathrm{e}} \sim 1\,\mathrm{eV}$.

A metal plate called *bias plate* is placed around the PG at a distance of 10 mm. The *bias plate* is electrically connected to the source body, while the plasma grid is instead isolated from the source. The PG grid can be positively biased w.r.t. the source up to tens of volts of potential difference. By biasing the PG w.r.t to the source and the *bias plate*, the fluxes of charged particles onto the PG surface can be changed: this was proven to be beneficial in order to decrease the amount of co-extracted electrons [6].

Parameter	**Driver**		**Ext. boundary layer**
Positive ion density $n_{H_x^+}$	$\sim 10^{18}\,\mathrm{m}^{-3}$		$\sim 10^{17}\,\mathrm{m}^{-3}$
Negative ion density n_{H^-}			$\sim 10^{17}\,\mathrm{m}^{-3}$
Electron density n_{e}	$\sim 10^{18}\,\mathrm{m}^{-3}$		$< 10^{17}\,\mathrm{m}^{-3}$
Hydrogen density n_{H_2}		$\sim 10^{19}\,\mathrm{m}^{-3}$	
Atomic fraction $n_{\mathrm{H}}/n_{\mathrm{H}_2}$		0.2-0.4	
Neutral Cs density n_{Cs}	~ 0		10^{14} - $10^{15}\,\mathrm{m}^{-3}$
Electron temp. T_{e}	$\sim 10\,\mathrm{eV}$		$\sim 1\,\mathrm{eV}$
Hydrogen temp. T_{H_2}		$\sim 0.1\,\mathrm{eV}$	
Ion temp. T_{H^+}, T_{H^-}			0.8 eV

Table 2.5: Typical plasma parameters obtained by measurements in the prototype source. Values for the driver and for the extended boundary layer close to the plasma grid are reported [32, 33].

The extraction and acceleration system consists of three multi-aperture grids: the plasma grid (PG) described before, the extraction grid (EG) and the grounded grid (GG). The extraction voltage U_{ex} between PG and EG is between 5 and 10 kV, while the acceleration voltage $\mathrm{U}_{\mathrm{acc}}$ can be set between 10 and 20 kV: the maximum high voltage available from the power supply, i.e. $\mathrm{U}_{\mathrm{ex}}+\mathrm{U}_{\mathrm{acc}}$ is 22 kV. Negative ions can then be extracted by means of the extraction potential and accelerated to the desired energy, thus generating the negative ion beam. Co-extracted electrons are deflected and dumped onto the EG by means of permanents magnets installed inside the EG.

Cs evaporation is performed by a Cs oven in which a Cs reservoir is heated up and the Cs vapour is injected into the source through a nozzle. The standard oven nozzle configuration at the BATMAN test facility is the one shown in figure 2.9: the nozzle is located on the top of the expansion chamber and the evaporation is directed towards the plasma grid.

The surface temperature is an important parameter that can affect the deposition of Cs and its reactivity with impurities, as it will be explained in chapter 3. In order to have stable performances, the temperature of the source walls and of the plasma grid is actively controlled by a water cooling/heating system. The standard set temperature for the source walls is $\sim 35°$; the PG is instead heated up to higher temperature, i.e. $\sim 150°$. It has been proved experimentally that a higher temperature of the PG surface is beneficial in the achievement of the target value for the extracted current.

The operation of the prototype source at the BATMAN test facility is pulsed, i.e. three different phases can be identified: the vacuum phase, in which the RF

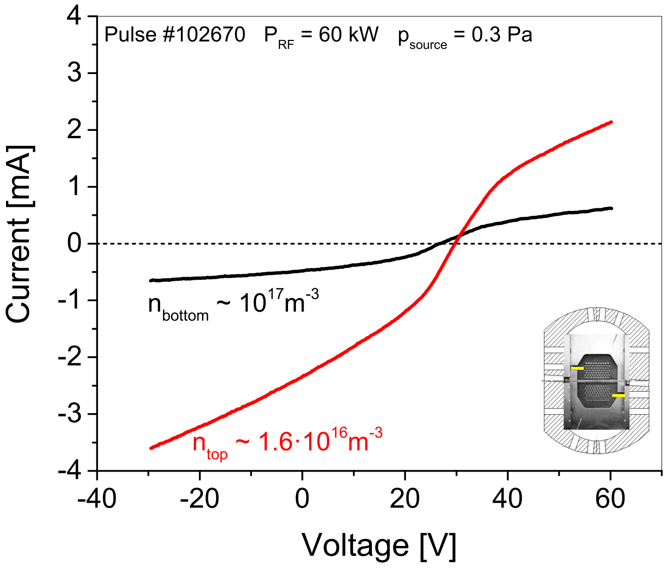

Figure 2.10: Characteristic curve of the two Langmuir probes positioned in the top and the bottom of the prototype source, in front of the plasma grid. The corresponding top and bottom measured plasma density (positive ions) is reported.

power supply is off and no plasma is present in the source; the plasma phase in which the plasma is generated and maintained by the RF; the beam phase, when the high voltage is applied and the negative ions are extracted and accelerated. Cs is constantly evaporated during all these three phases. The maximum plasma phase time achievable at the BATMAN test facility is ∼ 7 s and the beam extraction duration is ∼ 4.5 s. For this pulse length, the ITER requirements for extracted negative ion current density and co-extracted electrons to ions ratio have been simultaneously achieved at the ITER relevant source filling pressure of 0.3 Pa [37].

In order to reach high performances, i.e. high extracted negative ion current density with co-extracted electrons to ion ratio below 1, a so called *conditioning process* is needed: consecutive plasma pulses are performed with a vacuum phase of the order of minutes in between [38]. Several pulses are needed in order to reach a stable value of the extracted negative ion current and of the co-extracted electrons. Due to the complex Cs dynamics, which will be treated in detail in chapter 3, the behaviour of the source is strongly dependent on the caesiation history. In addition, a degradation of the source performances occurs during period of inactivity, such as night or weekends, and a daily reconditioning process is also needed to reach the desired target parameters.

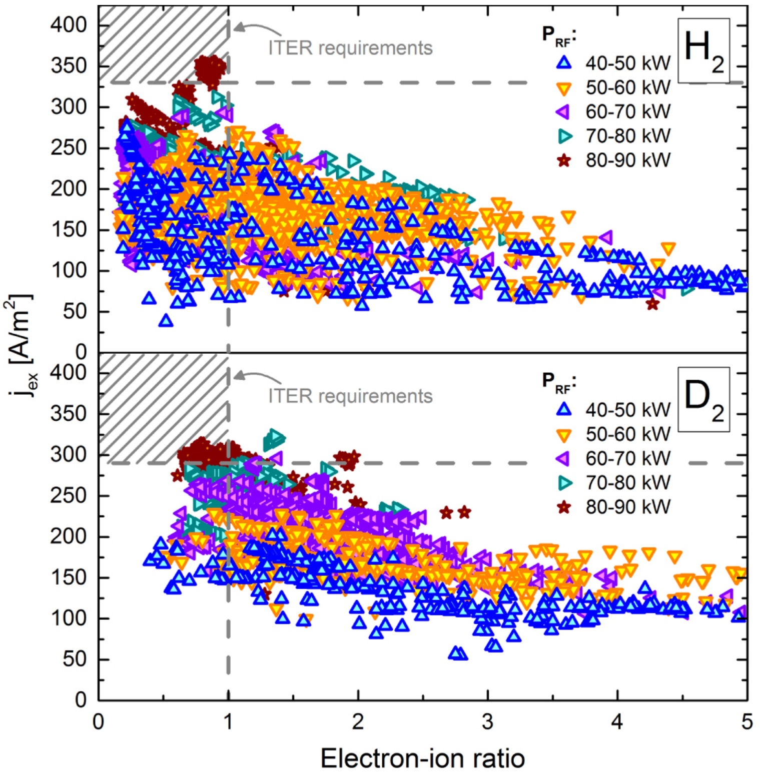

Figure 2.11: The plots shows the extracted negative ion current density versus the co-extracted electron to ion ratio for the two isotopes H_2 and D_2 achieved at BATMAN. The data are color coded according to the RF power [32].

Figure 2.11 shows the performances of the source achieved both in hydrogen and deuterium, i.e. the extracted negative ion current density versus the co-extracted electrons to ions ratio, for a source pressure equal to 0.6 Pa. The data are color coded according to the RF power. The presence of an isotope effect is clearly visible, i.e. different behaviour of the source between operation in hydrogen and deuterium, is clear: similar extracted negative ion current densities can be achieved with both the isotopes, but higher values of the co-extracted electron to ion ratio is observed for deuterium operation [32]. The achievement of the ITER requirements appears therefore much more challenging in deuterium w.r.t. hydrogen: the physical reasons behind the isotope effects are not yet fully understood.

In order to monitor and measure different plasma parameters, several diagnostics are installed close to the plasma grid: this is in fact the region where the most interesting physics in the negative ion sources occurs, i.e. the production, transport and extraction of the negative ions. The schematic of figure 2.12 shows a frontal view of the plasma grid and the ports on the diagnostic flange in which the following diagnostics are installed:

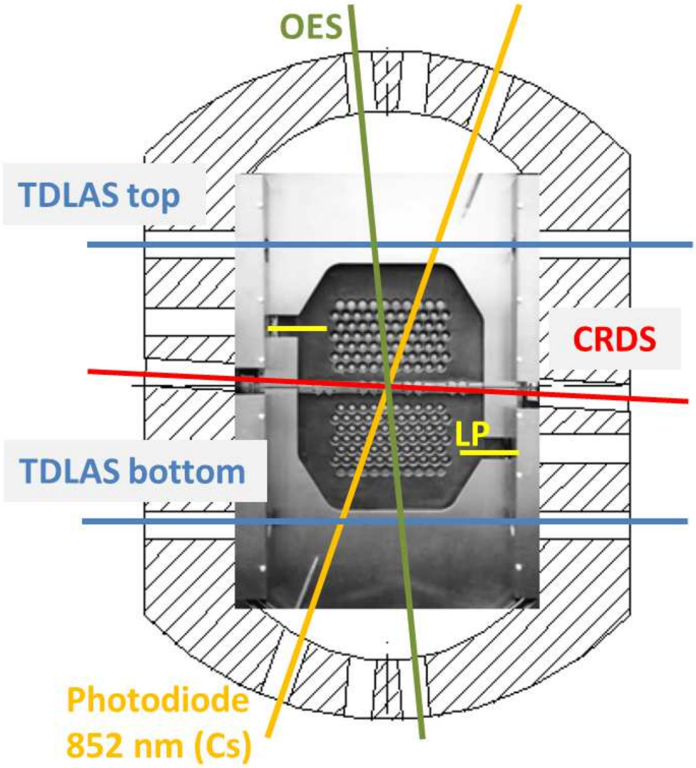

Figure 2.12: Schematic of the diagnostic flange at the BATMAN test facility with the different available diagnostics: Optical Emission Spectroscopy (OES), Tunable Diode Laser Absorption Spectroscopy (TDLAS), Cavity Ring-Down Spectroscopy (CRDS), Langmuir Probes (LP), Photodiode.

- **TDLAS (Tunable Diode Laser Absorption Spectroscopy)**, used to measure the neutral Cs density along two horizontal lines of sight, it will be treated in detail in section 3.4;
- a **photodiode** to detect the radiation in the wavelengths around 852 nm where the emission line of neutral Cs is located (section 3.4);
- **OES (Optical Emission Spectroscopy)**, to monitor the emission of the different species present in the plasma [39];
- **CRDS (Cavity Ring-Down Spectroscopy)**, for the measurements of the negative ion density in front of the grid [40];
- Two **Langmuir probes (LP)**, for the determination of electron temperature, plasma density, floating and plasma potentials.

2.3.2 Half size ITER-NBI source at the ELISE test facility

An intermediate step between the prototype source and the full ITER-NBI source is the ELISE test facility, with half the ITER-NBI source size, i.e. ~0.9 m× 1 m [41].

The basic working principle is the same as for the prototype source. Figure 2.13 shows a schematic view of the source at ELISE. The source has four cylindrical drivers, arranged in two pairs (284 mm diameter and 140 mm length). The maximum RF power achievable is 360 kW (90 kW/driver). The expansion chamber has a volume of $\sim 100 \times 90 \times 25\,\mathrm{cm}^3$.

As in the prototype source, the extraction and acceleration system consists of three grids, the plasma grid, the extraction grid and the grounded grid. The grids have 640 apertures with a diameter of 14 mm, for a total extraction area of $985\,\mathrm{cm}^2$. The apertures are arranged in 8 beamlet-group, 4 in the top and 4 in the bottom, each one consisting of an array of 16×5 apertures. The high voltage power supply can provide 60 kV at maximum.

The scheme of the source in figure 2.13 shows also an horizontal cut of the source in which the positions of the Cs oven nozzles are indicated. The nozzles are positioned on the side of the expansion chamber and the evaporation is directed towards the back-plate. The edges of the nozzle are straight and cut at a 45° angle.

The temperature of the source surfaces is actively controlled: during standard operation the temperature of the PG as well as the bias plate is set to 125°C, while the other source walls are kept at ~ 40°C.

A main difference with respect to the prototype source is the mechanism to generate the magnetic filter field for the cooling of electron temperature. The filter field in larger sources such as the one used at ELISE cannot in fact be generated only by external permanent magnets positioned on the side of the source: due to the size, the magnetic field strength in the centre would not be sufficient. The filter filed is therefore generated by flowing a vertical current through the plasma grid: this generates a more uniform magnetic field along the horizontal direction parallel to the plasma grid

	ELISE
Max. RF power	360 kW (90 kW/driver)
RF frequency	~ 1 MHz
Max. acceleration voltage	60 kV
Plasma phase length	up to 3600 s
Beam phase length	≤ 10 s every 150 s

Table 2.6: Operative parameters at the ELISE test facility.

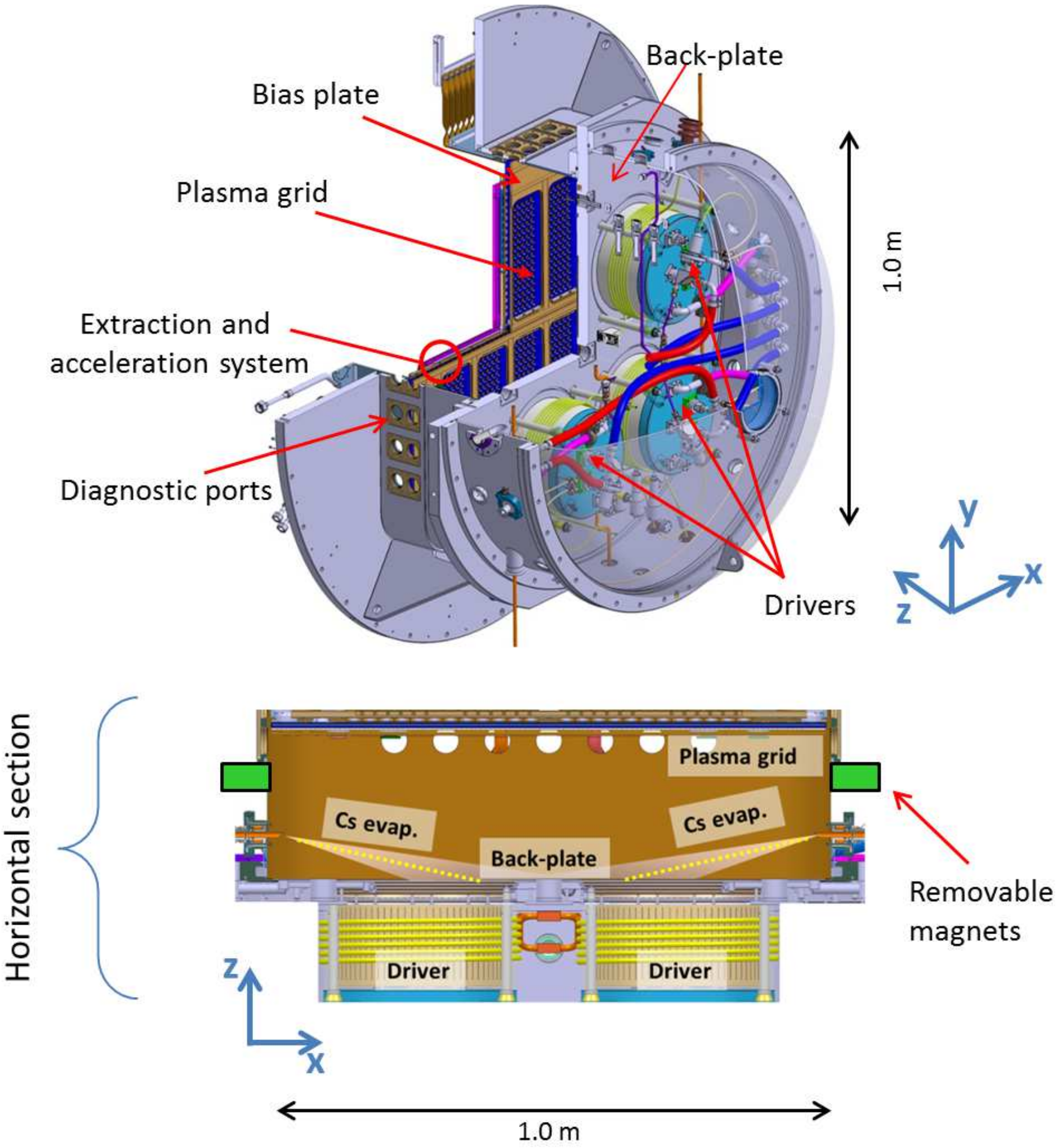

Figure 2.13: Top: scheme of the negative ion source at the ELISE test facility; bottom: horizontal section.

surface. The PG current used for the filter field can be set up to 5.3 kA. Experiments have shown that for ELISE lower filter field is needed (between 2 and 4 mT at the centre of the PG) in comparisons with BATMAN (peak value of 8 mT) [19]. External permanent magnets can be additionally applied in order either to strengthen or weaken the magnetic filter field generated by the PG current and in particular modifing its 3D topology [42]. A more detailed description of the magnetic filter filed in ELISE can be retrieved in the appendix B.

The ELISE test facility is designed to achieve plasma phase up to one hour long.

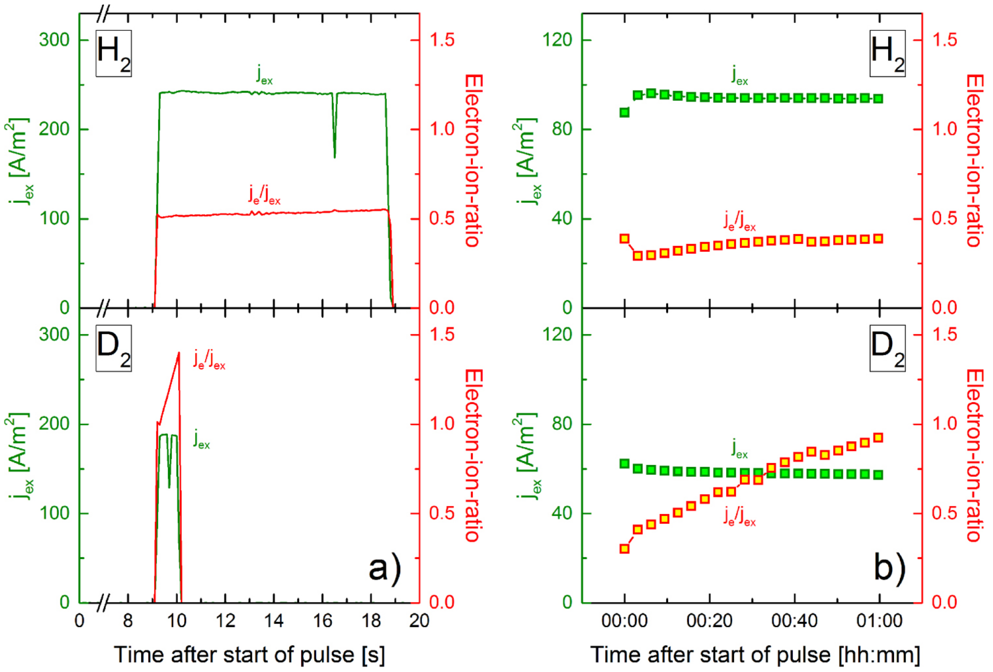

Figure 2.14: Time traces of the extracted negative ion and co-extraceted electron current density for hydrogen and deuterium in the cases: (a) short pulse, power 50 kW/driver and (b) long pulses, 20 kW/driver. Pressure 0.3 Pa. Results are presented for both the isotopes hydrogen and deuterium [32].

There is however a limitation concerning the high voltage power supply, which at present can be operated only for 10 s every 150 s: several beam extraction phases can therefore be performed during a long plasma pulse.

Experiments have shown that for short pulses in hydrogen, high value of current density with low co-extracted electron current density is easily achievable, similarly to the BATMAN case. More problems in controlling the co-extracted electrons arise in case of deuterium operations. The amount of co-extracted electrons is in particular the main limiting factor for the achievement of the ITER requirements during long pulses. Figure 2.14 (a) shows the time traces of the extracted negative ion j_{ex} and of the co-extracted electrons to ion ratio j_e/j_{ex} during a short pulse (20 s) for both hydrogen and deuterium, while figure 2.14 (b) shows the evolution of the current densities during the consecutive beam extraction phases during a long pulse, again both for hydrogen and deuterium [32]. The same isotope effect already found for the prototype source can be observed: the co-extracted electrons are much more unstable in deuterium than in hydrogen. In order to keep the j_e/j_{ex} ratio below 1 for the entire pulse duration in deuterium, the extraction voltage was lower than the hydrogen case, thus limiting the amount the extracted negative ion current j_{ex}.

The best performance achieved so far at ELISE are: 304 A/m^2 (hydrogen) and 250 A/m^2 (deuterium) for short pulses (i.e. 10 s extraction during 20 s plasma phase); 220 A/m^2 (hydrogen) for one hour and 193 A/m^2 (deuterium) for 2700 s [43].

3 Cs dynamics

The temporal and spatial dynamics of Cs in negative ion sources, i.e. the evolution of the transport and of the redistribution of Cs during the plasma operation, have a direct influence on the source performances, i.e. the amount of extracted negative ions and co-extracted electrons. It was experimentally observed that a sufficient Cs flux onto the converter surface is needed to maintain the low work function of the surface [44]. If the work function increases, a decrease of the negative ion generation yield, and therefore of the negative ion density in front of the PG, occurs. Due to the quasi-neutrality principle, a decrease of the negative ion density causes an increase of the electron density and then of the co-extracted electrons. The maintenance of a stable and low value of the work function is necessary for the achievement of the source target, both regarding negative ions and electrons.

Due to the relation between Cs flux and work function of the surface, the presence of spatial disuniformity of the Cs flux onto the PG can lead to a reduction of the negative ion production yield in some specific region of the PG surface. Limiting the spatial asymmetry of Cs distribution on the PG can help in reducing the Cs consumption and therefore the need of maintenance of the source.

This strong interaction between Cs flux, work function and source performances shows how important it is to understand and optimize Cs dynamics, i.e. the redistribution of Cs during the plasma phase and its interaction with the surfaces. The Cs dynamics is extremely complex because it is dominated by the reaction of Cs with the impurities. Cs is in fact a very reactive elements and the presence of impurities in the source is not negligible due to the back-ground gas pressure of $\sim 10^{-4}$ Pa, which is far from the ultra-high vacuum condition. In addition, Cs dynamics is also influenced by the presence of the plasma through processes like sputtering and collisions leading to the redistribution of Cs in the source.

The Cs redistribution in the source is investigated by numerical simulations performed with the Monte Carlo test particle code CsFlow3D. This code was developed in 2009 at IPP Garching and some preliminary insights on Cs distribution in the prototype source were achieved [8]. The final goal is to have a predictive tool which allows for the optimization of the Cs management, i.e. the position and location of the Cs oven nozzle and/or the duty cycle.

Some compromises need to be made for the optimization process, for example the Cs evaporation rate cannot be indefinitely increased during the source operation. It is an experimental evidence that an excessive amount of Cs inside the driver is correlated with a decrease of the H_α emission signal detected in the driver and with a reduction of the extracted negative ion current [32]. In addition, when the leakage of Cs through the PG apertures towards the grid system is too high, a reduction of voltage holding can occur, thus leading to an increased probability of breakdowns [45].

The quantities needed for this optimization and that can be calculated are:

- Cs flux onto the PG, which influences the PG work function and which is related to the source performances, i.e. extracted negative ions and the amount of co-extracted electrons;
- Cs coverage, i.e. the accumulation of Cs reservoirs on the source inner surfaces and that can be desorbed during the plasma phase;
- Neutral Cs density, in order to compare and benchmark the results from the simulations with the measurements obtained by the optical emission spectroscopy and laser absorption spectroscopy (these experimental diagnostics will be described in section 3.4).

In this chapter the basic properties of Cs and the present knowledge of Cs kinetics in the negative ion source environment will be described. Further on a description of the CsFlow3D code together with the improvements and updates that were performed during this work in order to achieve a quantitative benchmark against the experimental data and to ensure enough flexibility for the application of the code also to large sources, such as the one at the ELISE test facility or the full ITER-NBI source.

The Cs evaporation in the source and the experimental diagnostics used to monitor Cs dynamics will be presented as well.

3.1 Transport and kinetics of Cs in negative ion sources

The processes which affect the release, transport and redistribution of Cs in the source, i.e. the Cs dynamics, for the three operational phases (vacuum phase, plasma phase and beam extraction) are shown in figure 3.1.

During the vacuum phase the background pressure is of the order of 10^{-4} Pa. Collisions of the evaporated Cs with the background gas can be neglected at this low pressure and Cs transport can be considered ballistic. In this condition Cs dynamics is basically determined by the Cs oven evaporation profile, the geometry of the source and the surface properties, such as desorption and sticking coefficient. Experimental determination of the sticking coefficient has been performed in similar conditions as those in the ion sources. The surface properties depend both on the temperature of the surface and on the presence of impurities, which can form stable compounds (section 3.1.1) by reacting with Cs.

In the plasma phase the pressure is higher (~ 0.3 Pa) and the collisions of Cs with plasma particles and hydrogen atoms and molecules are relevant and need to be considered 3.1.1. The atomic Cs emitted from the oven or from the surfaces can get ionised due to collisions: its transport is therefore affected also by the electromagnetic field via the Lorenz force. The Cs deposited on the source inner surfaces can be removed and released by the plasma contact with the walls (a detailed explanation of the different removal processes will be given in section 3.1.3).

During the beam extraction phase, an additional source term of Cs needs to be considered. When negative ions are extracted and accelerated, they can collide with the background gas in the extraction system. The result of these collisions is the production of positive ions, namely H^+ and H_2^+, which are accelerated back into the

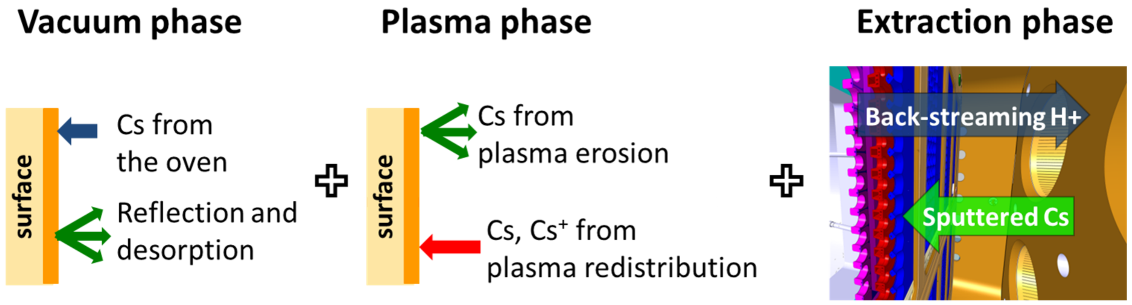

Figure 3.1: Schematic representation of the contributions to Cs dynamics in the different operative phases of the source.

source through the PG apertures with several kV of energy. This is schematically represented on the right of figure 3.1 by the arrow from the PG towards the back-plate of the source. The high energetic back-streaming ions can sputter and release Cs deposited on the back-plate (more details on the back-streaming ion sputtering yield will be given in section 3.1.3).

3.1.1 Properties of Cs and its compounds

In the case of negative ion sources the plasma grid where negative ions are produced is made of molybdenum coated copper: one monolayer of pure Cs onto molybdenum corresponds to a surface atomic density of Cs equal to $4.5 \cdot 10^{14}$ atoms·cm^{-2}, which will be indicated as 1 ML.

The desorption flux of pure Cs from a metal surface with a coverage $\theta < 1\,\mathrm{ML}$ depends on the temperature of the surface and on the coverage:

$$\Gamma_{\mathrm{Cs}} = \Gamma_0 \theta \exp\left(\frac{-e\,(A - B\theta)}{kT}\right) \tag{3.1}$$

where θ is the coverage, T the temperature of the surface, e the elementary charge, k the Boltzmann constant and Γ_0,A and B constants which depends on the material [46]. The fact that the desorption increases linearly with the coverage is due to the repulsive interaction between the Cs atoms within the layer. This repulsive interaction decreases the binding energy of Cs with the surface. Above one monolayer, when bulk Cs is reached, the interaction between Cs atoms is van-der-Waals like and the desorption flux is in principle determined by the vapour pressure:

$$\Gamma_{\mathrm{Cs}} = \frac{1}{4} \frac{p}{\sqrt{2\pi k T m_{\mathrm{Cs}}}} \tag{3.2}$$

For a tungsten substrate the values of the constant of equation 3.1 are available and the desorption flux of Cs for the source wall temperature T ~ 50°C is $\Gamma_{Cs} > 10\,\mathrm{MLs}^{-1}$: a multilayer growth of Cs is therefore only possible if the flux of Cs flux towards the plasma grid is higher than the calculated value. The Cs flux onto the PG can be calculated from the Cs density from an isotrope (thermal) distribution:

$$\Gamma_{\mathrm{Cs}} = \frac{1}{4} n_{\mathrm{Cs}} v_{\mathrm{Cs}} = \frac{1}{4} n_{\mathrm{Cs}} \sqrt{\frac{8kT}{m_{\mathrm{Cs}}\pi}} \tag{3.3}$$

When substituting in equation 3.3 the typical Cs density in negative ion sources, which is between 10^{14} - $10^{15}\mathrm{m}^{-3}$ and the measured Cs temperature in the vacuum phase ~ 350 K [47], the resulting fluxes onto the surfaces are 0.001 - 0.01 MLs^{-1}. The flux is not enough to counteract the desorption and no multilayer growth of pure Cs would develop at this temperatures for low density of Cs vapour.

All these considerations apply to the case of pure Cs on a clean metal surface, but in presence of impurities the formation of Cs compounds can drastically alter this behaviour. The density of the background particles at a source pressure between 10^{-5} and 10^{-4} Pa is in the range between 10^{15} and $10^{16}\mathrm{m}^{-3}$, which is one order of magnitude higher than those of Cs. Beside the hydrogen gas, impurities such as O_2 and H_2O are present, as confirmed by measurements obtained with the mass spectrometer[48]. Since the flux Γ of the particle species i is proportional to $1/\sqrt{m_\mathrm{i}}$, it is evident that the flux of H_2, O_2 and H_2O onto the source inner surfaces is comparable and even higher than the Cs flux, which has a much higher mass. For this reason and due to the high reactivity of Cs, the formation of Cs compounds on the surfaces will drastically change the sticking of Cs onto the surfaces as well as its thermal desorption properties. Unfortunately most of the literature providing data for the interaction properties of Cs with metal surfaces is for ultra-high vacuum conditions, which is not the case for negative ion sources.

The strong impact of the impurities have been confirmed experimentally by Cs density measurements performed during the vacuum phase at the ELISE test facility and without evaporating Cs from the oven, in such a way the desorption from the wall is the only Cs source term active. The source background pressure was 10^{-4} Pa. Figure 3.2 shows the measured Cs density, represented by the squares, as a function of the wall temperatures. As expected, the density increases with increasing temperature. However, when comparing the experimental values with the values of density calculated by the vapour pressure (represented by the full line in the plot), it is evident that the experimental measured density is more than 1000 times lower than the calculated density. Under the ion source conditions, the Cs flux cannot be simply calculated by the vapour pressure, because the reaction with impurities drastically changes the sticking of Cs on the surfaces.

Cs Compound	**Reaction**
CsH (Caesium hydride)	$2Cs+H_2 \longrightarrow 2CsH$
CsO_2 (Caesium superoxide)	$Cs + O_2 \longrightarrow CsO_2$
Cs_2O (Caesium oxide)	$CsO_2+3Cs \longrightarrow 2Cs_2O$
CsOH (Caesium hydroxide)	$2Cs+2H_2O \longrightarrow 2CsOH + H_2$
	$CsH+H_2O \longrightarrow CsOH+H_2$

Table 3.1: Cs compounds present in the environment of a negative ion source and the corresponding reactions.

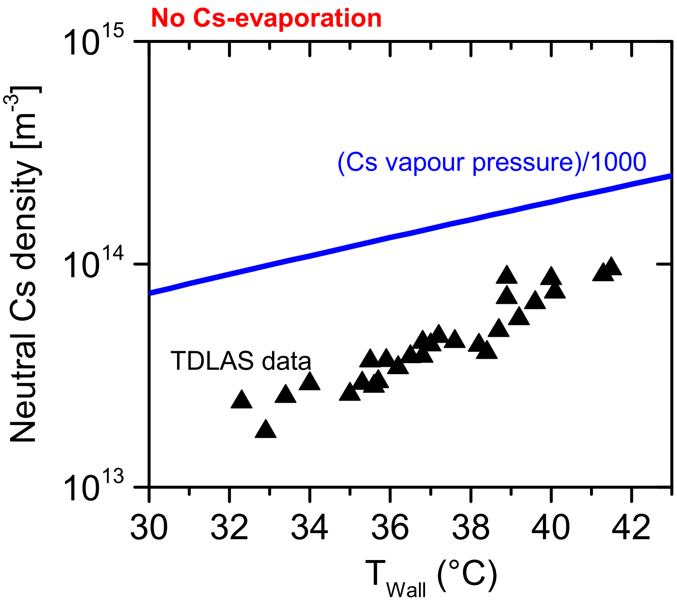

Figure 3.2: Measured neutral Cs density by TDLAS as a function of the wall temperature at the ELISE test facility. The measurements were performed without evaporating Cs and during vacuum phase [47].

The most common Cs compounds that are present in the environment of a negative ion source are reported in table 3.1, together with their relative forming reactions. CsO_2, Cs_2O and CsOH are very stable and spontaenuous dissociation of them at the working temperatures of the negative ion source cannot occur [49]. A different behaviour is instead expected for CsH in a specific range of temperatures and pressure.

Figure 3.3 shows the dissociation pressure as a function of temperature for ceasium hydride. The shaded area below the curve represents the value of temperature and pressure at which the CsH undergoes the dissociation process according to the formula:

$$2\mathrm{CsH} \longrightarrow 2\mathrm{Cs} + \mathrm{H_2} \tag{3.4}$$

During the vacuum phase (10^{-4} Pa) the spontaneous dissociation takes place for $T \gtrsim 60$°C, while during the plasma operation (0.3 Pa) the dissociation occurs at $T \gtrsim 140$°C.

It is an experimental evidence that a heated plasma grid, at least above 120 - 130°C is benefical for negative ion production and source performance. The beneficial effect of heating is probably related to a reduction of the impurities on the PG surface. The optimum temperature of the PG has been found empirically, by comparing the

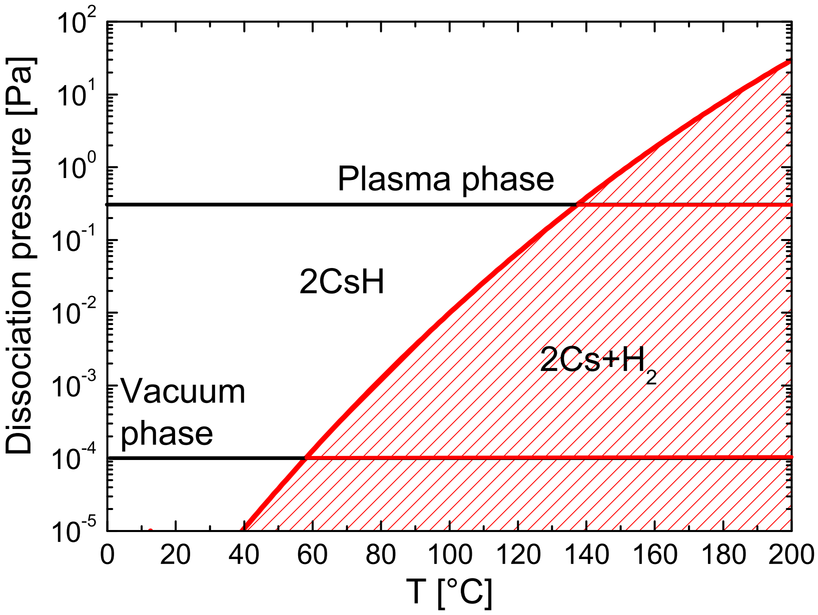

Figure 3.3: Disocciation pressure as function of equilibrium temperature for the Cs-CsH system. The shaded area under the curve is the region in which spontaneous dissociation occurs.

perfomances at different PG temperatures. In the case of the prototype source, the standard temperature for the PG is 150°C, while at the ELISE test facility good performances can be reached already at a temperature of 125°C.

The temperature of the other source walls is kept much lower than the PG temperature, in the range between 30° and 40°: this temperature range will allow the deposition and accumulation of Cs on the surfaces, which can be removed and redistributed during the plasma phase.

3.1.2 Sticking of Cs onto the surfaces

In order to have experimental data for the typical back-ground pressure of the negative ion source ($\sim 10^{-4}$ Pa), dedicated investigations were performed with the ACCesS[1] experiment at the University of Augsburg [50]. The ACCesS experiment consists of an ICP plasma source which can operate at similar parameters as negative ion sources [51, 52].

Figure 3.4 shows a schematic of the dedicated set-up of ACCesS used to evaluate

---

[1] Augsburg Comprehensive Cesium Setup

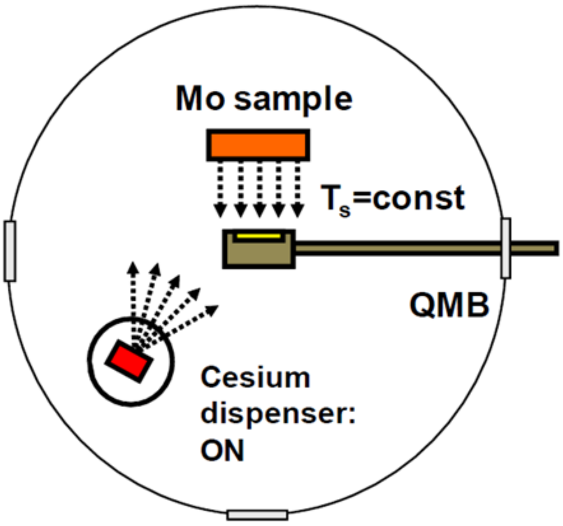

Figure 3.4: Top view of the set-up used for the determination of Cs sticking coefficient onto a Mo sample at the ACCesS experiment by means of a quartz microbalance [50].

the sticking coefficient of Cs onto a Molybdenum target. It consists of a Cs dispenser for the evaporation of Cs, a molybdenum sample towards which Cs is evaporated and a quartz microbalance [53]. The microbalance is a device that can be used to measure the amount of Cs that is deposited on it. It consists of two quartz plates, one exposed to the Cs flux and the other not: the Cs atoms impinging on the exposed surface are deposited on the plate. By using an AC-generator, the resonance frequency of each plate can be determined and the difference between the two resonant frequencies depends on the mass difference between the plates, i.e. the mass of the deposited Cs, according to the formula:

$$\Delta f \propto \frac{\Delta m}{A} \tag{3.5}$$

where Δm is the mass difference between the plates, i.e. the mass of the deposited Cs and A the area of the plates. For the specific case of the microbalance used in the experiments, with an area of $1\,\mathrm{cm}^2$, the frequency different of 4.995 Hz between the exposed plate and the reference plate corresponds to a mass difference of one monolayer of Cs coverage on the exposed plate.

The main idea is to position the Cs dispenser in such a way that there is only direct flux of Cs towards the molybdenum target and not onto the microbalance. The only way Cs can reach the microbalance is when it is reflected by the molybdenum surface. The Cs flux onto the quartz microbalance can be determined from the Cs mass Δm deposited on the microbalance plate during the time interval Δt and the area of the plate, i.e.:

$$\Gamma_{MB} = \frac{\Delta m}{\Delta t A} \tag{3.6}$$

The reflection coefficient $R(T)$ of Cs for different temperature T of the molybdenum sample can be directly measured:

$$R(T) = \frac{\Gamma_{MB}(T)}{\Gamma_{\text{tot}}}, \tag{3.7}$$

where $\Gamma_{MB}(T)$ is the flux impinging the MB, i.e. the reflected flux from the molybdenum at temperature T, while Γ_{tot} is the total Cs flux impinging onto the molybdenum. The sticking coefficient $S(T)$ is the complement to one of the reflection coefficient, i.e.:

$$S(T) = 1 - R(T). \tag{3.8}$$

For the typical temperature of the source walls of ∼40°C a value of sticking coefficient of ∼0.7 was estimated, i.e. ∼ 70% of the Cs impinging is adsorbed, while only 30% is re-emitted. These measurements were based on the assumption that all Cs is reflected at temperature above 88°C, i.e. $\Gamma_{tot} = \Gamma_{MB}(88°C)$.

3.1.3 Cs release and removal from the surfaces

Thermal desorption

The thermal desorption of the Cs deposited on a surface is a process that occurs continuously in the source and is basically dependent on the source temperatures and on the presence of impurities, as for the sticking coefficient. Measurements were performed with the same set-up used for the sticking coefficient. The molybdenum sample was caesiated before the measurments and afterwards the Cs dispenser was switched off. The sample was heated at different temperatures with the quartz microbalance positioned in front of the sample: in this way an estimation of the desorption flux as function of temperature can be obtained [8]. For the range of temperature used for the surface wall of the source, i.e. between 30°C and 40°C, a desorption flux between 0.5 and 1 monolayer/min was measured by the microbalance. The maximum temperature at which the measurements were performed was 80°C and the correspondent desorption flux of 3.5 monolayers/min was measured. All these measurements were performed at back-ground pressure of the source during the vacuum phase, i.e. $\sim 10^{-4}$ Pa, but cannot be performed in the plasma environment, so no data are available for the plasma phase.

Physical sputtering

The threshold energy for physical sputtering is given by the equation:

$$E_{\text{threshold}} = \frac{E_{\text{b}}}{\gamma} \tag{3.9}$$

where E_{b} is the binding energy of Cs (or of the Cs compounds) on the surface and $\gamma = 4m_1m_2/\left(m_1+m_2\right)^2$ is the maximum energy transfer factor between the projectile and the target. When considering the presence of impurities on the surfaces, and therefore the presence of compounds in addition to pure Cs, a binding energy of the order of 1 eV can be assumed. By substituting for the masses of hydrogen and Cs in equation 3.9, the threshold energy results to be of the order of ~ 35 eV. The energy with which the hydrogen ions impinge the Cs covered surface is the diffence between the plasma potential and the wall potential. Measurements in the prototype source have shown that in the driver the plasma potential is ~ 40 V, while it reduces to half this value in the expansion chamber (see the appendix A). Therefore physical sputtering of Cs due to the positive hydrogen ions inside the ion source can occur only in the driver, while it is negligible on the other surfaces of the source.

In contrary, the high energetic (several kV) back-streaming ions H^+ and H_2^+ created inside the grid system can be accelerated back inside the source and efficiently sputter Cs from the back-plate. In figure 3.5 the projections of the PG aperture onto the back-plate are shown for the prototype source at the BATMAN test facility and for the ELISE test facility. It can be noticed that in the case of BATMAN, all the projections are inside the driver back-plate, while in the ELISE part of the projection of the grid apertures are on the back-plate.

There are two direct reactions that can generate H^+ and H_2^+ ions inside the acceleration system:

$$H^- + H_2 \longrightarrow H^+\,(\text{fast}) + 2e^- + H_2 \tag{3.10}$$

$$H^- + H_2 \longrightarrow H_2^+\,(\text{at rest}) + 2e^- + H^0 \tag{3.11}$$

Another possibility is a two-step process starting first with a formation of a high energetic neutral:

$$H^- + H_2 \longrightarrow H^0\,(\text{fast}) + e^- + H_2 \tag{3.12}$$

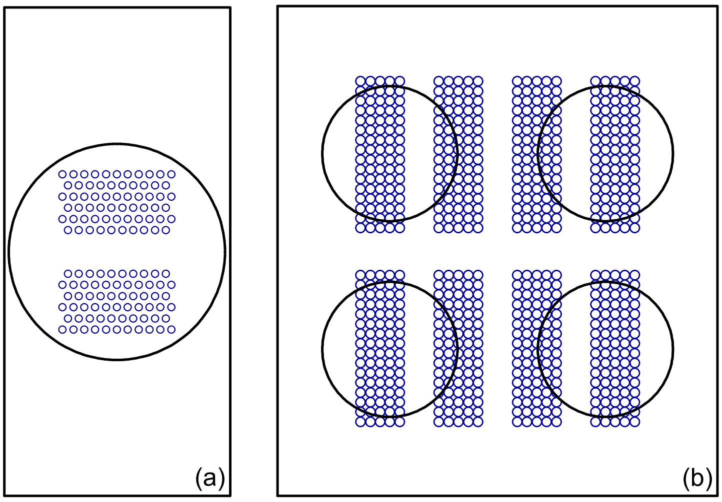

Figure 3.5: Footprint of the apertures of the PG onto the back-plate for the prototype source at BATMAN (a) and for the source at ELISE (b). The black circular contours indicate the drivers.

and the consequent formation H^+ or H_2^+:

$$H^0 + H_2 \longrightarrow H_2^+\,(\mathrm{fast}) + e^- + H^0 \tag{3.13}$$

$$H^0 + H_2 \longrightarrow H^+\,(\mathrm{at\,rest}) + e^- + H_2 \tag{3.14}$$

The extraction stage, i.e. the first gap of the high voltage grid system, is the one where the formation of the back-streaming ions is more relevant due to the higher H_2 gas pressure: on the source side of the grid system the pressure is $\sim$0.3 Pa, while on the other side it is of the order of $\sim 10^{-4}$ Pa.

The flux of these back-streaming ions was determined experimentally by investigating the sputtering of copper samples in the prototype source at the MANITU test facility. The set voltages are 5 keV between the PG and the EG and 15 keV between the EG and the GG. The total resulted flux of back-streaming ions was $2.45 \cdot 10^{15}\,\mathrm{cm^{-2}s^{-1}}$ for an extracted negative ion current of $16.1\,\mathrm{mA\,cm^{-2}}$. Calculations have shown that ion energy distribution functions for H^+ has a peak at 15 keV, while for H_2^+ has two peaks at 7.5 and 20 keV [54]. Simulations based on the TRIM.SP code [55] have been performed in order to calculate the sputtering yield due to back-streaming ions on a thick Cs layer: the dependence on the energy for H^+ is plotted in figure 3.6. The sputtering yield $Y_{H_2^+}$ for H_2^+ can be then calculated from

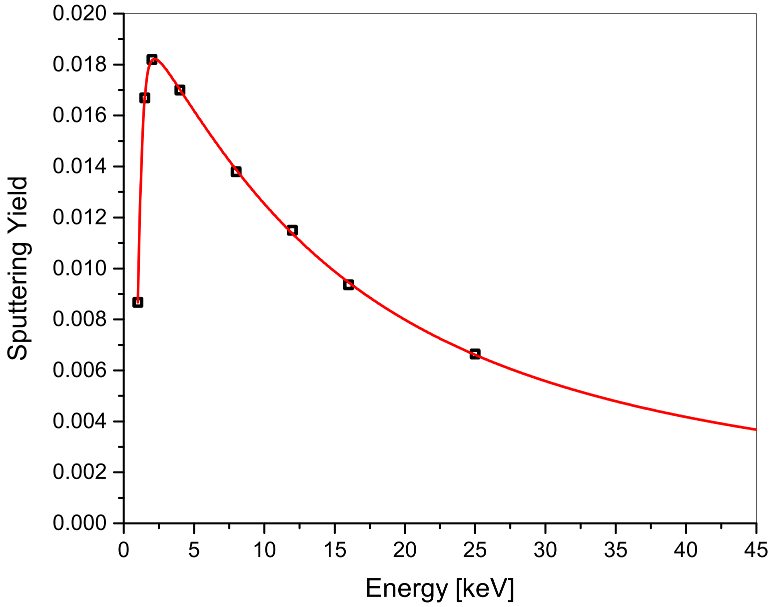

Figure 3.6: Sputtering yield of Cs by H^+ as a function of the ion energy. A thick Cs layer target is assumed.

the sputtering yield Y_{H^+} of H^+ by the relation:

$$Y_{H_2^+}(E) = 2 \cdot Y_{H^+}(E/2) \tag{3.15}$$

Further desorption processes

Both at the BATMAN and ELISE test facilities, large areas of Cs erosion can be observed on the lateral surfaces of the expansion regions, close to the driver exit, where the plasma is more intense. The threshold energy for physical sputtering by means of the positive hydrogen ions of the plasma is too low in these regions and cannot be the explanation for the observed erosion areas.

Another possible mechanism of Cs release from the walls can be the chemical sputtering of Cs due to reactive plasma particles, such as the positive hydrogen ions or the hydrogen atoms. The chemical sputtering is a process where the ion bombardment causes a reaction with the particles in the sources, thus producing molecules which are weakly bound to the surface. These molecules can be easily desorbed from the surface into the source volume. An example where chemical sputtering is known to occur is the case of hydrogen and deuterium bombardment of carbon [56] as well as the chemical erosion of hydrocarbon (C:H) films in hydrogen plasma [57]: in these cases the observed erosion yield at low energy are much higher than the calculated physical sputtering yield via TRIM.SP simulations.

However, data for chemical erosion processes of Cs due to reactive ions sputtering in the ion sources conditions are not available: up to now this phenomena can only be taken into account empirically by considering an additional sputtering yield term Y_{chem} to fit with the observed erosion pattern on the source chamber and the observed Cs density.

3.1.4 Cs collisions

Vacuum phase

The back-ground density during the vacuum phase is $\sim 10^{16}\,\mathrm{m}^{-3}$ (pressure of 10^{-4} Pa, $T = 300\,\mathrm{K}$). For this value of density the mean free path for the collision process between Cs and the back-ground gas is several times larger than the typical size of the source. As a matter of fact, the cross section of the elastic collision of Cs with H_2 can be expressed as [58]:

$$\sigma\left(v_{\mathrm{r}}\right) = \frac{C}{v_{\mathrm{r}}^{2/5}} \tag{3.16}$$

where C is a specific constant for the process and v_{r} is the relative velocity between the two collision partners. By using the value of the constant C tabulated in [58], the resulting cross section is of the order of $10^{-18}\,\mathrm{m}^{-2}$. Hence, the mean free path is:

$$\Lambda \sim \left(\sigma n_{\mathrm{H}_2}\right)^{-1} \sim 10^{2}\,\mathrm{m} \tag{3.17}$$

Collisions are therefore not relevant for the Cs transport during the vacuum phase of the source.

Plasma phase

Collisions of Cs with the back-ground H_2 gas and with the plasma particles become relevant in the plasma phase due to the higher pressure (~0.3 Pa).

One important process that takes place during plasma operation is the ionisation of Cs by means of electron impact collisions: the first ionisation energy of Cs is 3.89 eV [30], the lowest of all elements. Collisions between Cs^{+} and an electron can result in radiative recombination. Figure 3.7 shows the rate coefficients for the electron impact ionisation and radiative recombination as a function of the electron temperature. Since the electron temperature in the source varies between 10 eV in the driver and 1 eV close to the plasma grid, a high ionisation degree of Cs during plasma is expected. The radiative recombination due to collisions with electrons is in fact more than three orders of magnitude lower for the specified energy range. The only

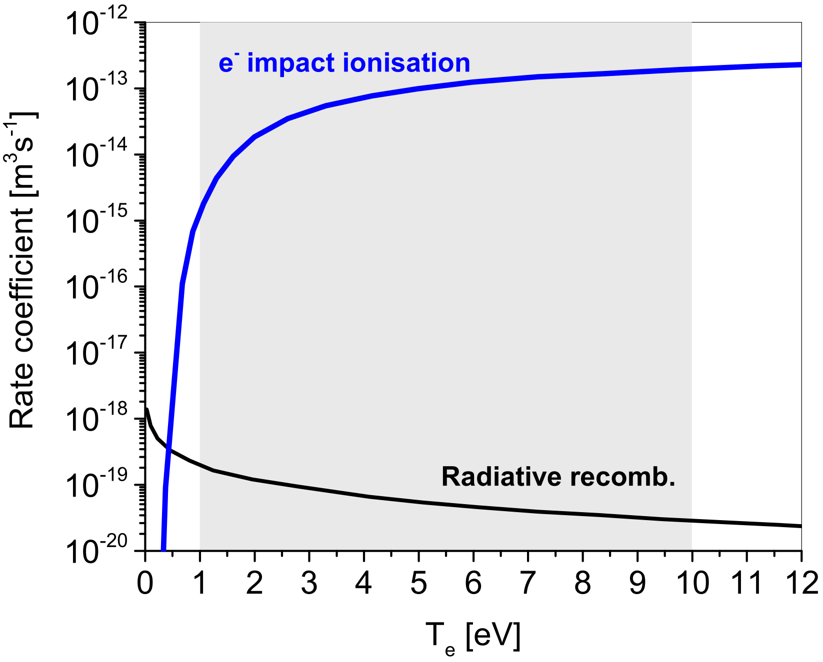

Figure 3.7: Rate coefficient of electron impact ionisation and radiative recombination for Cs in the range of electron temperatures typical of the negative ion sources.

effective neutralisation process is the recombination of a Cs ion with an electron from the surface of the source walls: the Cs ions that hit the wall are converted into neutral and can be either adsorbed or re-emitted, depending on the sticking parameter. The second ionisation of Cs, i.e. the formation of Cs^{2+} has a much higher threshold energy, which is 23.16 eV [30]. The production probability of Cs^{2+} is therefore very low in the RF negative ion source environment, where $T_e < 10\,\mathrm{eV}$.

The relevant collisions are shown in table 3.2, where the type of reaction and/or the cross section dependence is presented.

$Cs + e^-$	$\longrightarrow$	$Cs^+ + 2e^-$	Electron-impact ionisation
$Cs^+ + e^-$	$\longrightarrow$	$Cs + h\nu$	Radiative recombination
$Cs^+ + e^-$ (wall)	$\longrightarrow$	Cs	Wall recombination
$Cs + H_2$	$\longrightarrow$	H_2 Cs	Van-der-Waals $\sigma(v) \propto v^{-2/5}$
$Cs^+ + H_2$	$\longrightarrow$	$H_2 + Cs^+$	Langevin $\sigma(v) \propto v^{-1}$
$Cs + H$	$\longrightarrow$	$H + Cs$	$\sigma = \pi (r_H + r_{Cs})^2$
$Cs^+ + H$	$\longrightarrow$	$H + Cs^+$	$\sigma = \pi (r_H + r_{Cs})^2$
$Cs^+ + H_x^+$	$\longrightarrow$	$H_x^+ + Cs^+$	Coulomb

Table 3.2: Relevant collision processes of Cs during the plasma phase [8, 9].

3.2 CsFlow3D code

The numerical model CsFlow3D was developed in 2009 at IPP [8] with the purpose of investigating the Cs transport and redistribution inside the entire volume of the source. The best way to achieve this purpose is to use a Monte Carlo Test Particle model: it would be in fact computationally impossible to use particle-in-cell methods to model the full geometry of the source with the required resolution to solve the collision processes.

Calculation of the transport probabilities of Cs test particles

The inner surfaces of the source are divided into surface elements and the Cs transport probabilities between surface elements can be calculated via Monte Carlo methods (see the scheme in figure 3.8). The typical size of the surface elements is $\sim 1\,\mathrm{cm}^2$. In particular two types of transport probability need to be calculated:

- the vector $\mathbf{O}\,(i)$, which represents the transport probability from the Cs oven nozzle (or nozzles) onto the surface element i;
- the matrix $\mathbf{G}\,(i,j)$, which represents the transport probability from the surface element i to the surface element j.

For the calculation of $\mathbf{G}\,(i,j)$, a certain number of test particles (normally $\geq 10^5$) are emitted from the surface element i with a cosine distribution and transported

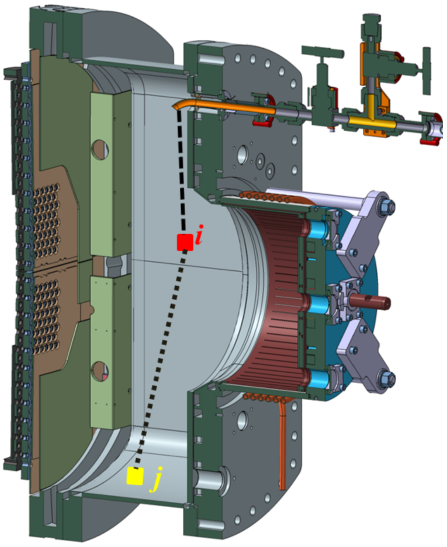

Figure 3.8: Schematic view of the prototype source with two example surface elements i and j used by CsFlow3D to calculate the transport probabilities.

inside the source until they hit another surface element j. The transport inside the source volume is modelled as ballistic for the vacuum phase, i.e. with a starting velocity which is sampled by a Maxwellian distribution with the temperature of the walls. During the plasma phase, the collisions are taken into account.

Since ionisation can take place during plasma, the transport modelling needs to consider the Lorenz force due to the electro-magnetic field. Therefore, after the collisional process, the velocity is update at each time step Δt following the relation:

$$\mathbf{v}\left(t+\Delta t\right)=\mathbf{v}\left(t\right)+\frac{e}{m_{\mathrm{Cs}}}\left(\mathbf{E}+\mathbf{v}\left(t\right)\times\mathbf{B}\right)\cdot\Delta t \tag{3.18}$$

The procedure is repeated until the particles hit one of the inner surfaces of the source. For the evaporation from the oven the suitable evaporation pattern (which is a squared cosine distribution). In the case of the oven matrix $\mathbf{O}\left(i\right)$ the test particles are emitted accordingly to the oven nozzle outflow profile considered in section 3.3.

The value of the used time step need to be chosen in order to correctly solve the collisions, i.e. $\Delta t\omega << 1$, where ω is the collision frequency. The value of Δt used in the simulations is 10^{-6} s.

Two groups of collisions are taken into account: short range elastic collisions and long range Coulomb collisions. For short range collisions, the probability that a collisions occurs during a time step is given by the path-length estimator [59]:

$$P=1-\mathrm{e}^{-\omega\Delta t} \tag{3.19}$$

where Δt the time step and ω the collision frequency for the specific collision defined as:

$$\omega=n\int_{0}^{\infty}\sigma\left(v_{\mathrm{rel}}\right)v_{\mathrm{rel}}f_{\mathrm{T}}\left(v_{\mathrm{rel}}\right)dv_{\mathrm{rel}} \tag{3.20}$$

where n is the density of the field particles with which the Cs atom/ion collides, $\mathbf{v}_{\mathrm{rel}}$ the relative velocity, $\sigma\left(v_{\mathrm{rel}}\right)$ the cross section and f_{T} the Maxwellian distribution function of the field particles at temperature T.

In order to decide if a collision takes place a random number RND is generated: if RND$<P$, the collision occurs. The relative velocity between the Cs particle and the field particle (i.e. the collision partner) is defined as:

$$\mathbf{v}_{\mathrm{rel}}=\mathbf{v}_{\mathrm{Cs}}-\mathbf{v}_{\mathrm{field}} \tag{3.21}$$

The effect of a short range elastic collision is a rotation $\boldsymbol{\Delta}\mathbf{v}_{rel}$ of the relative velocity vector between the Cs particle and the field particle (i.e. the collision partner): the

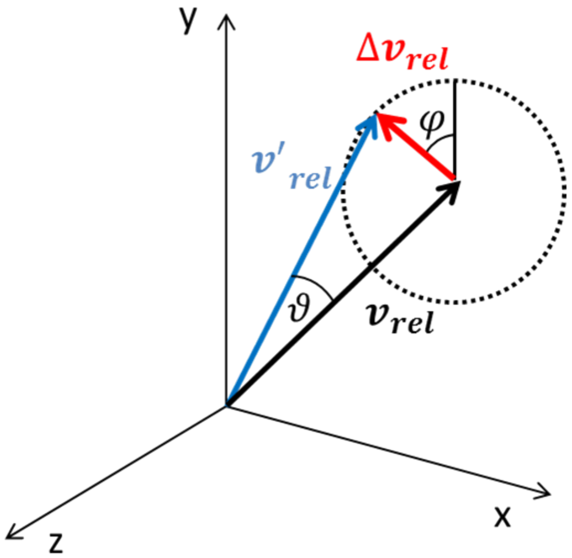

Figure 3.9: Schematic representation of the scattering angle θ and ϕ of a collision and the consequent rotation of the relative velocity vector.

scattering angle θ and ϕ, shown in figure 3.9, are generated by a uniform distribution. The new velocity vector for the Cs is therefore:

$$\mathbf{v}'_{\mathrm{Cs}} = \mathbf{v}_{\mathrm{Cs}} + \frac{m_{\mathrm{field}}}{m_{\mathrm{field}} + m_{\mathrm{Cs}}} \boldsymbol{\Delta}\mathbf{v}_{\mathrm{rel}} \tag{3.22}$$

For the case of the long range Coulomb interactions, the cumulative deviation due to frequent small angle collisions is calculated by assuming a Gaussian distribution of the θ angle and a uniform distribution of the ϕ angle. These scattering angles can be obtained by two random numbers RND1, RND2 generated with a uniform probability between 0 and 1 [60]:

$$\theta = \sqrt{[-2\omega\Delta t \ln{(1 - \mathrm{RND1})}]}, \tag{3.23}$$

$$\phi = 2\pi\mathrm{RND2} \tag{3.24}$$

where again ω is the collision frequency and Δt is the time step.

The knowledge of density and temperature of all the collisional partner species is fundamental for the treatment of the collisions, i.e. for the determination of the collision frequency by following equation 3.20. Figure 3.10 shows the plasma parameter profiles used by CsFlow3D for plasma density and electron temperatures along the source axis of the prototype source. A detailed description of the 3D map of plasma parameters used by the code for the prototype source and for ELISE is given

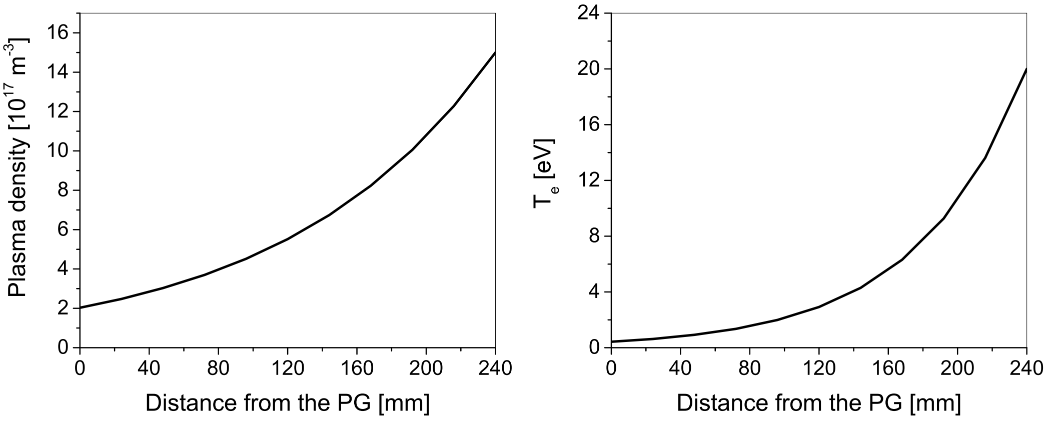

Figure 3.10: Plasma density and electron temperature along the axis for the prototype source used in CsFlow3D.

in appendix A.

Simulation of Cs dynamics with the calculated transport probabilities

The calculation presented so far allows the determination of the transport probability between surface elements in the source, by taking into account the collisions and the Lorenz force in the case of the ions. The Cs redistribution in the source can therefore be simulated by using the calculated transport probabilities and by taking into account all the Cs source terms such as desorption, sputtering and the evaporation from the Cs oven.

The source operation is divided in time steps, usually smaller than 0.5 s. This higher limit was determined by performing several simulations and comparing the results: no relevant difference were observed for time step below 0.5 s. At each time step, N caesium particles are injected accordingly to the oven evaporation rate. The Cs deposited on the surface element i due to the Cs evaporation is given by:

$$\mathbf{DEP}\,(i) = \mathbf{S}\,(i) \cdot N \cdot \mathbf{O}\,(i) \tag{3.25}$$

where $\mathbf{S}\,(i)$ is the sticking coefficient. The number of emitted particles $\mathbf{EMIT}\,(i)$ from the surface element i can be calculated as the sum of those reflected from the source element i plus the one desorbed ($\mathbf{DES}\,(i)$) via the different desorption and removal processes explained before:

$$\mathbf{EMIT}\,(i) = [1 - \mathbf{S}\,(i)] \cdot N \cdot \mathbf{O}\,(i) + \mathbf{DES}\,(i) \tag{3.26}$$

After this, the redistribution takes place in many iterative steps until all the Cs is deposited somewhere. At each iterative step the values of **DEP** and **EMIT** vectors are updated:

$$\mathbf{DEP}_{\text{new}}(i) = \mathbf{DEP}_{\text{old}}(i) + \mathbf{S}(i) \cdot \sum_j \mathbf{G}(i,j) \cdot \mathbf{EMIT}_{\text{old}}(j) \tag{3.27}$$

$$\mathbf{EMIT}_{\text{new}}(i) = [1 - \mathbf{S}(i)] \cdot \sum_j \mathbf{G}(i) \cdot \mathbf{EMIT}_{\text{old}}(j) \tag{3.28}$$

The convergence criteria is given by the condition:

$$\sum_i \mathbf{EMIT}_{\text{new}}(i) < N_{\text{residual}} \tag{3.29}$$

where N_{residual} is the minimum number of residual free Cs particles at which the iteration process can be considered converged. Once a single time step has converged, the vector **DEP** contains the coverage of Cs for each surface element. The fluxes onto a surface element can be calculated summing up all the particles that impinged onto the surface elements during the time step. The simulation can therefore proceed with the following time step.

This procedure is carried on separately for the Cs ions and the neutral Cs, so that at the end it is possible to discriminate the neutral and the ion components of the Cs flux on the surfaces.

3.2.1 State of the art

The CsFlow3D code was developed as topic of a previous PhD thesis [8] and it was applied to the prototype source. The knowledge acquired by these preliminary investigations are summarised in the following:

- **The Cs flux onto the PG** resulted of the order of $10^{12}\,\text{cm}^{-2}\,\text{s}^{-1}$ during the vacuum phase and one order of magnitude higher for the plasma phase. The release process of Cs from the source inner surface was proved to be the dominant source term of Cs during plasma. Due to the local variation of the plasma parameters, also the ionisation degree of Cs varies locally: most of the Cs flux onto the PG is ionised, up to fraction of 80 - 90%. The ionisation degree is higher in the regions where electron temperature is higher, i.e. close to the driver.

- **The Cs deposited on the inner surfaces** influences the time behaviour of the flux onto the PG. The code showed a depletion of the Cs reservoirs on the source walls due to plasma assisted erosion during the pulse, which correlates with a decrease of the Cs flux onto the PG, especially in the case of a long pulse (hundreds of seconds).
- **Slight inhomogeneity of the Cs flux onto the PG** was shown by the code results in correlation with the position of the Cs oven.
- **An alternative oven configurations**, i.e. relying on the direct evaporation of Cs close to the PG was simulated: the code revealed that in this case the Cs flux is mostly determined by the Cs evaporation rate and not by the plasma assisted redistribution, as in the standard case (Cs oven in the back-plate).

The major limitations of these analysis was that only one cycle of vacuum phase and plasma phase was simulated, but the conditioning process, i.e. the repetition of many cycles with the consequent replenishment and redistribution of the Cs reservoirs on the source walls, was not simulated. This process might drastically change the Cs dynamics and the fluxes of Cs onto the PG, due to enriched Cs reservoirs or different accumulation patterns. In addition, no quantitative benchmark against experimental data was possible: in the experiments the information about Cs evolution and distributions can be obtained by the measurements of neutral Cs density can be measured, a quantity which was not accessible at that time.

3.2.2 Updated version of the code

The current work has the aim at first to benchmark the code results against the data of the prototype source at BATMAN. In order to achieve this target the code needs to be updated with the possibility of calculating the neutral Cs density, so that simulation results can be quantitatively and directly compared with experiments. Further on, the size scaling should be investigated, by extending the simulation domain to that of ELISE and to attempt some preliminary investigations also of the full size NBI source for ITER (e.g. SPIDER).

A diagram of the input needed by the code and output quantities of the updated version of CsFlow3D is given in figure 3.11.

Calculation of neutral Cs density

The standard output quantities given by the CsFlow3D code, i.e. the Cs fluxes and

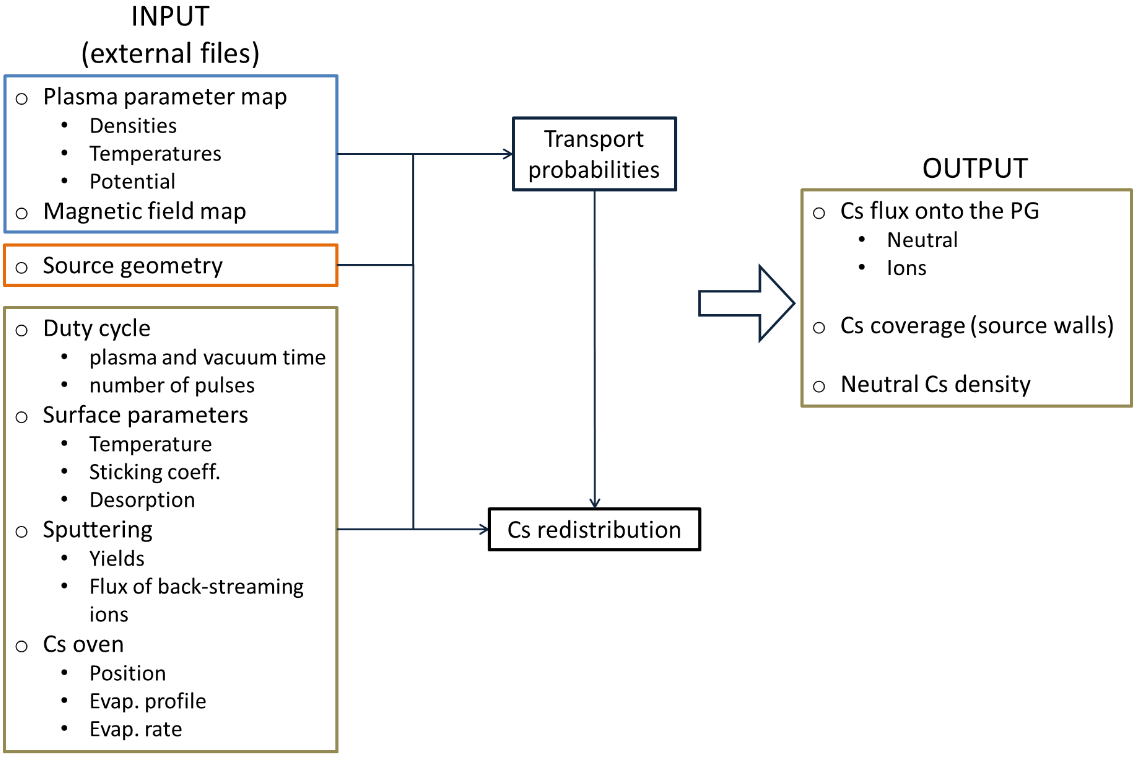

Figure 3.11: Diagram describing the input, the calculation and the output of the CsFlow3D code.

the coverage on the wall surfaces cannot be measured at the test facilities: a quantitative benchmark of the code is not possible by using these output values. The only quantitative diagnostic to experimentally monitor Cs dynamics is TDLAS, described in section 3.4, which measures the neutral Cs density. The Cs density inside the volume of the source cannot be directly calculated by CsFlow3D due to the fact that it is a test particle model which only uses transport probability matrixes among surface elements.

The way to retrieve the value of the line of sight averaged neutral Cs density is to implement virtual surfaces that correspond to the lines of sight used by TDLAS. These surfaces can be approximated by cylinders, which are completely transparent for Cs, meaning that Cs cannot be deposited neither emitted from them. One artificial cylindrical surface S is schematically represented in figure 3.12. The trajectory of N test particles emitted for each surface element i (as well as the Cs oven nozzle) is computed. The fraction of particles which start from an element i and cross the surface S is:

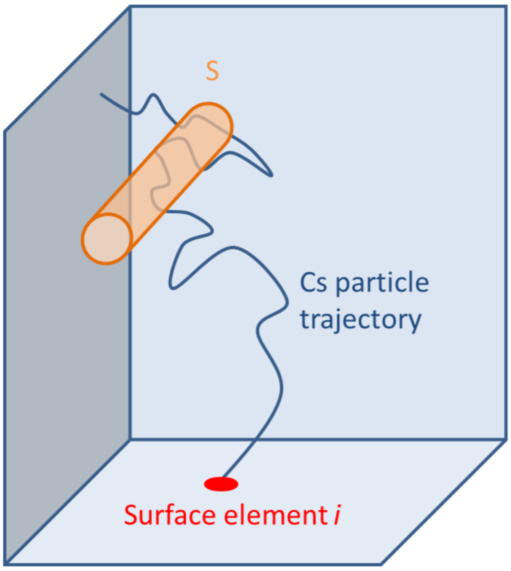

Figure 3.12: Schematic representation of the method used to calculate Cs density inside the line of sight volume in CsFlow3D. The cylindrical virtual surface S is shown together with the trajectory of a Cs particle emitted by the surface element i on the source wall and crossing the surface.

$$f_\mathrm{i} = \frac{N_\mathrm{i,S}}{N}. \tag{3.30}$$

One general Cs particle j is emitted from the element i and crossing the surface S. If the residence time inside the volume enclosed by S of the particle j is defined as $\Delta t_{i,j}$, it follows that the mean residence time of all the particles emitted by the surface element i is given by:

$$\langle dt_\mathrm{i} \rangle = \frac{\sum_\mathrm{i}^{N_\mathrm{i,S}} \Delta t_{i,j}}{N_\mathrm{i,S}} \tag{3.31}$$

As described previously, during a time step Δt, the Cs emitted by each surface element i is given by $\mathbf{EMIT}_\mathrm{i}$. It follows that the total number of particles that crosses the surface S during the time step are:

$$\sum_i f_\mathrm{i} \cdot \mathbf{EMIT}_\mathrm{i}. \tag{3.32}$$

Each particle has a different residence time and in order to estimate an instantaneous number of particles inside the volume, the sum of 3.32 should be weighted on the average residence time calculated with equation 3.31:

$$\sum_i f_\mathrm{i} \cdot \mathbf{EMIT}_\mathrm{i} \cdot \frac{dt_\mathrm{i}}{\Delta t} \tag{3.33}$$

If V is the measure of the volume enclosed by the surface S, an estimator of the Cs density, averaged inside the volume during the time step, is given by dividing the sum in 3.33 by V:

$$n_{Cs} = \frac{1}{V} \sum_{i} f_{\mathrm{i}} \cdot \mathbf{EMIT}_{\mathrm{i}} \cdot \frac{dt_{\mathrm{i}}}{\Delta t} \tag{3.34}$$

By accurately defining the surface S with the same geometry of the TDLAS lines of sight in the experiments, the output quantity calculated by the code is directly and quantitatively comparable with the experimental measurements. This is therefore a very important tool for the benchmark of the code.

Extension to the geometry of the ELISE source and full ITER-NBI source
The definition of the source geometry has been made more versatile, in order to allow for simulations of Cs dynamics also for larger sources with more drivers, such as the source at the ELISE test facility, with two pairs of drivers or the full source for the ITER-NBI (with four pairs of drivers). Simulations can be performed for ELISE and the behaviour of Cs dynamics compared with that in the prototype source.

Real geometry of the PG aperture
In order to have the possibility of simulating the conical shapes of the PG apertures, the code was updated with the real geometry of the apertures. This is of particular importance when considering the re-emission of Cs from the surface with a cosine distribution, which is peaked to the surface normal: a different shape of the surface affects the Cs redistribution.

Increase of the versatility of the input parameters
In order to have the option to simulate Cs dynamics in any negative ion sources, the possibility of inserting all the input parameters as external input files was also added. This is valid not only for the plasma parameters and the magnetic field, but also for the temperatures, the sticking coefficient and the oven nozzle position, orientation and evaporation profile. A diagram describing the input and output of the code is shown in fig. 3.11.

3.3 Cs evaporation in negative ion sources

Caesium is injected inside the source by evaporation from a heated liquid Cs reservoir. Figure 3.13 shows a cut view of the Cs oven used to evaporate Cs, which consists of three main parts: a sealed glass ampoule containing 1 g of Cs, the oven body and the nozzle. When the glass ampoule is cracked, the Cs flows into the oven body and it is collected in the so called reservoir. Heating elements are present on the reservoirs, the conduction pipe and the nozzle as well: the temperature of the different elements is feedback controlled.

By changing the temperature of the Cs reservoir it is possible to change the Cs vapour pressure and therefore the evaporation rate of Cs through the nozzle. The range of temperature of the liquid reservoirs during the operation is between 90°C and 140°C. All the other parts of the oven need to be maintained at much higher temperature w.r.t. the reservoir, namely $T > 250°\mathrm{C}$, in order to avoid the formation of cold-spots where Cs can condense, thus affecting the oven operation. Thermocouples are located on the nozzle, the conduction pipe and on the Cs reservoir in order to have a real time monitoring of the temperatures of the different oven parts.

Two valves are placed in the pipe which connect the reservoir with the nozzle: this is needed on the one hand to stop Cs evaporation and on the other hand to have the

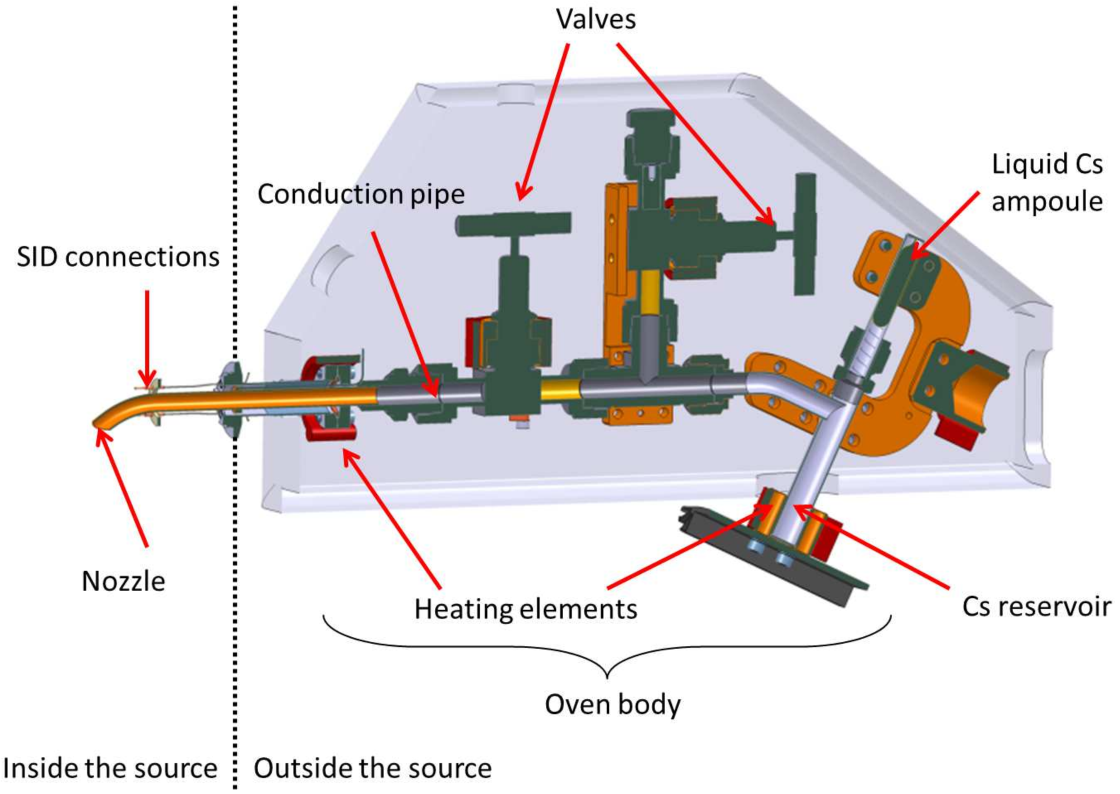

Figure 3.13: Drawing of the liquid Cs oven used in the negative ion sources at the IPP test facilities.

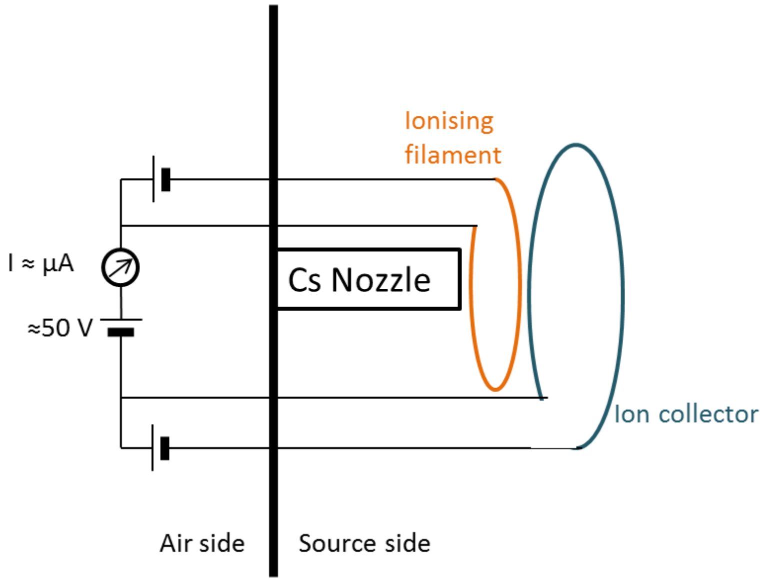

Figure 3.14: Electric scheme of the Surface Ionisation Detector (SID) used to determine the evaporation rate of the Cs oven.

possibility of changing the Cs ampoule without breaking the vacuum in the source.

In order to have a real time relative measurement of the evaporation rate during the experiments, a surface ionisation detector (SID) is mounted in front of the Cs oven nozzle. The SID consists of two heated tungsten filaments which are biased with a potential difference between each other of around 50 V, as shown in figure 3.14. The Cs atoms exiting from the nozzle get ionised when getting in contact with the first tungsten filament due to surface ionisation. This process can takes place only if the ionisation energy of the atom is lower than the surface work function: this is true for Cs (and in general for alkali metals) w.r.t. the tungsten work function (4.55 eV) [29]. The Cs^+ ions are then accelerated by the electric field towards the other tungsten wire which acts as ion collector: a current flowing between the filaments can be detected. The current is proportional to the number of Cs atoms impinging the first filament, i.e. to the evaporation rate of Cs. In order for this system to work and in particular to ensure a linearity between the current measured and the evaporation rate, the deposition of Cs on the filaments, which could alter their work function, needs to be avoided. Each tungsten filament is therefore Ohmically heated up to $\sim 1400°C$, a temperature at which the residence time of Cs on tungsten is sufficiently low, thus avoiding any work function change [61].

The calibration coefficient to convert the measured SID current to the absolute Cs evaporation rate strongly depends on the geometry and size of the filaments and on the relative position between the ionising filament w.r.t. the nozzle. The only way

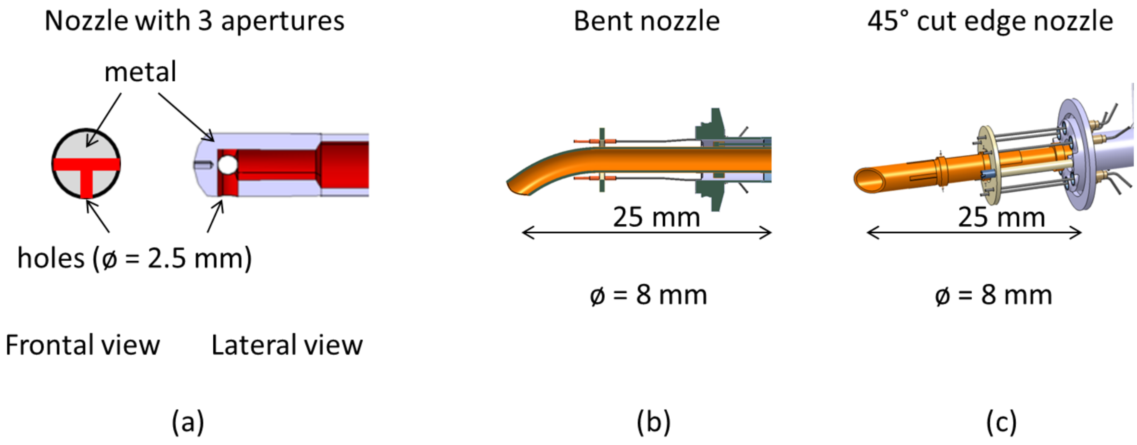

Figure 3.15: Three different nozzle geometries used at IPP test facilities: (a) and (b) used for the prototype source and (c) in use at the ELISE test facility.

to have an absolute estimation of the evaporation rate is to calibrate the system once the Cs oven ampoule is empty. By defining as Δt the total evaporation time achieved with an ampoule containing a total mass m_{Cs} of Cs, the instantaneous evaporation rate $\gamma\left(t\right)$ can be therefore retrieved by the equation:

$$\gamma\left(t\right) = I_{\mathrm{SID}}\left(t\right) \cdot \frac{m_{\mathrm{Cs}}}{\int_{t=0}^{\Delta t} I_{\mathrm{SID}}\left(t\right) dt}. \tag{3.35}$$

Since an ampoule can last up to several months, it is evident that during experimental operations of the source the SID can be used only for relative estimation of the evaporation rate. For the liquid Cs oven used at the RF prototype source, typical evaporation rates of $\sim 10\,\mathrm{mg/h}$ were estimated [62]. The SID measurements are of extreme importance during the source operation, since it is the only real-time measurement for monitoring the relative Cs evaporation rate from the oven.

For the simulation of the Cs dynamics in the source, the evaporation rate is of course an important input parameter, but it gives no information about the spatial distribution of the Cs outflow from the nozzle. The latter is a very important parameter, since the oven evaporation pattern determines the position on the source walls where Cs is deposited.

The position on the source walls where Cs is deposited is determined by the evaporation pattern of the oven: the Cs outflow profile is an relevant quantity that needs to be investigated to simulate the distribution of Cs in the source.

Different shapes of the oven nozzle were tested and used in the prototype source and in the larger source at the ELISE test facility. Figure 3.15 shows the three

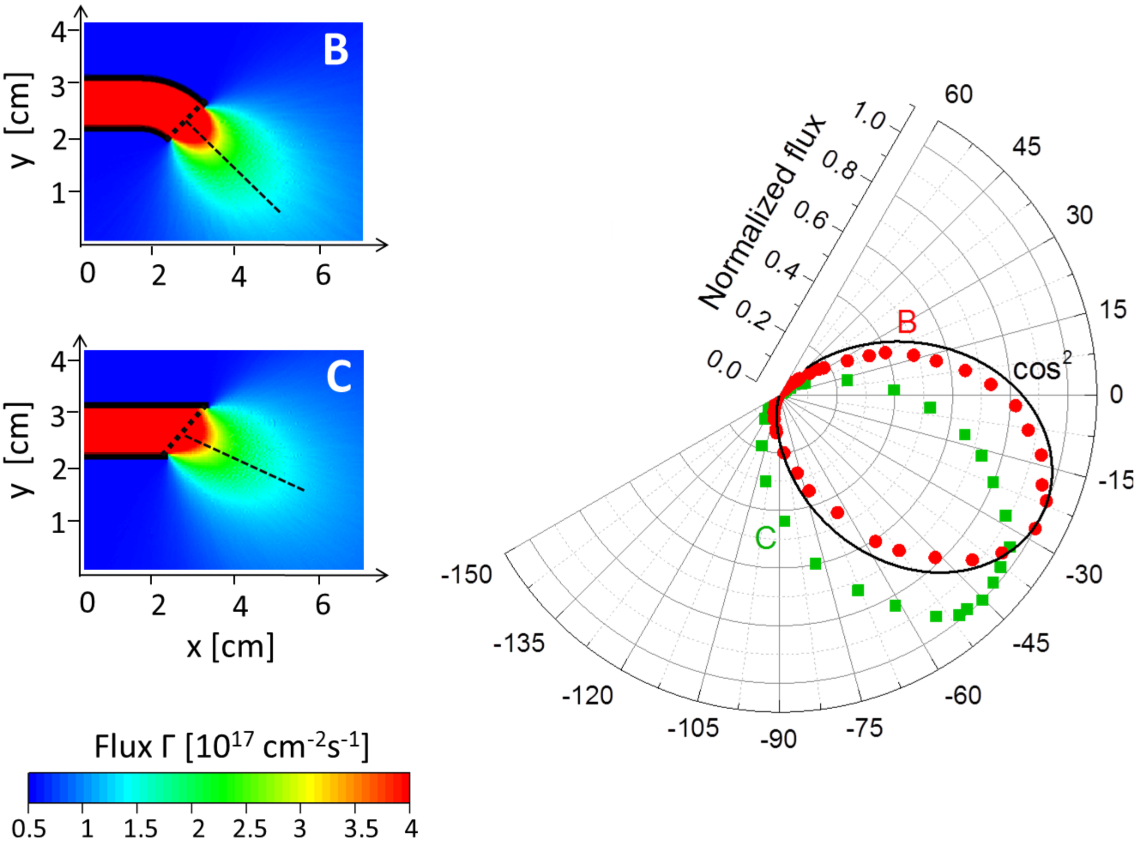

Figure 3.16: On the left, colour plot of the Cs flux intensity for the bent nozzle (b) and nozzle edge cut at 45 degree (c); on the right, polar plot of the normalized flux for the two geometries and the squared cosine fit.

typologies of nozzles:

(a) a pipe with 3 lateral holes ($\varnothing = 2.5\,\mathrm{mm}$), which allows evaporation of Cs to three directions;

(b) a bent pipe which is straight cut at the edge ($\varnothing = 8\,\mathrm{mm}$, length inside the source 25 mm);

(c) a pipe with the edge cut at 45° angle ($\varnothing = 8\,\mathrm{mm}$, length inside the source 25 mm)

Type (a) was used in the prototype source and it was now substituted by typology (b), while type (c) is currently used at the ELISE test facility. It has to be mentioned that the configurations (b) has been implemented with different bending angles in different experimental campaigns at the BATMAN test facilities (namely 50° and 35° downwards bending angle).

The flow regime which occurs inside the nozzle is a pure molecular flow, due to the high mean free path of Cs atoms w.r.t. the size of the pipe: in this condition Direct Simulation Monte Carlo (DSMC) [63] can be used to model the nozzle geometry and calculate the Cs outflow profile. Simulations for determining the pattern of the evaporated Cs were performed in the past only for the configuration (a), which shows a narrower evaporation profile w.r.t. the cosine distribution of an ideal orifice and can be approximated by a squared cosine distribution [8].

In this work calculations for the new nozzle geometries of the type (b) and (c) have been performed in order to have the respective input for the CsFlow3D code, to verify the presence of differences between the two geometries and if the squared cosine distribution obtained for the case (a) is also valid for (b) and (c).

The bending angle for configuration (b) was chosen to be 45° in order to be comparable with respect to the 45° edge cut of case (c). Figure 3.16 shows the colour plot of outcoming Cs flux for the two nozzle configurations and the polar plot of the normalised flux. The angle 0 corresponds to the horizontal direction, i.e. x axis. It can be observed that the direction at which the Cs flux is maximum is different for the two configurations: it occurs at 45 ° for the nozzle configuration (b), while it is ∼ 35 ° for case (c). Despite this shift, the flux profiles appears to be the same for both the configurations and can be fitted by a squared cosine.

3.4 Experimental diagnostics for investigation of Cs dynamics

In order to monitor and measure the amount of Cs in the source, both the test facilities BATMAN and ELISE are equipped with diagnostics based on two techniques: on one hand the detection of the radiation at the 852 nm Cs transition wavelength, on the other hand the radiation absorption from Cs via Tunable Laser Absorption Spectroscopy (TDLAS).

Detection of radiation at 852 nm

The atomic Cs can be excited from the ground state ($6^2\mathrm{S}_{1/2}$) to the excited state ($6^2\mathrm{P}$) via collision with an electron. This excited state is split into two levels due to fine structure, i.e. $6^2\mathrm{P}_{1/2}$, which results in a transition at 894 nm and the $6^2\mathrm{P}_{3/2}$, which results in a transition at 852 nm (D_2 resonant line). The latter transition (852 nm) is normally used due to the higher sensitivity of spectrometers at this wavelength with respect to 894 nm. By defining $i = 6^2\mathrm{P}_{3/2}$ and $k = 6^2\mathrm{S}_{1/2}$, the emissivity $\epsilon_{\mathrm{i,k}}$ for this transition is given by:

$$\epsilon_{\mathrm{i,k}} = n_{\mathrm{i}} A_{\mathrm{i,k}} \tag{3.36}$$

where n_{i} is the density of Cs in the excited state ($6^2\mathrm{P}_{3/2}$) and $A_{\mathrm{i,k}}$ the Einstein coefficient for spontaneous emission of the transition. Equation 3.36 allows for the calculation of the density of the excited state. In order to be able to calculate also the density of the ground state, a population model is needed.

Depending on the range of plasma parameters such as electron density and temperature, different population models, which relate the densities of the different energy states by taking in consideration the excitation and de-excitation processes, can be applied. For the typical regime of negative ion sources, in which the electron density is between 10^{17} - $10^{18}\,\mathrm{m}^{-3}$, the so called *collisional radiative* model has to be applied to quantitatively evaluate the optical spectroscopy measurements for the sources at the IPP test facilities [64].

Equation 3.36 can be written as function of the ground state density by inserting an effective rate coefficient $X_{\mathrm{i,k}}^{eff}$, which depends on the plasma parameters (i.e. electron density n_e and temperature T_e):

$$\epsilon_{\mathrm{i,k}} = n_{\mathrm{k}} n_{\mathrm{e}} X_{\mathrm{i,k}}^{eff}\left(n_e, T_e, ...\right) \tag{3.37}$$

where n_{k} is the density of atomic Cs in the ground state. The emissivity can be measured by integrating the Cs line detected by optical emission spectroscopy. By calculating the rate coefficient with the collisional radiative model, the ground state density can then be retrieved. For this procedure an accurate knowledge of the plasma parameters which appear in the rate coefficient is needed. However, when the plasma parameters can be considered constant, the emissivity itself represents a relative measurements of Cs density in the source.

For monitoring of the Cs amount in the source, photodiodes are used to detect the light in the range of the emission line of neutral Cs. Figure 3.17 shows a simple schematic of the system: the plasma light is collected by means of a lens, focused onto an optical fibre and detected by a photodiode. An interference filter is used to collect only the light in the range of 852 nm. The signal measured by the photodiode is proportional to the light intensity $I\left(\lambda\right)$ collected by the telescope, weighted by the spectral transmittance $T\left(\lambda\right)$ of the interference filter:

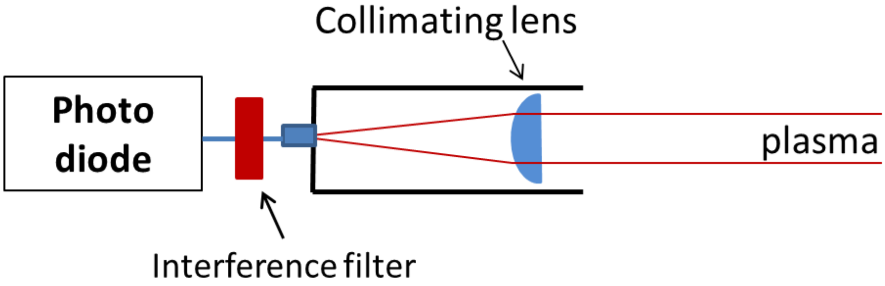

Figure 3.17: Scheme of the acquisition of light emission around 852 nm by means of an interference and a photodiode.

$$\int I(\lambda) T(\lambda) d\lambda \tag{3.38}$$

The transmittance of the interference filter is peaked at 852 nm and has a full width half maximum of ∼10 nm. In addition to Cs, in this range also molecular emission of hydrogen occurs [65]: this can produce an offset in the photodiode signal. Despite the fact that this set-up is not suitable for quantitative physical investigation on Cs distribution, it can be very useful for the source operator in order to have a real time feedback on the condition of the source caesiation, together with the signal of the oven nozzle SID.

Tunable Diode Laser Absorption Spectroscopy

In order to have a quantitative measurement of Cs atomic density, independently from the plasma parameters and available both during plasma and in vacuum, the measurement of the absorption spectrum of Cs instead of the emission can be used. This can be achieved by means of the Tunable Diode Laser Absorption Spectroscopy. This technique is based on the measurement of the absorption of radiation through an absorbing medium. When the light of spectral intensity $I(\lambda, 0)$ crosses the homogeneous medium of length L, the intensity after the medium is reduced to the value:

$$I(\lambda, L) = I(\lambda, 0) \exp\{-\tau(\lambda, L)\} \tag{3.39}$$

with τ the optical depth given by:

$$\tau(\lambda) = L \left(\frac{\lambda_0^4}{8\pi c} \frac{g_i}{g_k} A_{ik} \right) n_k P(\lambda) \tag{3.40}$$

where λ_0 is the center wavelength of the transition, A_{ik} the Einstein coefficient, g_i and g_k the degeneracies of the levels, n_k is the ground state density and $P(\lambda)$ is the normalized line profile of the transition, i.e.:

$$\int_0^\infty P_{\text{line}}(\lambda)\, d\lambda = 1 \tag{3.41}$$

An integration of equation 3.40 leads to the calculation of n_k:

$$n_k = \left(\frac{8\pi c g_k}{\lambda_0^4 g_i A_{ik}}\right)\frac{1}{L}\int_{line} \ln\left(\frac{I(\lambda,0)}{I(\lambda,L)}\right) d\lambda \tag{3.42}$$

This concept can then be applied to the D_2 resonant transition of Cs at 852 nm between the ground state $6^2S_{1/2}$ and the excited state $6^2P_{3/2}$. The ground state is split in two levels by hyperfine structure with total angular momentum quantum number which is $F = 3,4$ and the excited state $6^2P_{3/2}$ is split into four hyperfine levels with $F = 2,3,4,5$. Taking into account the selection rules (i.e. $\Delta F = 0, \pm 1$), the D_2 line has an hyperfine structure consisting of six lines. Because of Doppler broadening some of these lines overlap, resulting in two resolvable peaks which can be considered Gaussian: the wavelength distance between the peaks is 21.4 pm and the full width at half maximum, due to Doppler broadening, is around 2 pm at 1000K [66], as shown in figure 3.18.

Both in the BATMAN and ELISE test facility Tunable Diode Absorption Spectroscopy (TDLAS) for the evaluation of atomic Cs density has been implemented. A distribute feedback laser (DFB) diode is used as light source, since it has a sufficiently narrow linewidth ($<$ 0.1 pm) to resolve the two absorption peaks shown in

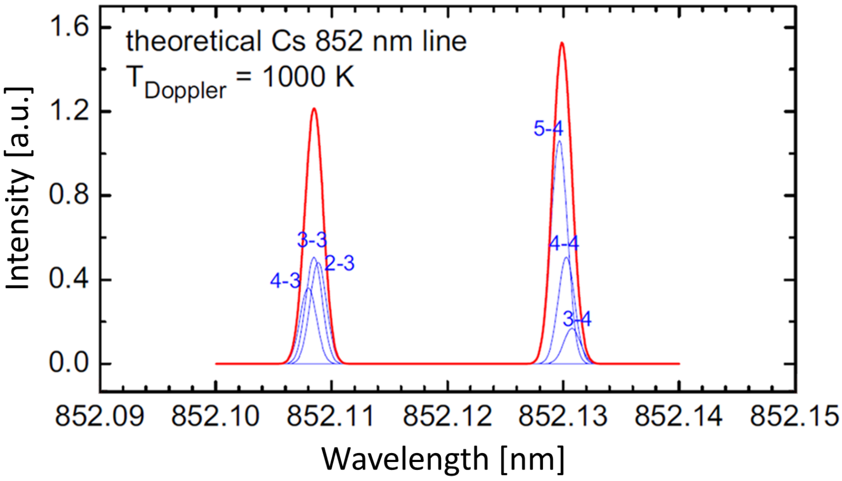

Figure 3.18: D_2 resonant line of Cs with the Doppler broadening in high resolution.

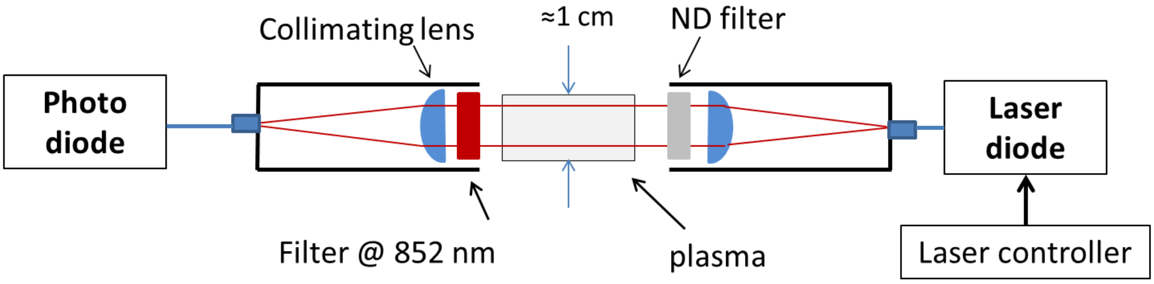

Figure 3.19: Scheme of the experimental apparatus used for TDLAS at the IPP test facilities.

figure 3.18 without further broadening. A scan in wavelength around the D_2 line of Cs is achieved by using a distributed feedback laser diode tunable between 851 nm and 853 nm: the coarse tuning is made by controlling the working temperature of the diode, while the fine scan in wavelength is done by modulating the current flowing through the diode.

A schematic of the set-up is shown in figure 3.19. The light emitted by the laser is collected by an optical fiber, coupled to a lens at the exit side, in order to create a collimated beam which is attenuated by a ND filter before crossing the medium. This filter is needed to attenuate the laser light intensity enough to avoid the depopulation

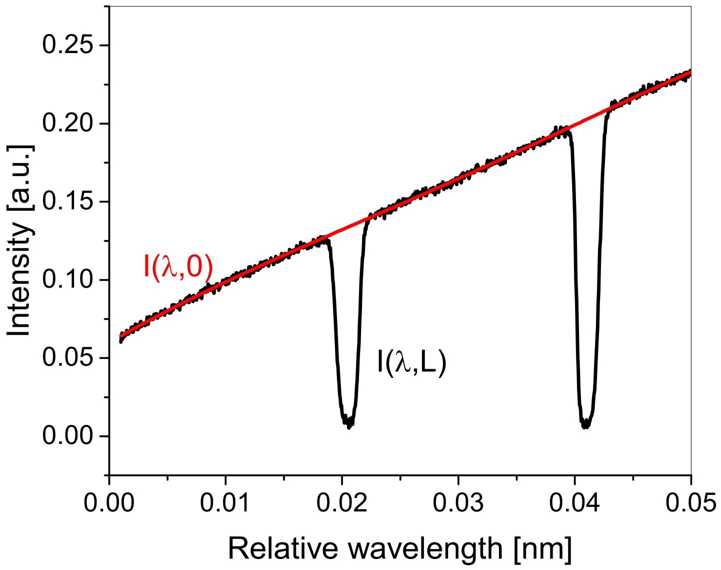

Figure 3.20: Experimental Cs absorption spectrum measured with the TDLAS. The baseline fitting is highlighted in red.

of the ground state, which could lead to an underestimation of the Cs density [66]: the resulting laser power is then below 1 mW. The transmitted light is collected and focused into another optical fiber, reaching a photodiode that acts as a detector. An interference filter is also used to avoid collecting the plasma light outside the wavelength range of interest.

Figure 3.20 shows an absorption spectrum measured with this set-up: the two absorption peaks of Cs are clearly visible. In order to retrieve the ground state density of atomic Cs, it is necessary to know the emission intensity of the laser light entering the medium $I\left(\lambda, 0\right)$: this value is obtained by fitting the base line emission of the laser with a polynomial function, without taking into account the region where the absorption peaks occurs. This procedure can be performed for each absorption spectrum, in order to avoid errors due to drift of electronics driving the laser diode, which can change the base line emission during the operations. The temporal resolution is of the order of 10 Hz [66].

4 Benchmark of CsFlow3D at the BATMAN test facility

The CsFlow3D code has been benchmarked against the data of the BATMAN test facility, which can in fact provide measurements of the line averaged neutral Cs density along dedicated lines of sight by means of the TDLAS. In such a way a quantitative comparison with the simulation results is possible.

In all the standard investigations performed with CsFlow3D for the prototype source, the caesium evaporation rate was kept constant at 10 mg/h, as stated in section 3.3. The temperature of the source surfaces is set at 35 °C, except for the plasma grid, which is set at 150 °C (typical values used during the experiments).

The effects of the Cs oven positions and orientations on Cs dynamics and on the conditioning process of the source are studied. Scans of the input parameters such as the plasma density, temperature and potential profiles inside the source were also performed, to quantify their influence on the Cs distribution inside the source.

4.1 Simulation of a single pulse

For the simulations the standard Cs evaporation configuration is considered, i.e. the Cs oven is located on the top part of the backplate of the source and the Cs evaporation is directed towards the plasma grid (section 3.3). The downwards bending angle of the nozzle is 50° and its length inside the source is 2.5 cm. At the beginning of the simulation there is no Cs deposited on the source surfaces: this situation corresponds to a completely clean source at the beginning of the experimental campaign. The aim of these simulations is to compare the Cs fluxes onto the PG that are achieved during the different operative phase (vacuum and plasma) and evaluate the effect of the direct evaporation w.r.t. the Cs released by the plasma. For this no plasma drift was considered in this simulations, while it will be introduced when comparing the code results with the experiments in section 4.2.

The vacuum phase length is set to 240 s, a typical value used in standard experiments. Figure 4.1 (a) shows a colour contour plot of the caesium flux during the vacuum phase onto the surface where the plasma grid (PG) is located. The area of the plasma grid is indicated by the black contour in the figure. The evaporation pattern of the oven is clearly visible on the top of the plasma grid. The evaporation cone is quite narrow due to the square cosine distribution of the oven evaporation profile and the peak flux onto the projection of the nozzle reaches a maximum value of $\sim 10^{13}\,\mathrm{cm^{-2}s^{-1}}$.

After the vacuum phase, a plasma pulse of 8 s is simulated: in this condition the transport of caesium towards the plasma grid changes due to the collisions with the hydrogen gas and plasma particles and due to the additional caesium source term provided by plasma contact with the caesiated surfaces (see section 3.1). The change in the caesium distribution during the plasma phase w.r.t. the vacuum phase can be observed in figure 4.1 (b), which shows the distribution of the total caesium flux (i.e. both neutral Cs and $\mathrm{Cs^+}$ ions) onto the plasma grid after 2 s of plasma. The highest values of the Cs flux are now closer to the center of the source, where the plasma is more intense and so the plasma assisted redistribution is more effective. The ionic

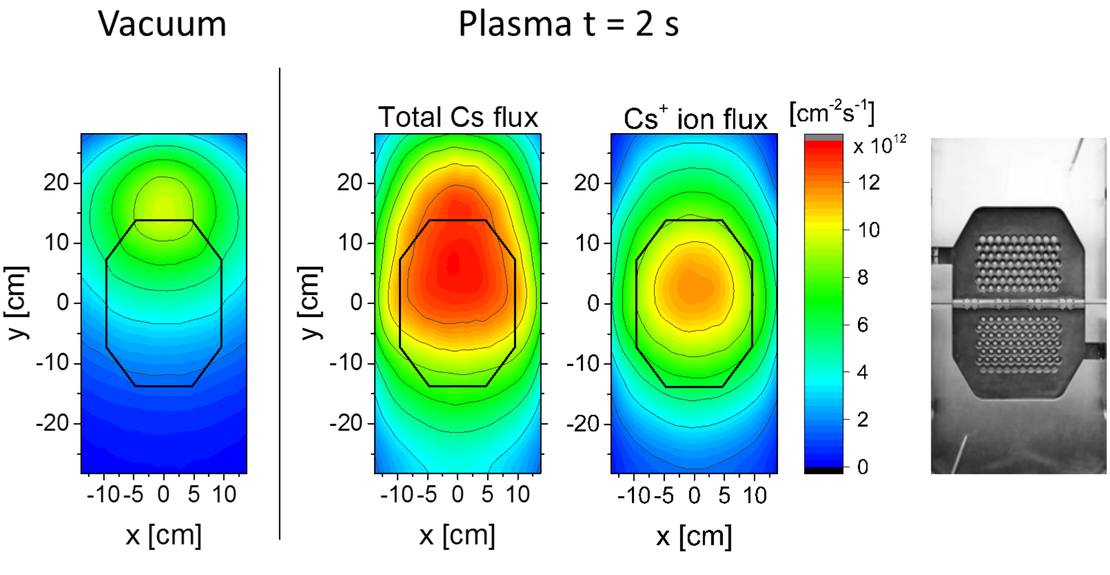

(a) (b) (c)

Figure 4.1: (a) Cs flux onto the plasma grid (PG) surface during the vacuum phase. The black contour indicates the plasma grid area; (b) Total Cs flux (neutral Cs and $\mathrm{Cs^+}$) onto the PG surface in plasma at t = 2 s; (c) $\mathrm{Cs^+}$ ion flux onto the PG surface in plasma at t = 2 s.

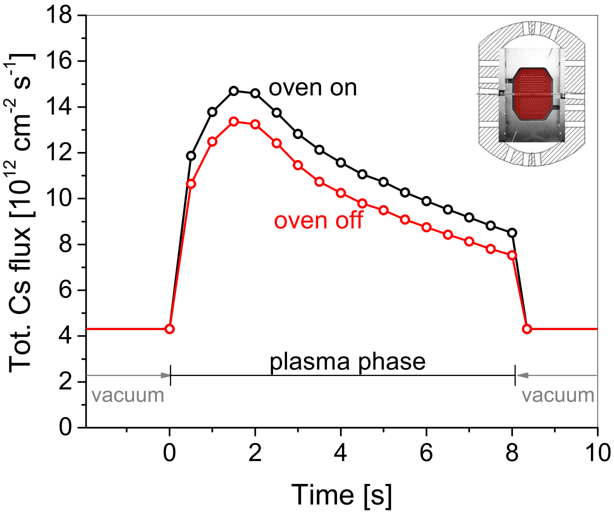

Figure 4.2: Total Cs flux averaged onto the plasma grid area vs. time for the case with the oven evaporating also during the plasma phase (oven on) and with the oven turned off during the plasma phase (oven off).

component of the Cs flux onto the the plasma grid is shown in 4.1 (c): by comparing these values with the total flux, it can be seen that most of the Cs that reaches the plasma grid is ionized. The ionization fraction changes over the plasma grid, since it depends on the plasma parameters (appendix A) and on the different transport of neutral Cs and Cs ions: the maximum $\mathrm{Cs}^{+}/\mathrm{Cs}$ fraction resulted in $\sim 80\%$.

Figure 4.2 shows the time evolution of the total caesium flux averaged on the plasma grid area. The RF is turned on at $\mathrm{t}=0\,\mathrm{s}$. The black curve (oven on) indicates the results for a continuous caesium evaporation also during the plasma phase, the red one (oven off) is obtained by stopping the caesium evaporation during the plasma phase. In such a way it is possible to decouple the contribution of the direct evaporation from the oven and the plasma redistribution. The total flux averaged onto the plasma grid area Γ during the vacuum phase is $4.3{\cdot}10^{12}\ \mathrm{cm}^{-2}\mathrm{s}^{-1}$ and it is basically determined by the oven evaporation rate and the sticking coefficient (0.7), i.e. the loss of Cs on the walls. In the beginning of the plasma phase the total flux increases and reaches a maximum of $13.4{\cdot}10^{12}\,\mathrm{cm}^{-2}\mathrm{s}^{-1}$ for the oven off case and $14.7{\cdot}10^{12}\,\mathrm{cm}^{-2}\mathrm{s}^{-1}$ for the oven on case. The difference between this two values ($\sim 1.3 \cdot 10^{12}\,\mathrm{cm}^{-2}\mathrm{s}^{-1}$) is almost constant during the pulse and represents the contribution of the direct flux from the oven, which is less than 10% of the total flux reaching the plasma grid. Therefore most of the caesium ($\sim 90\%$) that reaches the plasma grid during the pulse comes from plasma redistribution, which is the most relevant term for Cs dynamics in plasma.

A temporal evolution of the caesium flux during the plasma phase can also be observed: it is important to remark that the plasma parameters in the simulation are kept constant during all the plasma phase, so this evolution is not related to changes of the plasma. The temporal behaviour of the flux can be caused only by the distribution of the Cs reservoirs, i.e. the deposited Cs on the source inner walls. During the first two seconds caesium is redeposited to places where it is easily removed by the plasma and transported onto the plasma grid, resulting in an increase of the flux. Afterwards the Cs reservoirs accessible to the plasma get depleted and cannot sustain anymore the original flux, which consequently decreases during the rest of the plasma phase. After switching off the plasma, the value of the flux is again the same as the previous vacuum phase due to the direct evaporation from the oven.

These results show that the vacuum and plasma phase are strongly decoupled: in vacuum the Cs dynamics is determined by the oven evaporation, while in the plasma the dominant factor is the redistribution of the Cs deposited on the walls.

4.2 Comparisons with experiments

The previous results were obtained by considering a clean source (i.e. no Cs deposited on the source walls) and by simulating only one vacuum phase followed by a plasma phase. The source conditioning during the experiments is a process that requires the repetition of many cycles of vacuum and plasma phase with continuous Cs evaporation, in order to achieve a high extracted negative ion current density while limiting the co-extracted electron current density below that of negative ions. An example of the experimental conditioning process is shown in figure 4.3: the plot (a) shows the detected emission at 852 nm where the neutral Cs emission line is located, averaged along a vertical line of sight close to the PG; the plot (b) shows the evolution pulse by pulse of the extracted negative ion current density j_{H^-} and the co-extracted electron current density j_{e}. All the values of current and emissions of figure 4.3 are averaged on the second half of the extraction phase.

All the shots during the conditioning phases were performed at constant operational parameters, in particular a pressure of 0.3 Pa and RF power of 60 kW. Cs evaporation from the oven started at the pulse number 102612: the Cs emission signal observed before is not zero due to the background emission of molecular hydrogen in the same wavelength range [65]. After the beginning of Cs evaporation the Cs emission increases and so the amount of Cs inside the source: different stages in the increase of Cs emission can be observed, due to the stepwise increase of the Cs oven temperature (i.e. Cs evaporation rate) up to the final operational value. This stepwise increase of the Cs oven reservoir temperature was performed in order to follow experimentally with more resolution the conditioning process. Consequently to the increase of the Cs amount in the source, a progressive improvement of the performances occurs: the extracted ion current density increases due to the increase of the negative ions created by surface production on the PG, while the co-extracted electrons decrease.

In order to have a benchmark of the CsFlow3D code, the experimental measurements of line averaged neutral Cs density of the TDLAS are compared with the simulated density obtained by the CsFlow3D code for a well-conditioned source, i.e. after the repetition of many cycles of vacuum and plasma phases, when a stable regime is reached.

The vertical plasma drift due the magnetic filter field, which is observed experi-

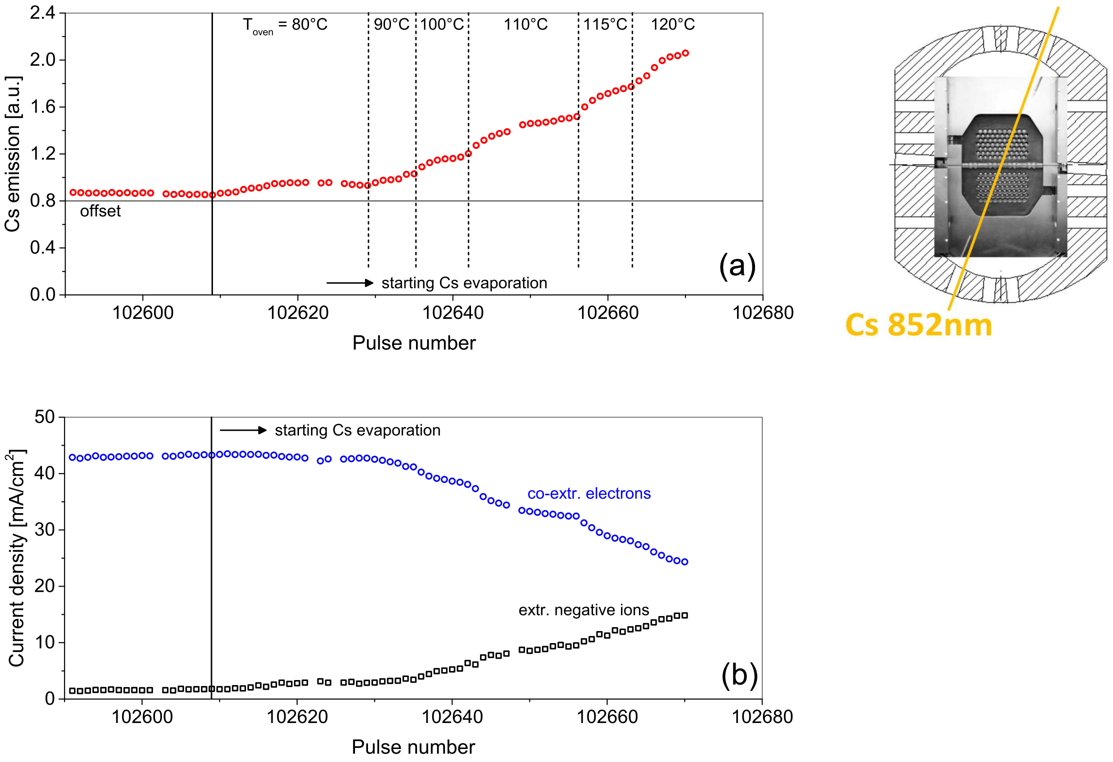

Figure 4.3: (a) Negative ion current density and co-extracted electron to ion current ratio vs. pulse number during the conditioning phase; (b) Intensity of Cs emission line (852 nm) vs. pulse number during the conditioning phase.

mentally [34], needs to be taken into account. A simple way of modelling the plasma drift in the code is to consider a vertical shift $\Delta y\,(z)$ that depends linearly on the distance from the plasma grid. The shift is maximum at the PG, where the magnets are located, Δy_{max}, and it is set to zero at the driver position. Figure 4.4 shows a sketch of the protoype source where the shift parameter Δy along the source axis is indicated and an example of the shifted density profile in front of the plasma grid is presented. In the sketch the positions of the permanent magnets and of the two Langmuir probes for the measurements of plasma parameters are also shown.

A maximum shift $\Delta y_{\mathrm{max}} = 10\,\mathrm{cm}$ is chosen, which is in agreement with the experimental measurements of the Langmuir probes. The conditioning phase was simulated by repeating 20 times the standard pulse (i.e. 240 s vacuum phase and 8 s plasma phase) consecutively and with constant Cs evaporation of 10 mg/h.

Figure 4.5 (a) shows the comparison with TDLAS measurements for the 20th pulse: full lines represent the experimental data while dashed line the simulation. Figure 4.5 (b) shows in addition the time traces of the discharge parameters, i.e. pressure and power.

In the experimental time traces an overshooting of Cs density can be observed at the very beginning of the pulse: this is correlated with a variation of the gas pressure, which is increased before starting the plasma to facilitate the ignition, and

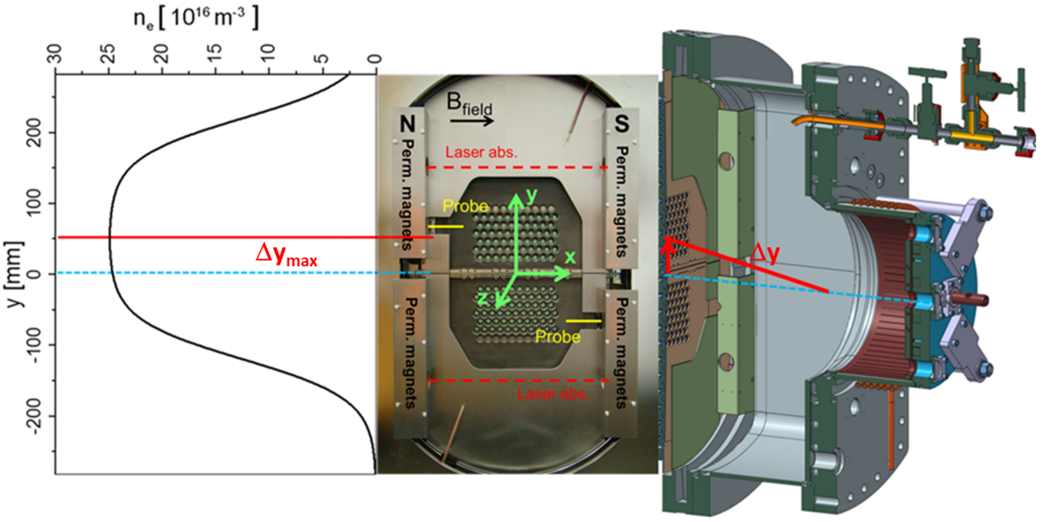

Figure 4.4: Sketch of the prototype source at the BATMAN test facility: the location of permanents magnets and of the Langmuir probes is highlighted and a shifted profile of plasma density is shown on the left.

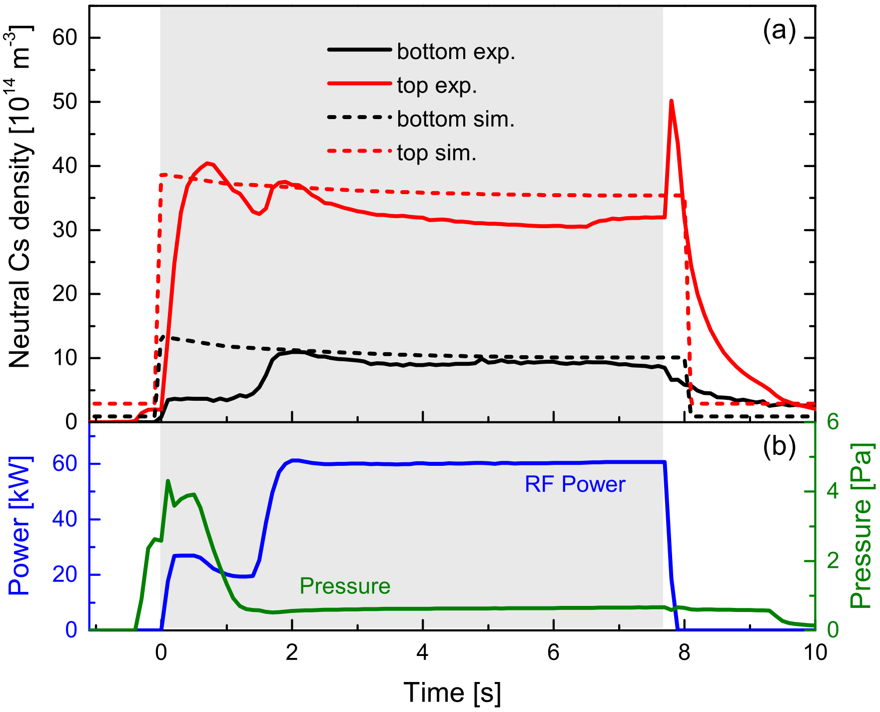

Figure 4.5: Neutral Cs density in the top and bottom line of sight as result of the simulations (dashed line) and of the experimental measurement (solid line). The simulation for a plasma displacement $\Delta y_{\max} = 10\,cm$ was assumed.

the RF power, which is increased stepwise up to the nominal value. These technical restrictions for the plasma ignition are not simulated by the code. Another peak is visible for the top line of sight immediately after the end of the pulse. Although there is still not a clear explanation of the origin of this peak, which does not appear in every pulse, the following hypothesis has been formulated. The laser absorption spectroscopy is sensitive only to neutral Cs: during the pulse a large fraction of Cs is ionised and cannot be detected. Immediately after switching off the RF, there might still be a high Cs flux from the walls, but due to the absence of ionisation it can be detected as a peak in the TDLAS signal. This flux decays after the end of the pulse with a decay time of the order of seconds, as it can be observed in the decay of the TDLAS measured density. It can also indicate a temporal dynamic of the desorption or of the sticking coefficient after the plasma phase. The time traces indicate also that this effect varies locally: it is in fact not observed for the bottom line of sight in this specific shot. In first approximation this effect is not considered in the code.

The simulations (dashed lines) appear in very good agreement with the experimental time traces (full lines) for both the top and bottom lines of sight and the code can reproduce the vertical asymmetry of neutral Cs density which is observed experimentally by the TDLAS. Since achieving a better symmetry of the Cs distribution onto the plasma grid can be helpful in reducing the Cs consumption, the physical mechanisms affecting Cs distribution need to be investigated. It has been previously shown (figure 4.2) that most of the Cs released during the vacuum phase comes from the plasma assisted erosions of the Cs deposited on the walls. This means that the Cs distribution in plasma is a consequence of:

- the position of the Cs reservoirs in the sources and in the amount of Cs deposited, which is determined by the sticking coefficient and the location and orientation of the Cs ovens;
- the plasma parameter profiles, i.e. the distribution of the plasma inside the source.

Dedicated investigations of these phenomena by means of the CsFlow3D code will be given in the next sections.

4.2.1 Role of sticking coefficient

One of the factors that affect the amount of deposited Cs on the inner surfaces is the sticking coefficient: in the standard case with the source wall temperature at 35°C the sticking probability of Cs used by the code is 0.7 (as described in chapter 3). This parameter is based on experimental data but it is strongly dependent on the amount of impurities present on the surfaces so it is important to evaluate how much a variation of the sticking will affect the Cs dynamics. In the vacuum phase a decrease of the sticking will determine an increase of the Cs fluxes, since the loss to the walls is decreased. During the plasma the effect is more complex, since a lower sticking leads also to a lower amount of Cs available for the redistribution, so it can affect also the stability.

A sticking coefficient scan between 0.1 and 0.9 was performed for a standard plasma pulse of 8 s with a previous vacuum phase of 240 s. No shift in the plasma parameters was considered in these analysis. Figure 4.6 (a) shows the total Cs flux averaged on the PG area as a function of time for the different values of sticking coefficient. As expected, during the vacuum phase a lower sticking coefficient is associated with a higher flux, because of the decreased loss to the walls. The same trend is observed also during the plasma phase, but the temporal evolution is strongly

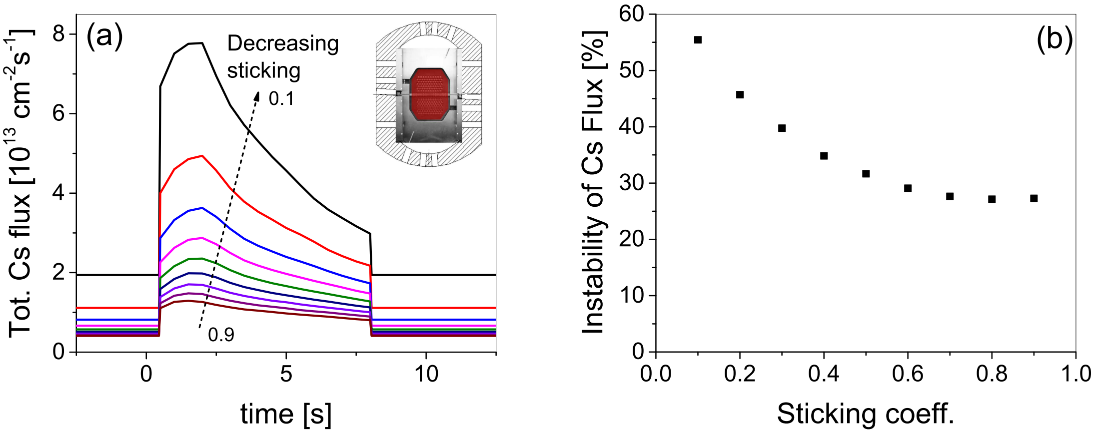

Figure 4.6: (a) Total Cs flux averaged on the PG area vs. time for different sticking coefficients; (b) Instability of the Cs flux during the pulse as a function of the sticking coefficient.

dependent on the sticking coefficient: the Cs flux is considerably less stable for lower sticking coefficients.

Figure 4.6 (b) shows a plot of the flux instability defined as $(\Gamma_{\mathrm{START}} - \Gamma_{\mathrm{END}})/\Gamma_{\mathrm{START}}$ as a function of the sticking coefficient. The instability is clearly higher for low sticking coefficient values: in these cases the amount of Cs deposited in the source inner walls is lower and so a faster depletion of the Cs reservoirs during the plasma phase occurs. The instability reaches a flat level of around 30% for sticking larger than 0.6.

Thus, the sticking coefficient is a parameter with a huge influence on the Cs dynamics. It is also worth to mention that in reality the sticking probability might be a local property of the surface and not a global value as assumed in the code.

4.2.2 Role of Cs reservoir location

The position of the Cs reservoir that provides Cs for the plasma redistribution can also affect the amount and the stability of the Cs flux onto the plasma grid. The location of the reservoirs can be changed by changing the orientation of the Cs evaporation: simulations were performed by varying the bending angle of the Cs oven nozzle positioned on the top of the back-plate.

A standard pulse of 8 s with a previous 240 s vacuum phase was simulated for four downward bending angles of the nozzle: 0° (horizontal), 25°, 50° and 75°. In order to investigate exclusively the effect of the Cs reservoirs positions, no vertical shift in the plasma parameters was considered. Figure 4.7 shows the total Cs flux averaged on the

PG area as a function of time. The different values during the vacuum phase depend on the projection of the evaporation pattern from the nozzle onto the PG surface and it resulted maximum for the 50° case. During the plasma phase, both the absolute value of the flux and the time evolution is very sensitive to the bending angle: the case 0° (horizontal nozzle) is strongly unstable, while the stability is considerably higher for the case at 50° and 75°. The time at which the maximum flux is reached shows also a dependence from the bending angle: for the 0° case the depletion of the reservoirs starts already at $t = 0.5\,\mathrm{s}$, while with the nozzle at 75° it starts later, i.e. at $t = 3\,\mathrm{s}$. Since the direct flux from the oven contributes for less than 10%, this dependence on the bending angle comes from the different location of the Cs reservoirs. All these observations suggest that in the case of 50° and 75° the Cs reservoirs on the wall can be better exploited w.r.t. to the lower bending angles.

Figure 4.8 shows the Cs coverage of one of the side walls of the prototype source (there is a left/right symmetry) for the different bending angle α of the Cs oven nozzle. In the top row the coverage before the pulse is plotted, while in the bottom the coverage after the 8 s pulse is shown.

The maximum coverage achieved after one vacuum phase of 240 s is $\sim 18{\cdot}10^{14}\,\mathrm{cm}^{-2}$, i.e. 4 monolayers (1 Cs monolayer onto Mo $\sim 4.5{\cdot}10^{14}\,\mathrm{cm}^{-2}$) and the position of the most covered area moves by changing the bending angle. By looking at the cover-

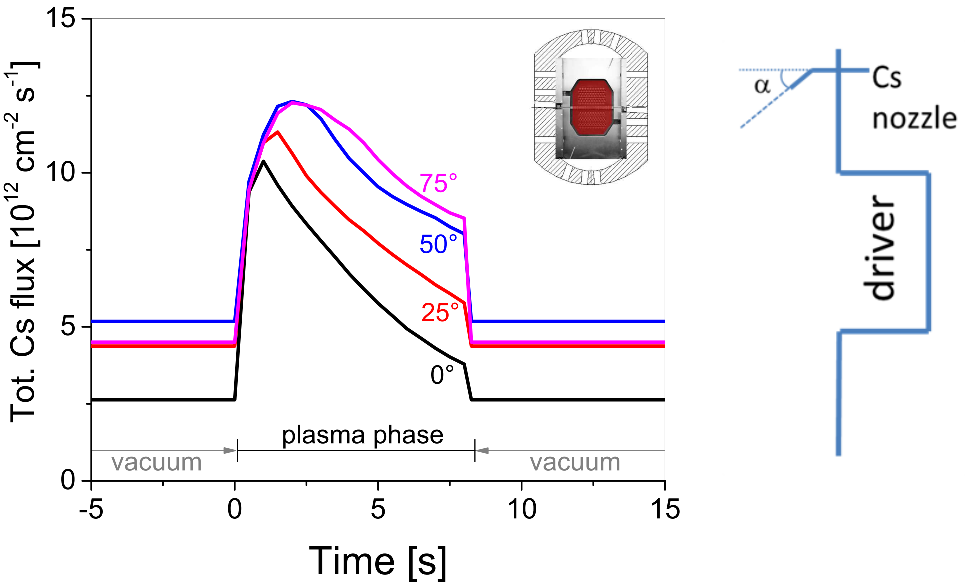

Figure 4.7: Total Cs flux (i.e. neutral Cs and Cs^+) averaged on the PG area vs. time for different orientation of the Cs oven nozzle positioned on the backplate.

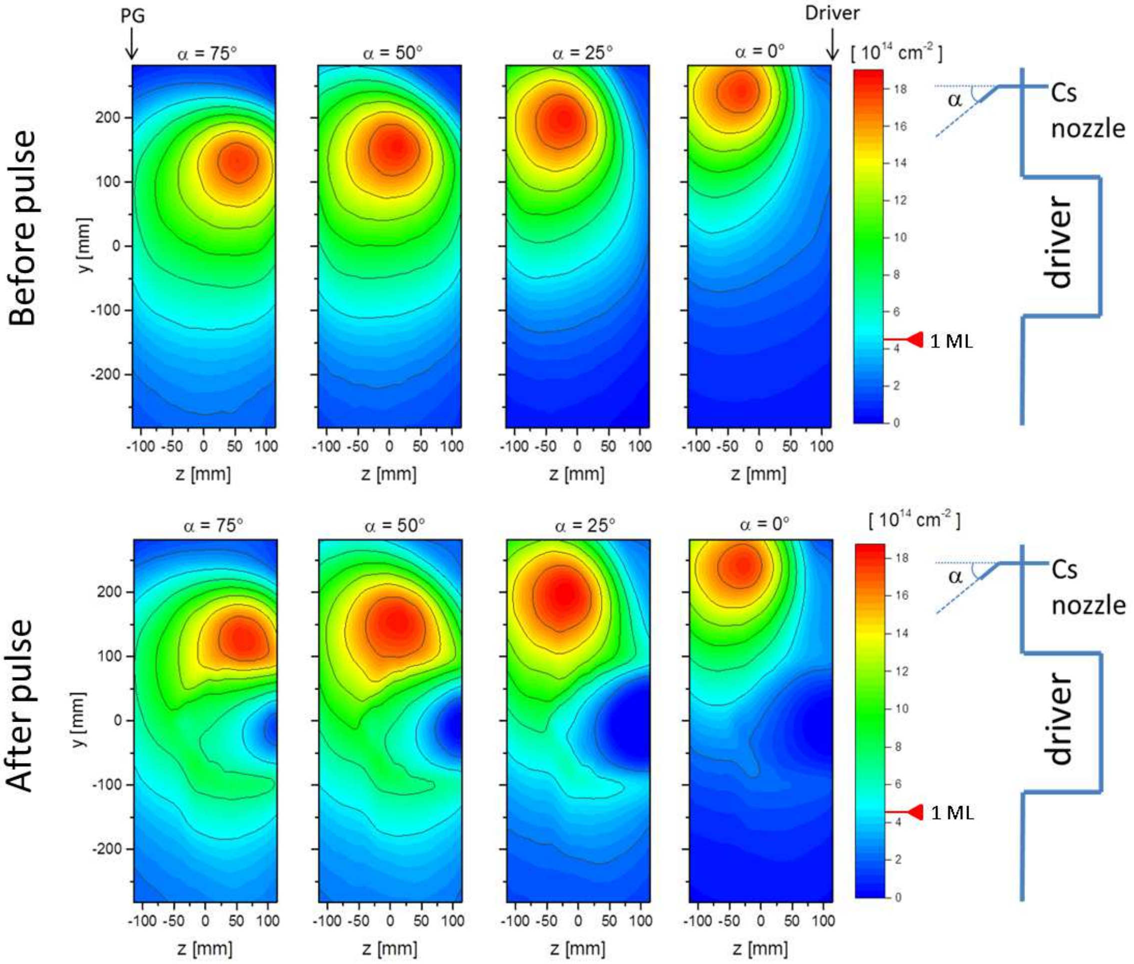

Figure 4.8: Cs coverage on the side wall of the prototype source immediately before the pulse (top) and immediately after the pulse at $t = 8\,\mathrm{s}$ (bottom), for different inclination angle alpha of the oven nozzle.

age plots immediately after the plasma phase, it is possible to identify the region of stronger Cs removal due to plasma contact, i.e. close to the driver exit, where the plasma density is higher. It is evident that the Cs coverage on these areas immediately before the pulse is higher for the 50° and 75° cases: the increased amount of Cs available for redistribution is therefore the reason of the increased flux onto the PG and of the better stability. After the plasma pulse the Cs depletion area is smaller compared with the other two cases at 25° and 0°, in which there is basically no more Cs left close to the driver exit.

The Cs removal on the sidewall of the source can be observed also experimentally during the opening and inspection of the source. Figure 4.9 shows a picture of the side wall of the expansion chamber, with the driver exit visible on the right. The

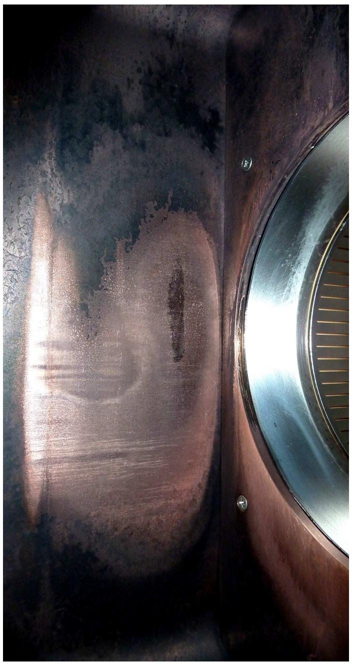

Figure 4.9: Picture of the inner side wall of the expansion chamber of the prototype source taken during an opening of the source. The driver exit is visible on the right.

dark brown and black regions are formed by high coverage of Cs compounds, which were either created already inside the ion source during the operation or due to the reaction with the atmosphere after the opening. A cleaner region in the centre of the side wall is visible in correspondence with the driver position where the plasma density is higher, which is in agreement with the code results of figure 4.8.

Positioning the Cs reservoirs on the side walls as close as possible to the driver exit, where the removal and redistribution is more effective, can significantly improve the stability of the Cs dynamics. An effective way of achieving this would be evaporating Cs from one of the ports located in the diagnostic flange of the expansion vessel, close to the plasma grid (see the sketch in figure 4.10 (a)). Simulations were therefore performed considering the Cs oven nozzle positioned on the uppermost port in the diagnostic flange. In order to evaporate towards the central part of the side wall, the Cs oven nozzle was bended downwards by 35°. In addition the nozzle can be rotated by an axial angle β in order to evaporate either towards the plasma grid (negative value of β) or towards the driver (positive value of β). The results are shown in figure 4.10 (b), where the total Cs flux averaged on the PG Γ is plotted as a function of time: the dashed line represents the reference case with the oven on the top of the backplate. It is evident that in all the cases with the oven on the side wall the Cs flux during the plasma phase is higher w.r.t. the reference case and the absolute value

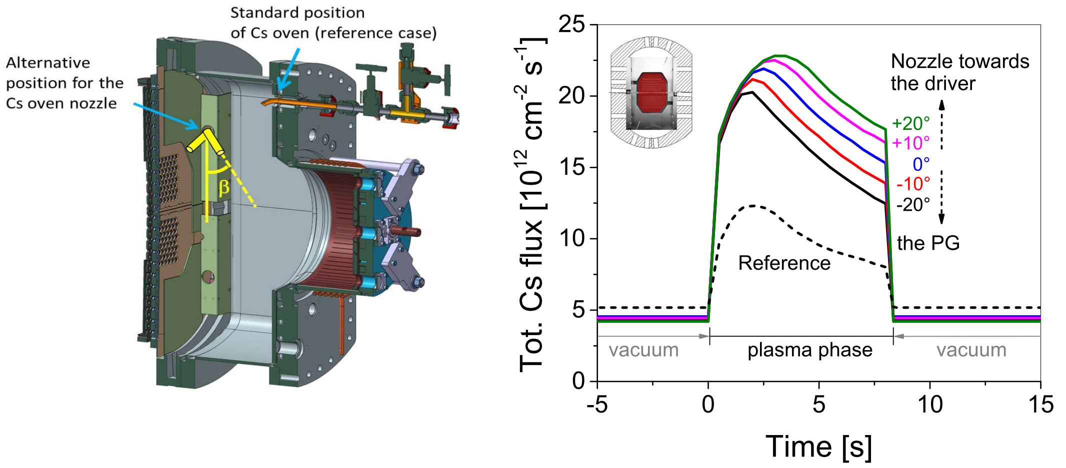

(a) (b)

Figure 4.10: (a) Sketch of the prototype source with the alternative oven nozzle position on the side wall (diagnostic flange); (b) total Cs flux averaged onto the PG area vs. time for different nozzle orientations of the Cs oven positioned on the side wall.

increases by rotating the nozzle towards the driver, i.e. by moving the Cs reservoirs closer to driver exit. In addition the decrease of the Cs flux starts later for the case in which the evaporation is directed towards the driver, as shown by the time at which the maximum flux is reached. These results confirm the observations of the previous simulations: it is better to have Cs reservoirs on the locations where the plasma (and therefore redistribution) is more intense.

4.2.3 Relation between plasma and Cs distribution in the source

The relation between the plasma distribution in the source and the Cs distribution was investigated by performing simulations of 20 consecutive standard pulses for different values of the shift parameter $\Delta y_{\mathrm{max}} = 0, 5, 6, 10, 15$cm. In order to evaluate the vertical asymmetry of neutral Cs density the vertical asymmetry index is defined as $\xi = (n_{\mathrm{top}} - n_{\mathrm{btm}})\,/\mathrm{min}(n_{\mathrm{top}} + n_{\mathrm{btm}})$. The index ξ is zero in a symmetric case and positive (negative) for the case $n_{\mathrm{top}} \geq n_{\mathrm{btm}}$ ($n_{\mathrm{top}} \leq n_{\mathrm{btm}}$). Figure 4.11 (a) shows the asymmetry index ξ as a function of the consecutive pulse number for the simulations with different values of Δy_{max}. ξ strongly increases with increasing Δy_{max}, showing clearly that a vertical plasma asymmetry results in an asymmetry in Cs distribution.

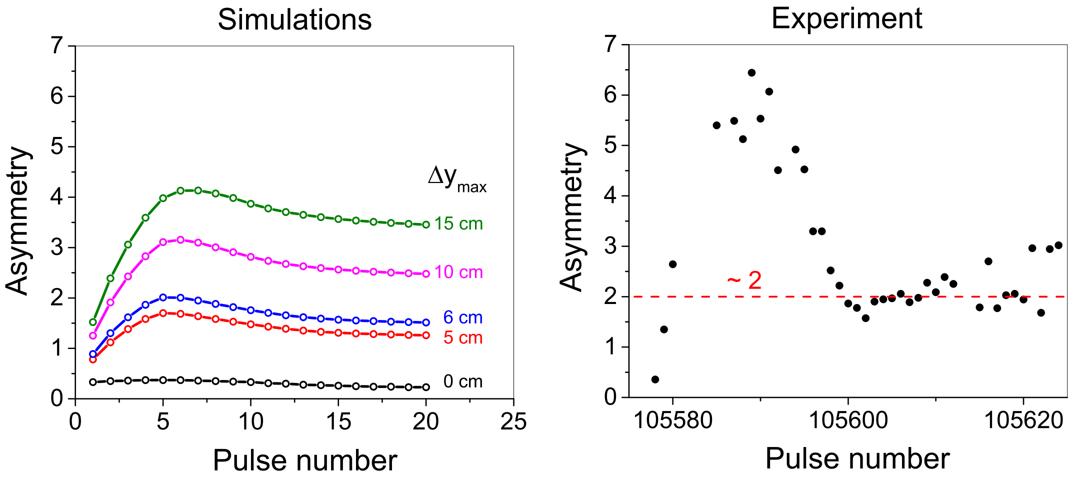

Figure 4.11: (a) Simulated Cs asymmetry index ξ vs. progressive pulse number, for different plasma displacement Δy_{max}; (b) Evolution of the experimental asymmetry during pulses (pressure 0.3 Pa, power 60 kW). Cs oven in the top of the backplate.

The measured vertical symmetry during a conditioning day is shown in figure 4.11 (b). After an initial peak, the experimental asymmetry tends to stabilise at a value around ~ 2. Comparing this value with the different simulations, the value of Δy_{max} for which there is agreement with the experiment is between 6 and 10 cm. These values are compatible with the Langmuir probe data, although the experiments show a much stronger dynamics before the saturation to the stable values w.r.t. the simulations.

The simulated conditioning process for the most asymmetric case compatible with the measurements ($\Delta y_{\text{max}} = 10$ cm) will be discussed in more details in the following. Figure 4.12 shows the neutral Cs density in the top and in the bottom line of sight averaged on time during the pulse phase for the two cases with an upward drift ($\Delta y_{\text{max}} = 10$ cm) and without drift. The density values in the bottom are very similar for the case with and without the drift. A more significant difference is observed for the top line of sight: in presence of the plasma drift the value of Cs that is reached at the 20th pulse is much higher w.r.t. to the no drift case (more than a factor of 3). It has been shown before that in the configuration with the oven on the top of the back-plate, the Cs reservoirs are located on the top part of the sidewalls (figure 4.8). When an upward drift of the plasma is included in the code, the areas on which Cs is removed due to the plasma contact are also shifted upwards and they will coincide with the position where the reservoirs are located: in such a way more Cs is available for the plasma assisted redistribution.

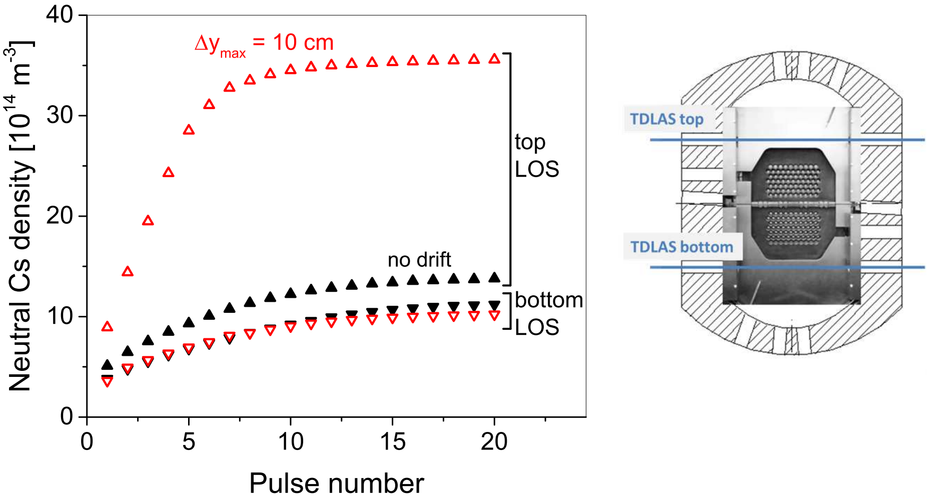

Figure 4.12: Simulated neutral Cs density in the top and bottom line of sight for the two cases: with plasma drift (black) and without plasma drift (red).

4.2.4 Combined effect of plasma asymmetry and oven position

Due to the interplay between the position of the Cs reservoirs and the plasma distribution in the source, the vertical Cs asymmetry previously observed could in principle be reduced by changing the position of the Cs reservoirs, in order to compensate the effect of the plasma drift.

Experiments were performed at the prototype source by using an additional Cs oven positioned on the bottom of the back-plate and evaporating towards the plasma grid (figure 4.13) [67]. Three different evaporation configurations were considered, i.e. evaporation only from top oven, only from the bottom one and the simultaneous evaporation from both the ovens. For each one of these configurations, calculations were performed with CsFlow3D for different plasma drift intensity, by varying the plasma shifting parameter Δy_{max} between 0 cm and 15 cm. In every configuration the total Cs evaporation rate inside the source was kept constant to the nominal standard value of 10 mg/h.

The experimental results are shown in figure 4.14 (a), where the measured Cs asymmetry index during the pulses of each day is plotted with open dots. Since there is an evolution of the asymmetry during the conditioning process, the dots are colour coded according to the pulse number, i.e. the last pulses of the day with a good and stable conditioning are represented by the one with more intense colour. The

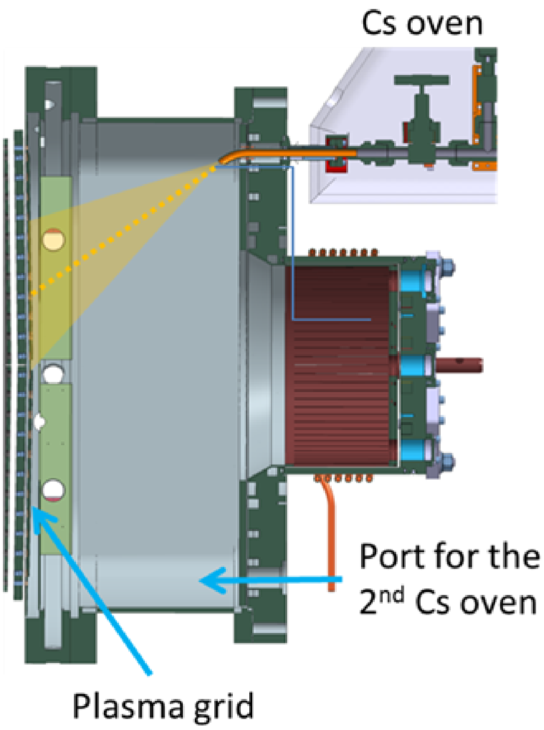

Figure 4.13: Vertical cut of the prototype source where the ports used for the Cs oven nozzle in the bottom are indicated.

rectangle represents the simulated asymmetry for the range of Δy_{max} between 5 cm and 10 cm, which are the values compatible with the Langmuir probe measurements. There is a similar trend between experiments and simulations: higher values of Cs asymmetry are observed for the top oven case, while the lowest values are observed for the bottom oven case. Simulations fit particularly good the data for the top oven case, while for the other two case the simulations shows higher positive asymmetry value.

The asymmetry index resulting from the simulations for the three configurations as a function of the maximum plasma shift Δy_{max} are shown in figure 4.14 (b). The general rule for which a higher vertical plasma asymmetry is associated with a higher vertical Cs asymmetry is still valid also when changing the position of the Cs reservoirs. In particular the values of the simulated asymmetry for $\Delta y_{\mathrm{max}} > 0$ cm are always positive: this means that in all the cases the value of Cs density is higher in the top w.r.t the bottom, i.e. Cs ”follows” the plasma. Some differences between the evaporation configurations can anyway be observed: the highest asymmetry values are obtained by using the top oven only, while the lowest asymmetry occurs when the evaporation is performed from the bottom oven only. When Cs is simultaneously

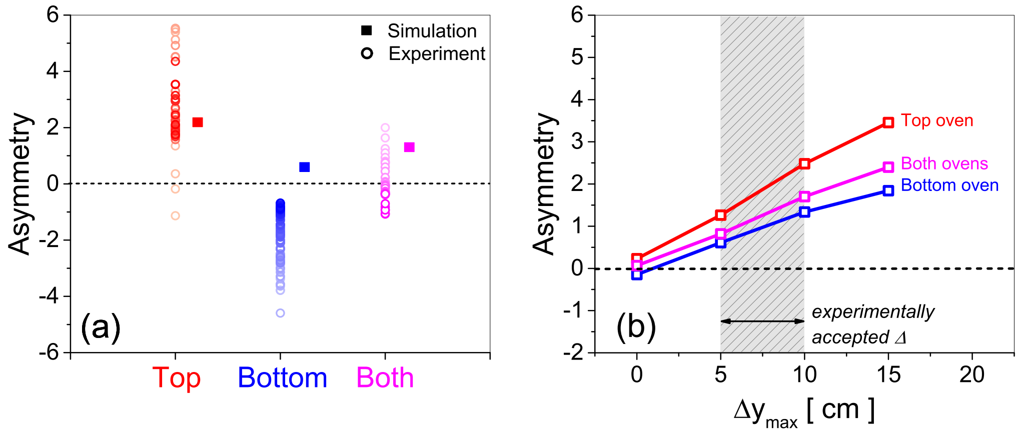

Figure 4.14: (a) Simulated Cs asymmetry index ξ as a function of the plasma displacement $\Delta y_{\max}$, for the three different oven configurations (i.e. only top oven, only bottom oven, both ovens); (b) Comparisons between experimental and simulated Cs asymmetry index ξ, for the same three oven configurations.

evaporated by both the ovens, i.e. with a symmetric distribution of the Cs reservoirs, the values of ξ lie in between the two previous cases.

The difference between experiment and simulation results in the case of the bottom oven and both oven configurations can be explained by the fact that in the simulations the total Cs evaporation rate inside the source was kept constant for all the configurations, while in the experiment the evaporation rate of the bottom oven had to be increased in order to reach good performances (i.e. to reduce the co-extracted electron current below the current of extracted negative ions). It was also observed experimentally that a larger number of pulses was needed when operating only with the bottom oven in order to reach the performance target.

In order to compare the conditioning process for the top and the bottom oven, the evolution pulse by pulse of the simulated neutral Cs density along the two horizontal lines of sight is plotted in figure 4.15. A vertical plasma displacement in front of the plasma grid $\Delta y_{\max}$=10 cm was considered in both cases. It is evident that when Cs is evaporated from the top, the conditioning (i.e. the achievement of a high and stable Cs density value) is much faster: along the top line of sight the Cs density has already reached the saturation level after around 10 pulses. In the case of the bottom oven the density is instead still increasing also after 20 pulses. In addition it can be observed that also in the bottom line of sight the amount of Cs is slightly higher when Cs is evaporated from the top oven.

The comparisons of the two different oven positions in relation with a presence

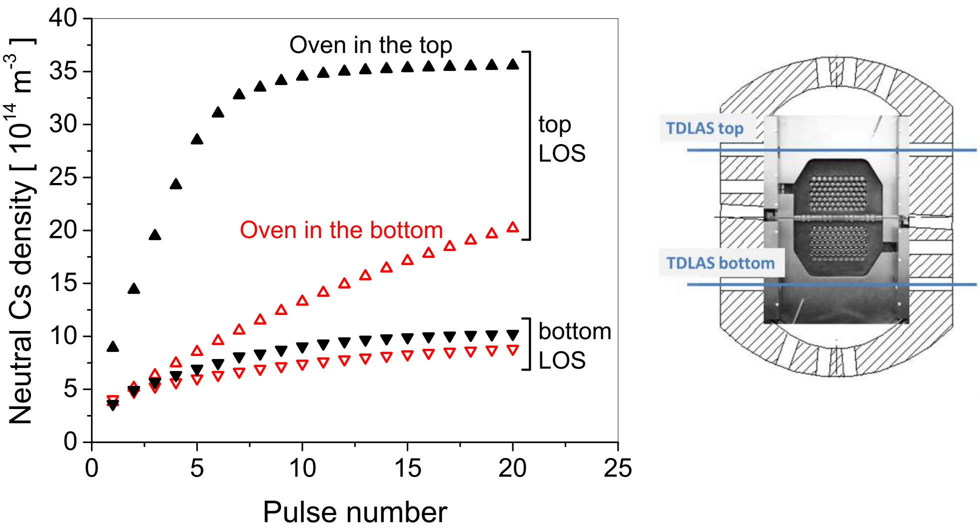

Figure 4.15: Simulated neutral Cs density in the top and bottom line of sight for two Cs evaporation configurations, i.e. by considering only the oven in the top (black) and only the oven in the bottom (red).

of a plasma drift show that Cs distribution in the source is mostly determined by the location where Cs removal is more effective. The change in the position of the oven and so of the Cs reservoirs on the inner surfaces can then either slow down the conditioning process, if Cs is deposited far from the plasma, or accelerate the conditioning in the opposite case. As a general rule, it is therefore advisable to evaporate Cs towards places where it can be efficiently removed and redistributed by the plasma, also in order to reduce the conditioning time.

4.3 Application of CsFlow3D to the racetrack driver concept

The CsFlow3D code was applied in order to optimize the position of the Cs oven for a new configuration of the BATMAN test facility, in which the cylindrical driver is replaced by a race-track shape driver [68]. Figure 4.16 (a) shows a vertical cut of the reacetrack driver mounted at the BATMAN test facility in comparison with the cylindrical driver (figure 4.16 (b)). This driver shape has been already in use for positive ion sources, such as the ones at the ASDEX upgrade experiment [69]. The reason for testing this driver geometry is to verify if in larger modular sources the substitution of two cylindrical drivers with one single race-track driver could enhance the RF efficiency and the reliability of the source.

It can be seen in figure 4.16 (a) that different ports for the Cs oven are available for the racetrack driver in comparison with the cylindrical driver case. The available ports are in the back-plate of the driver (indicated with the letters A, B and C in figure 4.16 (a)) and they will lead to Cs evaporation inside the driver. The other available port is located in the diagnostic flange on the side of the expansion chamber, close to the plasma grid (indicated by letter S).

As mentioned in section 3.3, two constraints have to be considered for the positioning and the orientation of the Cs oven in negative ion sources:

- The amount of Cs in the driver: experiments have shown that an increase of the amount of Cs in the drivers correlate with a decrease in the H_α emission in the driver [32], i.e. a change in the plasma parameter and therefore in the neutral hydrogen flux onto the PG. In the same time, also a reduction of the extracted negative ion current density occurs, in relation to this change in the fluxes: an excessive amount of Cs in the driver should therefore be avoided.
- The amount of Cs which is lost throughout the plasma grid apertures, which can be harmful for the high voltage holding of the extraction system [45].

In order to determine what is the best position for the Cs oven nozzle, when taking into account the available ports and the two constraints, the `CsFlow3D` was applied to calculate two relevant quantities for this optimisation: the total amount of Cs deposited on the driver surfaces during a vacuum phase (which can be released during the plasma phase inside the driver), normalised by the driver volume, and the Cs loss flux throughout the plasma grid apertures, averaged on the extraction area. In particular, the simulation of a vacuum phase of 200 s was performed considering the different available ports and orientations of the nozzle (all the cases are listed in table 4.1).

Case	Position	Nozzle angle
A	Backplate	$\alpha = 0, 10, 20, 30, 40°$
B_0,B_{45}	Backplate	$\alpha = 0, 45°$
C	Backplate	$\alpha = 0, 10, 20, 30, 40°$
S	Diagnostic flange	$\beta = -10, 0, 10, 20, 30°$

Table 4.1: Simulated nozzle configurations for the BATMAN racetrack driver as indicated in figure 4.16.

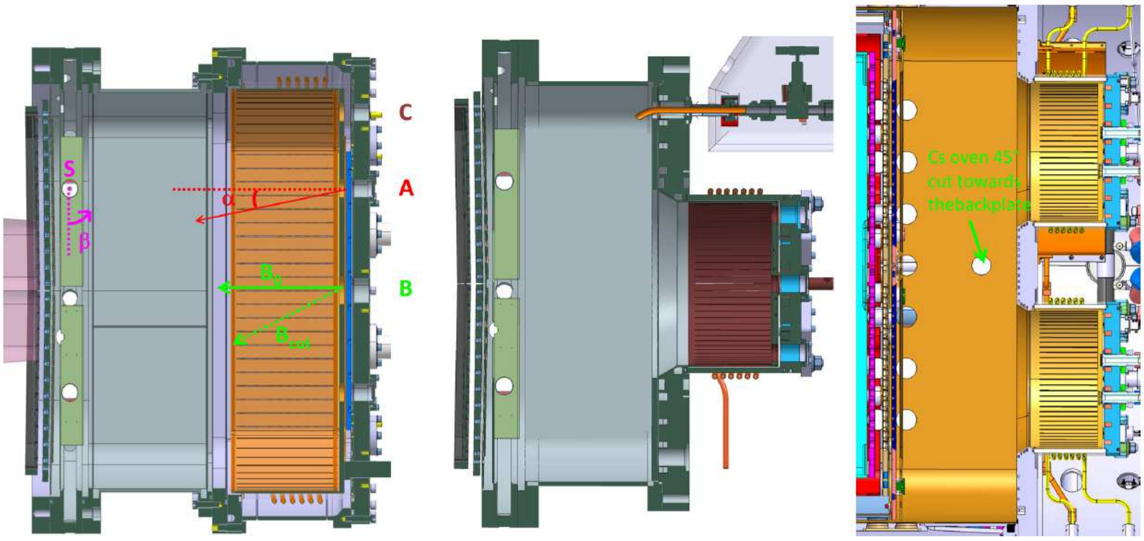

(a) (b) (c)

Figure 4.16: (a) source at the BATMAN test facility with racetrack driver. The different available ports for the Cs oven nozzle are indicated (A, B, C in the back-plate and S in the diagnostic flange); (b) Prototype source with cylindrical driver, oven nozzle on the back-plate, evaporation towards the grid; (c) source at ELISE, oven nozzles in the side wall, evaporation towards the back-plate.

Two reference cases were considered in order to compare the results obtained with the racetrack driver geometry. A 200 s vacuum phase was simulated for the case of the cylindrical prototype source at the BATMAN test facility with the oven in the standard position, i.e. on top of the back-plate (figure 4.16 (b)): this case will be considered as the reference for the Cs loss flux, since the evaporation is directed towards the grid. To have a reference for the Cs deposited in the driver, the same simulation was performed for the source at ELISE (figure 4.16 (c)): in this source two Cs ovens are present on the side wall evaporate towards the back-plate. The overall Cs evaporation rate inside the source in all the cases was set to 10 mg/h.

The plot (a) of fig. 4.17 shows the deposited Cs per unit volume and the plot (b) shows the Cs loss flux averaged on the extraction area for the different Cs nozzle configurations as function of the nozzle bending angle. The amount of Cs which is lost onto the extraction system is much higher in the case of the Cs oven located close the plasma grid (case S) w.r.t. the oven positioned on the back-plate of the racetrack driver (cases A, B and C). Since these fluxes are averaged over the extraction area, the local loss flux towards the extraction system can be also significantly higher than the prototype source reference case: the configuration S is therefore considered not suitable for the positioning of the Cs oven. Regarding the Cs deposited onto the

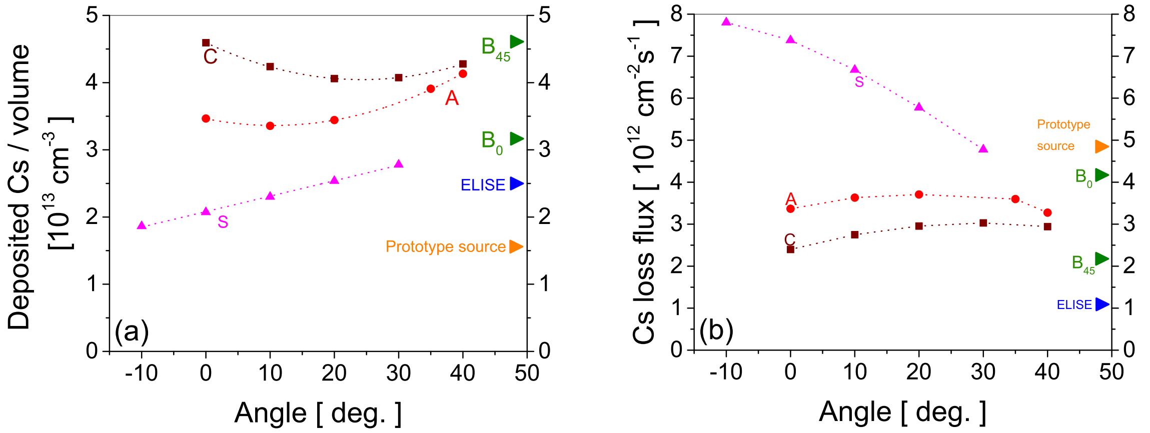

Figure 4.17: (a) Total deposited Cs per unit volume on the inner surface of the driver during a vacuum phase time of 200 s as a function of the nozzle direction; (b) Flux of Cs lost throughout the PG aperture averaged on the extraction area as a function of the nozzle direction. Oven configuration summarised in table 4.1

racetrack driver inner surfaces, all the configurations using the ports on the back-plate of the racetrack driver show higher accumulated Cs per unit volume w.r.t. the ELISE reference. The best cases are the configuration A at 10° and B_0 (i.e. horizontal nozzle at the central ports of the driver back-plate), for which the Cs in the driver is between 25% and 30% more than that for the ELISE reference case.

The best compromise is represented by the configuration B_0, i.e. the horizontal nozzle positioned in the central port of the racetrack driver backplate. In this configuration the Cs inside the driver will be slightly higher than the ELISE reference, but the Cs loss flux can be maintained below the prototype source reference case, with the additional advantage of avoiding an asymmetric position of the Cs oven. This will ensure a more homogeneous caesiation of the plasma grid during a vacuum phase as well as a formation of vertically symmetric Cs reservoirs. During the plasma phase the only possible source of inhomogeneity will then be due to the plasma redistribution.

This oven nozzle configuration has been implemented on the racetrack driver at the BATMAN test facility and it was successfully tested experimentally. No increase of the breakdowns in the extraction system was observed as well as no problem regarding the plasma ignition in the driver.

Figure 4.18 (a) shows the value of plasma density measured by the two Langmuir probes in the top and in the bottom: despite the larger area of the racetrack driver, the plasma distribution is strongly affected by the magnetic filter field and show a pronounced vertical asymmetry, similar as what has been already observed with the

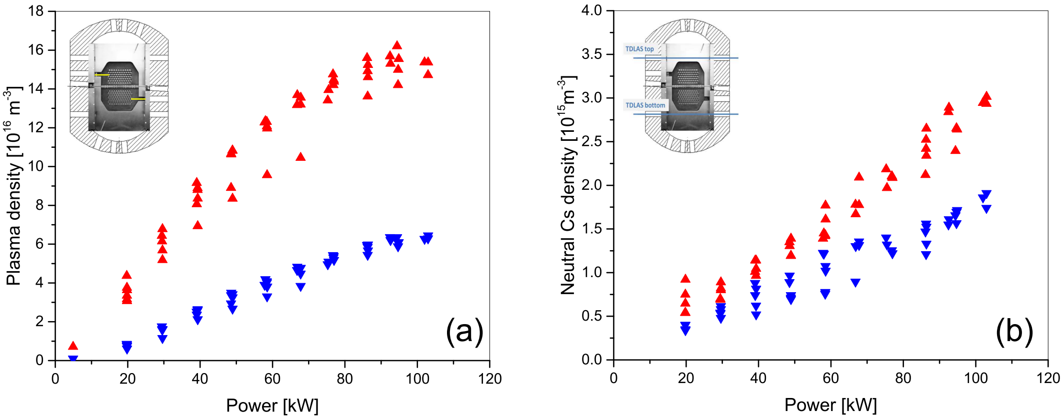

Figure 4.18: Measured plasma density (a) and neutral Cs density (b) with the racetrack driver configuration as a function of RF power.

cylindrical driver [67].

Figure 4.18 (b) shows the neutral Cs density measured by the TDLAS for the top and bottom lines of sight at different RF power. The detected neutral Cs density increases with increasing power and a vertical asymmetry is observed: the observation of an asymmetry in the neutral Cs density was associated with the observation of an asymmetry of the plasma density, reinforcing the statement that the most relevant factor driving Cs dynamics is the distribution of plasma in the source.

The racetrack driver with this Cs nozzle configuration has shown similar performances to the cylindrical source for comparable RF power [67].

5 Simulation results for the ELISE test facility

The purpose of the research at the ELISE test facility is to investigate the feasibility of the ITER-NBI targets in a large source for long pulses up to one hour. The simulation domain of CsFlow3D was extended in order to model Cs redistribution also for ELISE; there are in fact several reasons for which the behaviour and the dynamics can be different in comparison to the prototype source:

- **Surface to volume ratio.** The most important contribution for the caesiation of the PG during the plasma phase is the Cs released from the wall, which is a surface process: the amount of Cs that can be released in plasma is therefore proportional to the surface S. The released Cs is distributed through the entire source volume by collisions, so an inverse proportionality to the volume V of the Cs density and fluxes can be expected. Consequently, for the same evaporation rate, a higher S/V ratio would lead to higher Cs fluxes. The volume of the source at ELISE is ~ 4 times larger than the prototype source, and the source has a different surface to volume ratio S/V: for ELISE it is $\sim 4\,\mathrm{m}^{-1}$, while for the prototype source at BATMAN it is $\sim 11\,\mathrm{m}^{-1}$.

- **Cs sputtering due to back-streaming ions.** As mentioned in section 3.1.3, Cs can be removed from the backplate of the source due to sputtering induced by the back-streaming ions. This contribution was negligible in the prototype source due to the geometry and position of the PG apertures, while in ELISE the rate is expected to be higher.

- **CW operation**. ELISE is designed to operate in CW plasma operation and pulsed extraction due to power supply limitation (while for the ITER-NBI sources also CW extraction is foreseen). The time evolution of Cs distribution in the source as well as the depletion of the Cs reservoirs on the source walls for such a large source can become an issue for the operation at the maximum performances.

- **Cs evaporation configuration.** At the ELISE test facility two Cs ovens are used and they are located on the side wall of the experiment: this is a completely different configuration w.r.t. the BATMAN test facility, with a single oven on the back-plate of the source.

In a first stage CsFlow3D was used to perform simulations of short pulses: the results will be compared with those obtained for the prototype source at BATMAN, in order to understand if the basic principles of Cs dynamics that have been learnt for BATMAN can be extended also for ELISE and in general for RF negative ion sources of similar geometry. The results obtained for ELISE will be compared with the experimental measurements performed with TDLAS in short pulses.

The open issues which are addressed by the application of the code to the ELISE test facility are:

- the investigation and quantification of the Cs release by back-streaming ion sputtering;
- the possibility of affecting the magnitude and stability of the Cs flux onto the PG by adjusting the duty cycle;
- the study of the temporal evolution of Cs behaviour during long pulse, by comparing the case of pulsed extraction achievable by ELISE to the continuous extraction foreseen for the ITER-NBI sources and for which no experimental data are available;
- to identify strategies in order to avoid the reduction of the Cs flux onto the PG during long pulses, e.g. by relying on the additional Cs released by back-streaming ion sputtering or by using alternative Cs evaporation configurations.

5.1 Short pulse operation

The simulation results for the prototype source have shown that some cycles of vacuum phase (200 s) followed by plasma phase (8 s) are needed in order to achieve a good conditioning of the source and a stability of the Cs flux and Cs density. In particular, when starting from a clean source (no Cs deposited on the wall), the minimum number of cycles needed to reach stability was ~ 20. This conditioning process

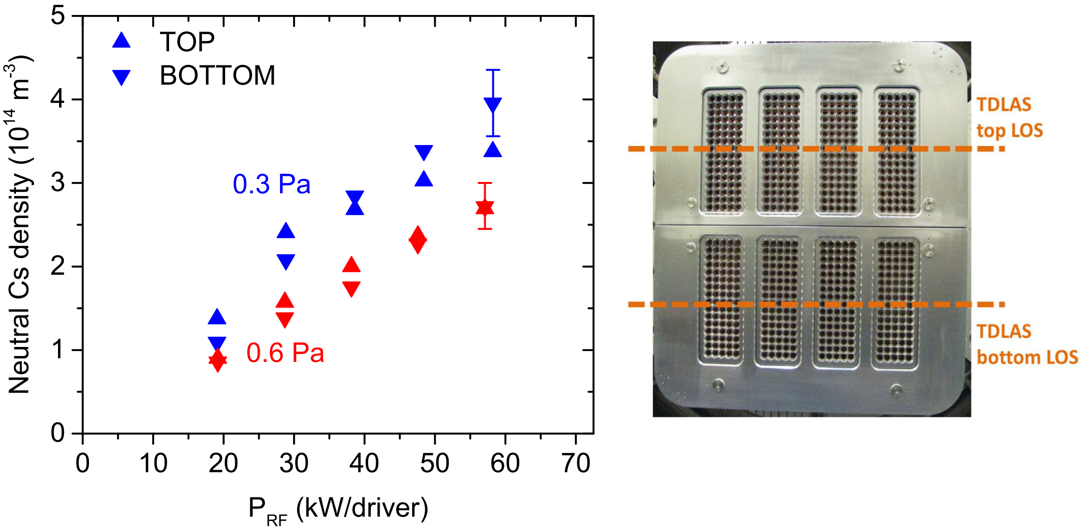

Figure 5.1: Neutral Cs density in the top and bottom lines of sight at the ELISE test facility as a function of the RF power. The data are presented for two different filling pressures, 0.3 Pa and 0.6 Pa.

is needed in any source which relies on caesiation and therefore also for the source at ELISE, as it is seen in the experiments and it can be proven by performing the same simulations carried on for the prototype source.

The standard *short pulse* duration time at the ELISE source has been defined as 20 s, as normally set in the experiment and a vacuum phase of 200 s has been chosen. No plasma drift is taken into account in the model (i.e. $\Delta y_{\text{max}} = 0\,\text{cm}$) and vertically symmetric plasma profiles are used (see appendix A), since the effect of the magnetic filter field on the vertical distribution of the plasma is lower w.r.t. the prototype source [70]. For this reason, no vertical asymmetry of Cs distribution is expected for ELISE. This is confirmed by the experiments: figure 5.1 shows the top and bottom neutral Cs density measured by TDLAS as a function of the RF power per driver at the ELISE test facility. The data were collected for two filling pressures, namely 0.3 and 0.6 Pa. The Cs density shows the same linear dependence on the power that was already observed in the prototype source, but no significant vertical asymmetry is present.

The simulations of 20 consecutive cycles of vacuum phase and plasma phase were performed. The Cs oven reservoir temperature at ELISE is normally set to a lower value w.r.t. the prototype source: a rough scaling leads to a value of ∼ 5 mg/h/oven. Since there are two ovens on the side of the expansion chamber at ELISE (see section 2.3.2), the total evaporation rate set in the simulations was 10 mg/h. The relevant pa-

	BATMAN	ELISE
t_{vacuum}	200 s	200 s
t_{plasma}	8 s	20 s
$t_{\text{extraction}}$	4 s	10 s
N_{cycles}	20	20
Δy_{max}	10 cm	0 cm
Oven evap. rate	10 mg/h	5 mg/h

Table 5.1: Comparison of the simulation parameters used by CsFlow3D for the two test facilities BATMAN and ELISE for the investigation shown in figure 5.2.

rameters for this simulation, in comparison with those used for the prototype source, are reported in table 5.1.

Figure 5.2 shows the line averaged neutral Cs density as a function of the progressive pulse number: in red, the values for the top line of sight of TDLAS at ELISE and in black for the top and bottom lines of sight at the prototype source, as already shown in fig. 4.12. The neutral Cs density calculated by the code for ELISE is the same in the top and in the bottom, due to the vertical symmetry of the oven position and of the plasma parameters, therefore only the results for the top line of sight are shown. For the prototype source a vertical plasma displacement with a $\Delta y_{max} = 10$ cm was considered.

The simulations for the ELISE case shows an increase of the Cs density pulse after pulse and a constant value is reached close to the 20th pulse. Compared to the

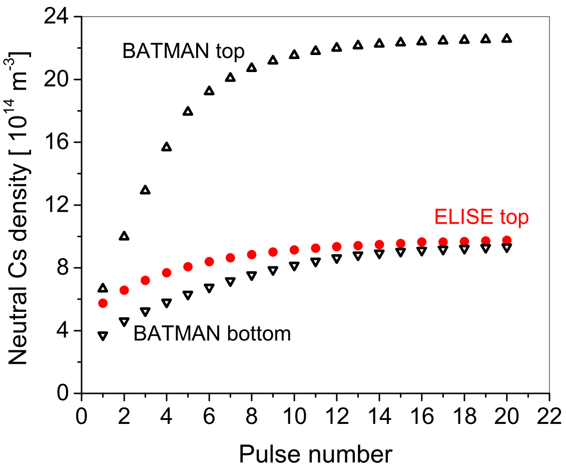

Figure 5.2: Evolution of simulated Cs density pulse by pulse in the top line sight for ELISE (circle) in comparison with the simulation performed for the prototype source with plasma drift (triangle).

top line of sight of BATMAN, a lower density is observed in ELISE, because of the lower S/V ratio and the higher depletion due to the longer plasma phase (20 s). A repetition of cycles of plasma phase and vacuum phase is beneficial also in the case of the larger source at ELISE in order to increase the amount of Cs available for redistribution.

To investigate if the contribution of the direct evaporation from the oven during the plasma is negligible also for ELISE the standard 20 s pulse after the conditioning procedure was simulated in two different conditions: in one case without Cs evaporation during the plasma phase, in the other case with Cs evaporation active also during plasma.

The time traces of the line averaged neutral Cs density for the two cases are shown in figure 5.3. In both cases, an increased Cs density during plasma w.r.t. the vacuum phase level is observed, rising from $\sim 2 \cdot 10^{14}\,\mathrm{m}^{-3}$ to $\sim 10^{15}\,\mathrm{m}^{-3}$. By comparing the two time traces, it can be derived that the contribution of the oven is negligible: the neutral Cs density measured with the oven evaporating during the plasma phase gives a value only $\sim 5\%$ higher than the one calculated without the Cs oven evaporation. Most of the Cs in plasma is released from the surfaces.

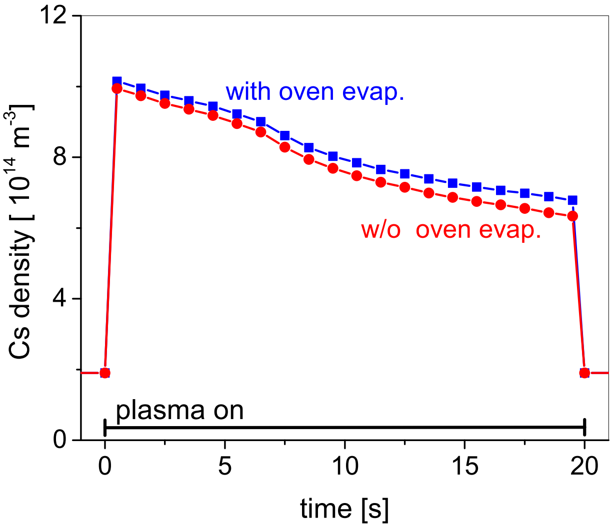

Figure 5.3: Simulated neutral Cs density in the top line of sight at ELISE for the 20th pulse (vacuum phase between pulses 200 s). The two cases with and without evaporation during the plasma pulse are shown.

5.1.1 Relevance of back-streaming ion sputtering to Cs release

The relevance of the back-streaming ions in releasing Cs from the source back-plate via sputtering can be demonstrated by computing both the cases with and without the contributions of back-streaming ions and comparing the experimental cases with and without extraction.

The plots in figure 5.4 (a) shows the experimental time traces for two pulses, one with extraction and the other without extraction. The time traces of the discharge parameters, i.e. power and pressure, as well as the currents and the voltage for the case with extraction are also shown. Figure 5.4 (b) shows the results of the simulations (20 s pulse without extraction in one case and with 10 s extraction in the other case). The extraction and acceleration voltage was set to 7 kV and 28 kV respectively, in order to compare simulation results with experimental data. Before the simulation of these two pulses, the standard 20 conditioning cycles was simulated.

The experimental time traces should be compared with the code results only for ($t \gtrsim 5\,s$), when the power and pressure in the experiment reaches the nominal set values.

The agreement between simulations and experimental data appears to be very good: when considering the case without extraction, the absolute value of density is in agreement as well as the decrease in time of the Cs density. In correspondence with the extraction phase, an increased value of Cs density is observed both in the TDLAS data and the simulations. This experimental increase is of the same order of magnitude of the simulated one. The density after the extraction phase for $t > 15\,\mathrm{s}$ is slightly lower than the case without extraction, again both in the experiments and in the simulations: this effect can be explained as a reduction of the Cs reservoirs on the back-plate due to the back-streaming ion sputtering, thus implying that a lower amount of Cs is available on the back-plate for the other removal processes once the extraction is stopped.

The comparison of the simulated and experimental time traces show that the release of Cs due to back-streaming ions is a plausible explanation for the observed Cs increase at the start of the extraction phase. To prove it experimentally and to exclude other phenomena (such as Cs release from the grid system) which can lead to this additional Cs release, a correlation of this increase on the voltages or on the beam optics need to be identified.

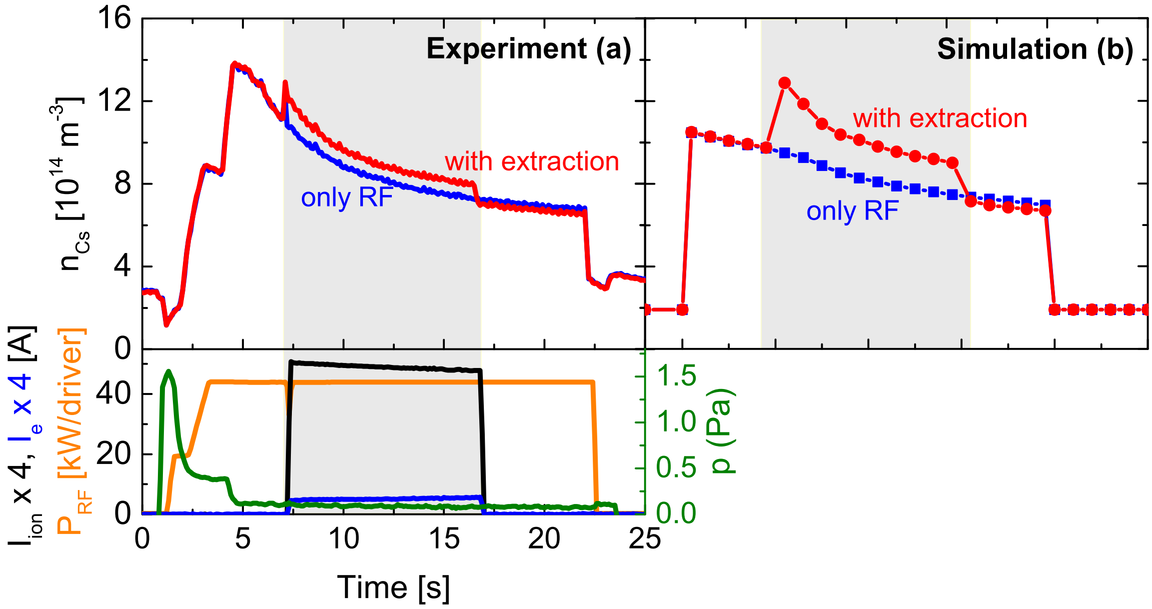

Figure 5.4: Experimental (a) and simulated (b) time traces of neutral Cs density for two pulse at ELISE test facility, one with extraction and one only with the RF plasma. The time traces of the experimental discharge parameters such as pressure and power are also reported, together with the negative ion and the co-extracted electron currents for the case with extraction. The experiment was conducted in deuterium.

To verify if there is an experimental dependence on the acceleration voltage, a scan of this parameter was performed. The absolute value of Cs density increase once the extraction phase starts is defined as:

$$\Delta n_{\mathrm{Cs}} = n_{\mathrm{Cs,HV}} - n_{\mathrm{Cs,RF}} \tag{5.1}$$

where $\mathrm{n_{Cs,HV}}$ is the Cs density measured immediately after the beginning of the extraction phase, while $\mathrm{n_{Cs,RF}}$ the density immediately before.

The value of Δn_{Cs} depends on the extraction and acceleration voltages and it is also proportional to the extracted negative ion current, since the amount of the generated back-streaming ions is proportional to the number of negative ions. For this reason the value of Δn_{Cs} is normalised by the current I_{ion} and the normalised value is defined as the parameter $\kappa = \Delta n_{\mathrm{Cs}}/I_{\mathrm{ion}}$.

Together with the experimental measurement of κ, also a simple 1D model of the generation of back-streaming ion and consequent Cs release is used. The reactions which can produce H^+ and H_2^+ inside the extraction and acceleration system were presented in 3.1.3 and the cross section are taken from [71]. This model assumes

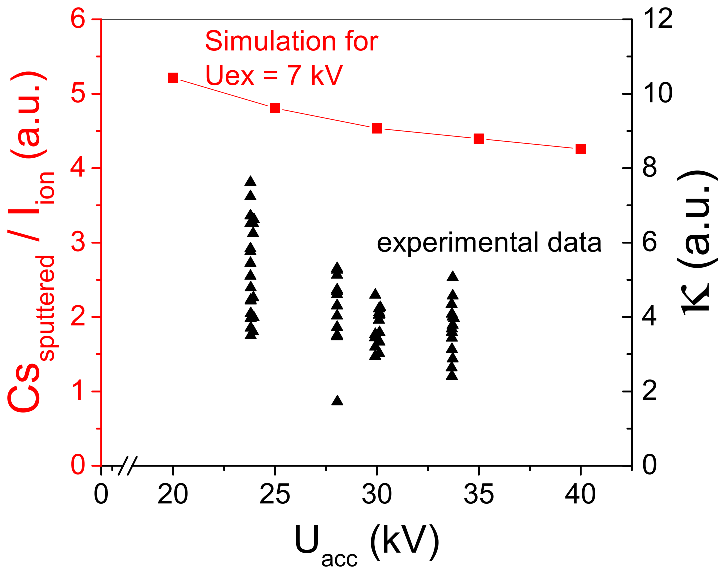

Figure 5.5: Amount of sputtered Cs normalised to the ion current. Simulations (red) and the measured value of $\kappa = \Delta n_{\mathrm{Cs}}/I_{\mathrm{ion}}$ are shown.

that the generated positive ions are not affected by the optics of the grid system and they are straightly accelerated back through the grid aperture, thus reaching the projection of the apertures onto the back-plate of the source. It follows that the amount of sputtered Cs normalised by the ion current can be calculated as:

$$\propto \int f_{\mathrm{H}^+}(E)\,Y(E)\,dE + \int f_{\mathrm{H}_2^+}(E)\,Y(E)\,dE \tag{5.2}$$

$Y(E)$ is the sputtering yield of Cs by H^+ (see section 3.1.3), while f_{H^+} and $f_{\mathrm{H}_2^+}$ represents energy spectrum of H^+ and H_2^+ respectively, i.e. :

$$\int f_{\mathrm{H}^+} dE = N_{\mathrm{H}^+} \tag{5.3}$$

$$\int f_{\mathrm{H}_2^+} dE = N_{\mathrm{H}_2^+} \tag{5.4}$$

Figure 5.5 shows in black the plot with the experimental values of κ as a function of the acceleration voltage measured experimentally at ELISE and in red the estimated value of the normalized amount of sputtered Cs from the simple model presented above by using equation 5.2. Although the dispersion of the experimental data is relatively high, a weak trend can be identified: κ decreases with increasing

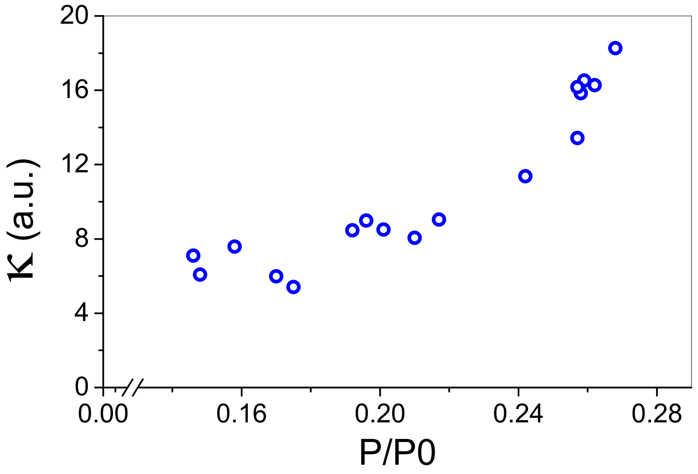

Figure 5.6: Experimental values of $\kappa = \Delta n_{\mathrm{Cs}}/I_{\mathrm{ion}}$ as function of the normalized perveance defined in equation 5.5.

acceleration voltage U_{acc}. The results from the model shows the same weak trend of κ on $\mathrm{U}_{\mathrm{acc}}$.

A more evident proof that the increase of Cs observed during the extraction phase comes from the back-streaming ion sputtering is the correlation observed between the parameter κ and the normalised perveance as shown in figure 5.6. The normalised perveance is an index which characterises the optics of an ion beam w.r.t. to the Child-Langmuir law for the plane diode case [72] and it is defined as:

$$P/P_0 = C \cdot \frac{I_{ion}}{U^{3/2}} \tag{5.5}$$

where C is a constant which depends on the geometry of the grid system.

In ELISE the best optic for the negative ion beam, i.e. the lowest beam divergence, is achieved for normalized perveance equal to 0.25 [73]. The plot shows a high value of κ for a normalised perveance in the range 0.24 - 0.25, while it decreases with decreasing perveance: it seems therefore that a good beam optic results in a larger amount of sputtered Cs. A similar correlation was observed in the negative ion source at NIFS[1] [74], thus validating the theory of back-streaming ions as cause for the additional Cs observed when switching on the extraction.

---

[1] National Institute for Fusion Sciences, Toki, Japan

5.1.2 Influence of duty cycle on the Cs amount and stability

The duty cycle, i.e. the relation between the vacuum phase time and the length of the plasma phase, is investigated with CsFlow3D by keeping constant the 20 s plasma phase time and using different vacuum phase time, namely 200, 400, 600 and 800 s. In each case the standard 20 conditioning cycles are performed.

The comparisons between the time traces of the 20th pulse after the conditioning phase for the case of 200 s, 400 s and 600 s vacuum time are reported in figure 5.7. For each vacuum phase two different pulses are simulated, one with extraction one without. The Cs density increases by increasing the vacuum phase time: from $10^{15}\,\mathrm{m}^{-3}$ for 200 s to $2{\cdot}10^{15}\,\mathrm{m}^{-3}$ for 600 s. In all the cases the effect of the back-streaming ions can be observed: in particular for the 200 s case the reduction of the Cs density during the simulations. This is correlated to a faster depletion of the Cs reservoirs in the back-plate as it will be shown in section 5.2.

The different vacuum phase time does not only affect the absolute value of the neutral Cs density during the pulse, but also its stability. The instability index can be defined as $\Delta n_{\mathrm{Cs}}/n_{Cs}$, where Δn_{Cs} is the difference between the Cs density at the beginning and at the end of the plasma phase and n_{Cs} is the time averaged density. Figure 5.8 shows the instability index as function of the consecutive pulse number for different values of the vacuum phase time. In all cases, the instability of the simulated Cs density decreases by repeating several time the cycle of vacuum and plasma phases, until a saturation level is reached. It can be seen that a vacuum phase of 400 s or more improves the stability of Cs density for short pulses w.r.t. the case of 200 s.

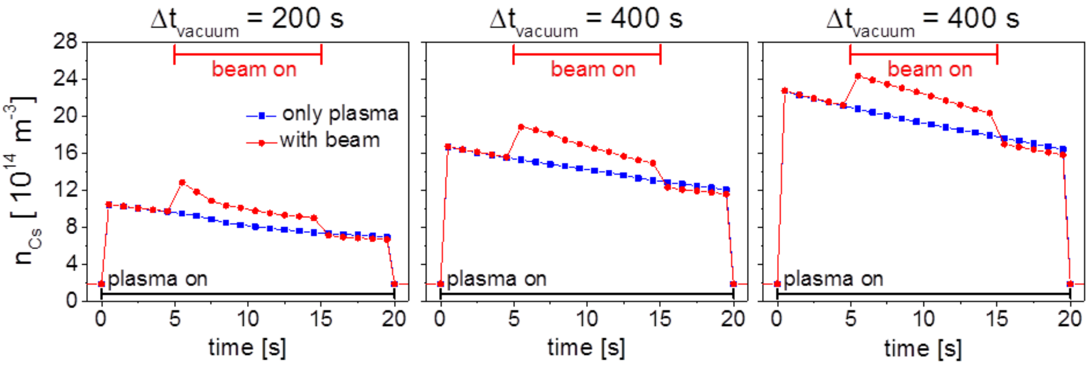

Figure 5.7: Simulated neutral Cs density during the 20th shot of the conditioning phase. Three different vacuum phase durations of 200 s, 400 s and 600 s are considered. Time traces are calculated both for the case with and without HV beam.

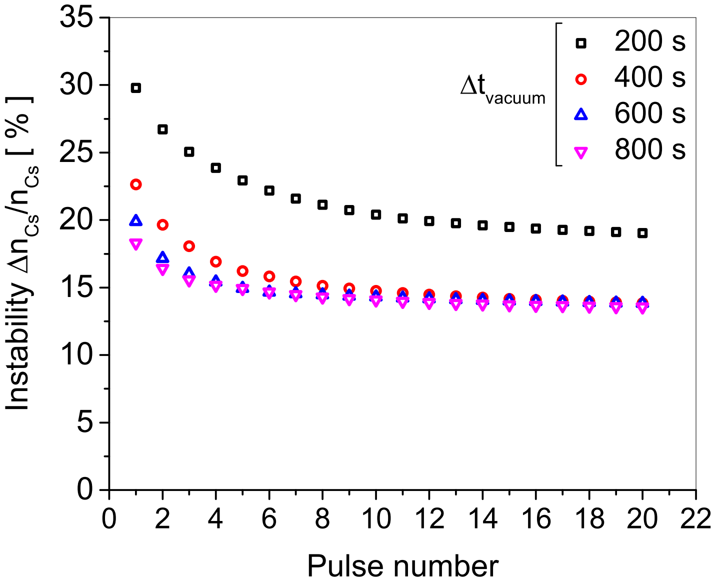

Figure 5.8: Evolution of the stability of neutral Cs density in front of the plasma grid for different vacuum phase time between pulses.

5.1.3 Lessons learnt for short pulses

The lessons learnt from the investigation of the Cs dynamics in short pulses at the ELISE test facilities are therefore the following:

- the results obtained for the prototype source at BATMAN are valid also for ELISE, i.e. the need of a conditioning procedure in order to reach an equilibrium of the amount of Cs released during the plasma phase and the negligible contribution of the direct oven evaporation during the plasma;
- the code reproduces the measured neutral Cs density, both the absolute values and the trend of the time traces and can be used to make predictions;
- the sputtering due to back-streaming ions during the extraction phase is a significative additional source terms of Cs;
- the duty cycle has a clear effect on the Cs density during plasma and on its stability: a vacuum phase longer than 400 s should be chosen for an evaporation rate of 5 mg/h/oven.

5.2 Cs flux evolution during long pulse operation

The most critical factor limiting the source performance during long pulses is the increase of the co-extracted electrons in time. Figure 5.9 shows the experimental time traces of the extracted negative ion current density and the co-extracted electron density during a long pulse: the plasma is on during all the time, but as mentioned in section 2.3.2 the extraction phase is limited to 10 s every 150 s. The plasma phase is 1175 s with seven beam blips, i.e. extraction phases.

The ion current appears almost stable through all the pulse, while the co-extracted electron current density strongly increases already between the first and the second beam blip. This is most probably connected to a degradation (i.e. an increase) of the work function of the PG. Inside a single beam blip the co-extracted electrons have instead the opposite behaviour, i.e. the co-extracted electron current density decreases during the 10 s of extraction, as highlighted in the enlarged plot of the last beam blip.

The simulations performed with CsFlow3D cannot provide direct information about the evolution of the co-extracted electrons or the PG work function. However, the code can predict the temporal evolution during long pulses of the Cs flux onto the PG, which is related to the PG work function: these predictions can be

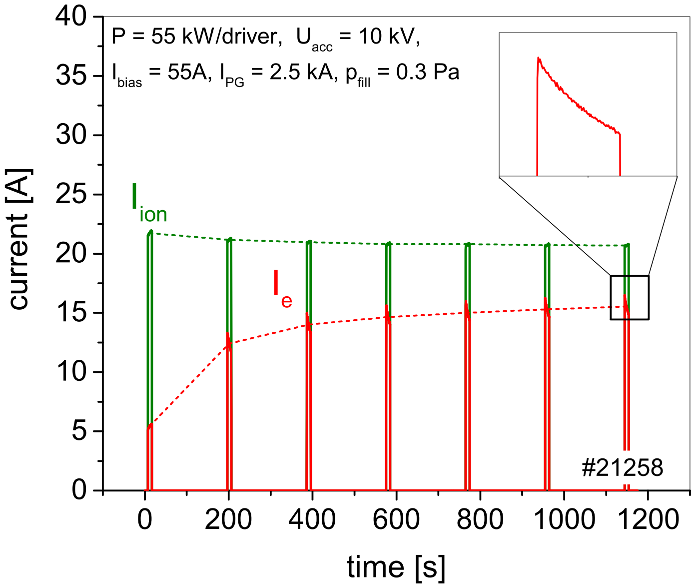

Figure 5.9: Time traces of the extracted negative ion and co-extracted electron current density for a long pulse (1175 s) at the ELISE test facility.

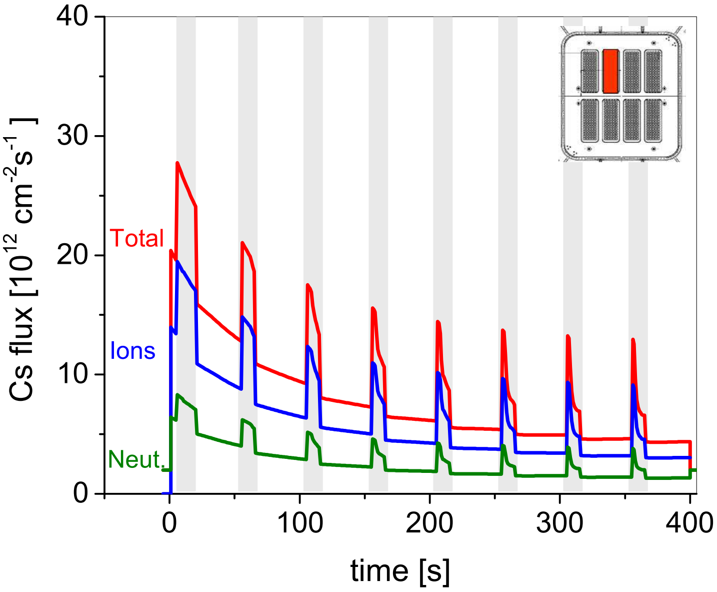

Figure 5.10: Simulated time traces of the Cs flux (total, ions and neutrals) averaged on the area of the beamlet group indicated on the scheme. Extraction phases of 10 s are repeated each 50 s and indicated by the grey shaded area.

used to understand the behaviour of the source in long pulses. With this purpose, a 400 s pulse was simulated with extraction phases of 10 s every 50 s: the duty cycle was changed w.r.t. the experiments in order to model more beam blips in a shorter time and therefore have more statistic while saving computational time.

Figure 5.10 shows the time traces of the simulated Cs flux averaged on the area of one beamlet group (which is represented in the plot). The two components of the flux, i.e. of neutral Cs and of the Cs ions, are plotted together with the total flux. The grey shaded areas indicate the 10 s beam blips. Most of the Cs reaching the PG is ionised: in the specific case the ratio between the ion and the total Cs flux is up to ∼ 70%. When considering the overall trend of Cs density, a strong decrease with time can be observed: this indicates a depletion of the Cs reservoirs on the source walls due to the plasma erosion. This depletion is evident by comparing the Cs coverage on the side of the source at the beginning of the pulse and after 400 s, as shown in figure 5.11: a strong reduction of the deposited Cs close to the driver exit is evident.

During each beam blip, the flux of Cs increases w.r.t. the plasma only phases due to the back-streaming ions sputtering. This increased Cs flux can be the explanation of the dynamics of the reduction of the co-extracted electron current density during

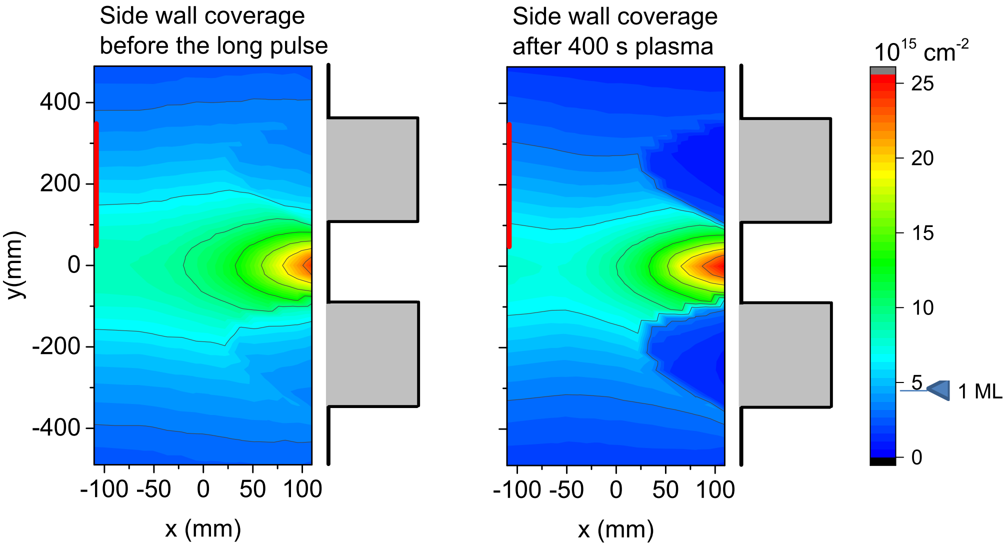

Figure 5.11: Cs coverage on the side of the source at the beginning of the simulated long pulse (t=0 s) and after the pulse (t=400 s)

the beam blip. The Cs flux decreases faster during the beam blip, due to the additional depletion of the Cs accumulated on the back-plate. From the fourth beam blip on ($t > 150$ s), the Cs flux at the beginning of each beam blip is higher than the flux at the end of the previous beam blip. This is correlated with the evolution of the Cs coverage on the back-plate. Figure 5.12 shows the Cs coverage averaged on the area of one beamlet group projection onto the back-plate (as indicated by the red area in the plot) between $t = 200$ s and 400 s. The grey shaded areas represent the beam blip, i.e. the time in which back-streaming ions sputter Cs from the back-plate. A reduction of the Cs coverage is observed in this phase. Instead, during the plasma only phase, the Cs coverage increases, indicating a replenishing of the Cs reservoirs, which can provide again Cs for the following beam blip.

Differently to the ELISE case, the ITER-NBI source is foreseen to have a continuous extraction phase. The code was used to make prediction also for a long pulse with continuous extraction. Another simulated scenario was the assumption of an unlimited Cs coverage on the back-plate, i.e. avoiding the depletion and thus having the maximum achievable amount of Cs released by back-streaming ions.

The results for these two cases in comparisons with the pulsed extraction are plotted in figure 5.13. The trend of the black curve shows that the continuous extraction does not help significatively stabilise the Cs flux, even though the Cs release due to back-streaming ion sputtering is active all the time. A strong reduction of the flux

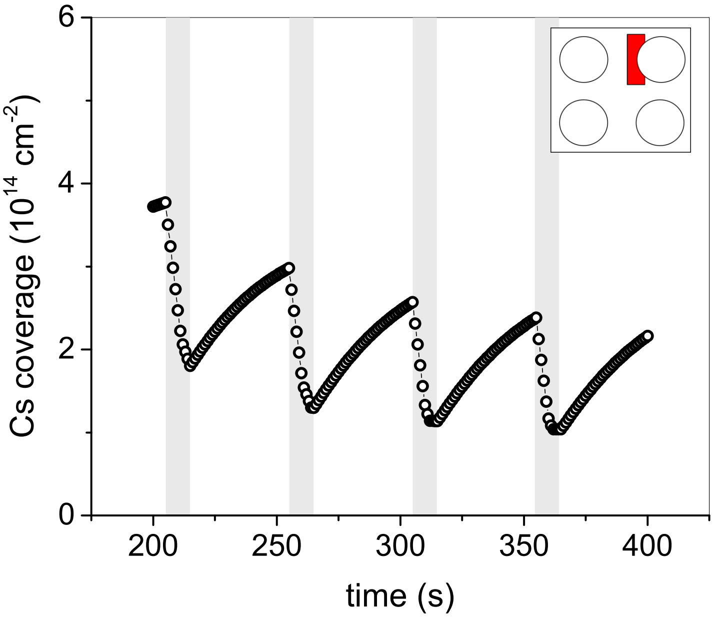

Figure 5.12: Evolution between $t = 200\,\mathrm{s}$ and $400\,\mathrm{s}$ of the Cs coverage averaged on the beamlet group projection onto the back-plate as indicate by the red area in the scheme. The grey shaded areas indicated the extraction phases.

is observed and at the end of the pulse the Cs flux saturates at the same level as for the pulsed extraction case.

By considering instead the case with unlimited Cs reservoir on the entire surface of the back-plate, a decrease of the flux is visible for the first 200 s: this corresponds to the depletion of the Cs reservoirs on the other surfaces of the source. The stable value of the flux for the unlimited Cs on the back-plate results $\sim 30 \cdot 10^{12}\,\mathrm{cm}^{-2}\mathrm{s}^{-1}$, while in the other cases the saturation value of the flux at the end of the pulse is six times lower, i.e. $\sim 5 \cdot 10^{12}\,\mathrm{cm}^{-2}\mathrm{s}^{-1}$.

From these results it can be concluded that a high amount of Cs on the back-plate can be very beneficial to stabilize the Cs fluxes for long pulses by exploiting the release due to the back-streaming ions. Further investigations are needed in order to better understand the dependence of the back-streaming ion fluxes and energy spectrum on the operational parameters, such as grid voltages, pressure, extracted negative ion current, etc.

An additional parameter in the experiments is represented by the bias voltage between the PG and the source. The purpose is to reduce the amount of co-extracted electrons, by attracting them on the PG. If the PG is biased sufficiently positive w.r.t.

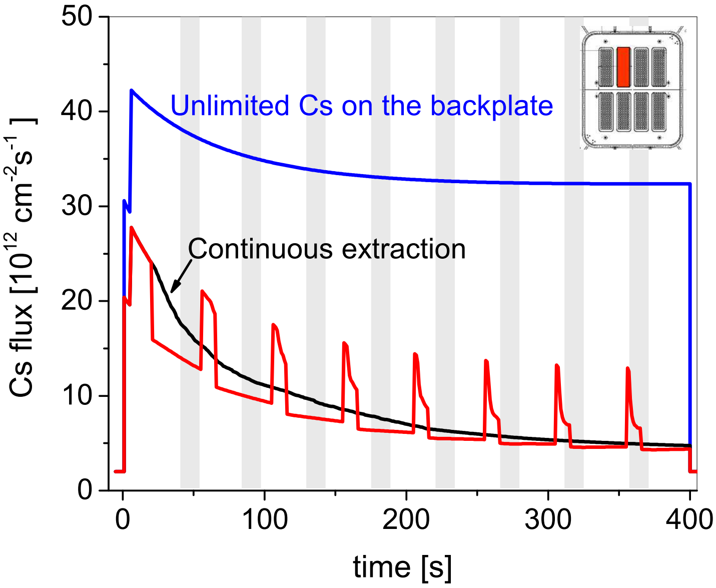

Figure 5.13: Time traces of the total Cs flux averaged on the area of the indicated beamlet group for three different configurations: pulsed extraction (red), continuous extraction (black) and continuous extraction with unlimited Cs on the back-plate (blue). The grey shaded areas indicate the extraction phases in the case of the pulsed extraction.

the source body an electron attracting sheath is generated. In this condition the PG attracts negative charges but repels positive ones: this means that the positive Cs ions, which represent the majority of the Cs flux onto the PG, are partially repelled. This sheath strongly depends on the operational parameters and was not taken into account in the CsFlow3D model. In the worst case all the Cs ions are repelled: the Cs flux on the PG in the experiment would be 30% of the total flux resulting from the simulations, i.e. only the neutral fraction. The relation between this reduction of the effective flux of Cs impinging on the PG due to the bias voltage and the source performances is still an open issue.

5.3 Alternative Cs evaporation method

An alternative Cs evaporation configuration is represented by the possibility of evaporating Cs by means of an array of Cs dispensers located close to the PG. This configuration was already simulated for the case of the prototype source [8], resulting in a lower ionisation degree of the Cs flux onto the PG. This seems therefore a promising solution to overcome the problem of Cs ion repulsion from the PG on the one hand, on the other hand to have a caesiation method which relies on direct evaporation.

Simulation using this concept were performed for ELISE, where sort of *Cs shower* at some centimeters of distance from the PG was considered. This could be in principle achieved using some vertical Cs emitters located on the side of the beamlet groups at a certain distance d. The sketch in figure 5.14 shows a vertical and axial view of this emitter. The triangular section of the emitters allows for the Cs evaporation towards the beamlet group: the aperture angle of the triangle is calculated as a function of the distance d in order to have the normal vector of the emitter surface pointing towards the center of the beamlet group. The evaporation of Cs is supposed to occur all along the vertical emitter with a cosine distribution.

In figure 5.15 the total flux onto the PG by using the presented Cs emitters at a

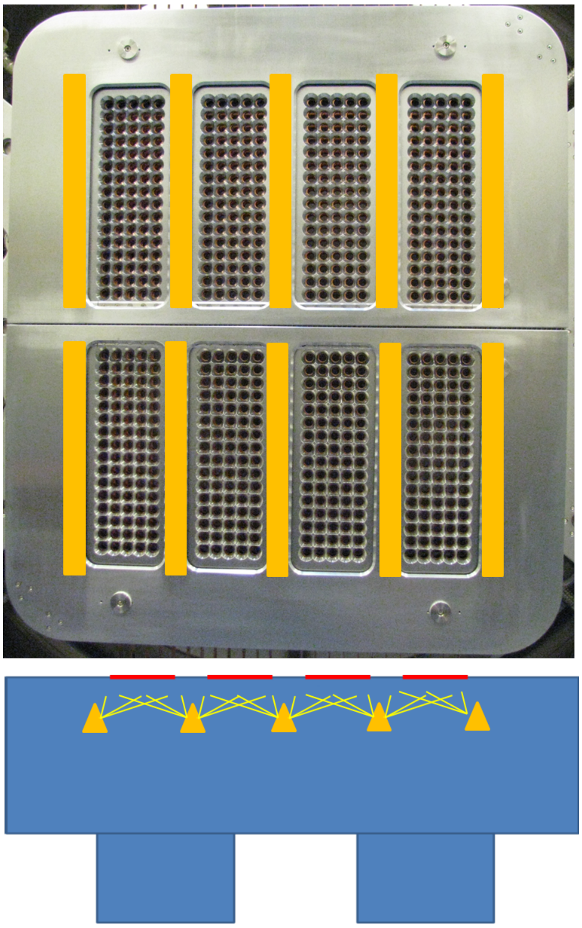

Figure 5.14: Schematic view (top: axial, bottom: vertical) of a possible alternative Cs evaporation configuration for the ELISE test facility. Vertical evaporators with triangular section could be used for a direct evaporation towards the beamlet group.

distance $d = 3\,\mathrm{cm}$ is plotted. It can be seen that quite homogeneous flux onto the PG can be achieved, with an average value on the beamlet group of around $7{\cdot}10^{12}\,\mathrm{cm}^{-2}\mathrm{s}^{-1}$, by considering an overall evaporation rate of 10 mg/h. In this configuration the flux does not change in time independent as long as the evaporation rate is constant: a kind of real-time system to adjust the Cs evaporation rate to the source performances could in principle be developed. This implies a higher reliability and a easier control of the source operation; the reliability is a fundamental requirement for the sources of the NBI systems of industrial demonstration power plant, such as DEMO.

In contrast with the standard case presented in the previous sections, in which most of the Cs reaching the PG from plasma redistribution was ionised (70%), in this case most of the Cs is neutral. Cs is in fact evaporated in a region with low electron temperature, thus decreasing the efficiency of the electron impact ionisation process. The plot in figure 5.16 shows the ratio between the ionic flux and the total flux onto a beamlet group as a function of the distance between the emitting elements and the PG: the ion fraction is strongly reduced from the 70% of the standard evaporation

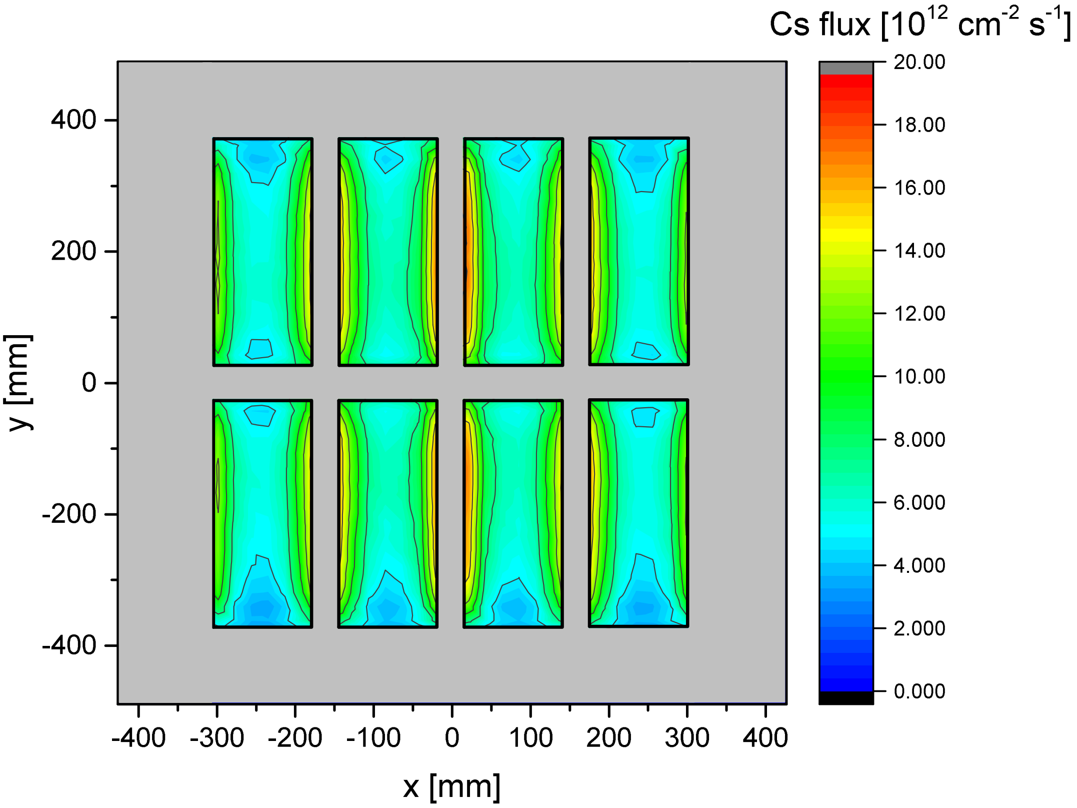

Figure 5.15: Simulated Cs flux onto the plasma grid with the distributed Cs evaporation close to the plasma grid.

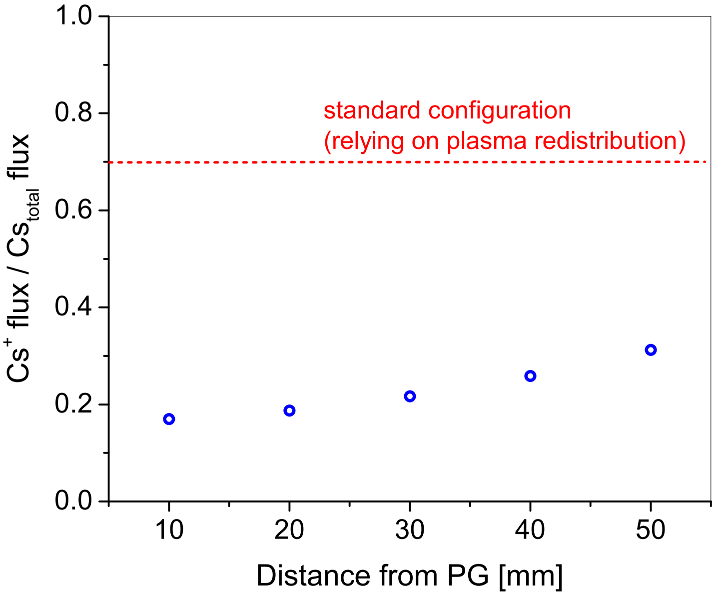

Figure 5.16: Ionization degree in front of the plasma grid for the distributed Cs evaporation as a function of the distance of the evaporating elements from the grid. The dashed line is the value obtained with the standard evaporation method.

configuration to values down to 20%. With this alternative oven evaporation, a constant flux of Cs of $7{\cdot}10^{12}\,\mathrm{cm}^{-2}\mathrm{s}^{-1}$ can be achieved during all the pulse, which is comparable to the neutral Cs flux achieved at the beginning of a long pulse with the standard evaporation configuration, i.e. $\sim 8 \cdot 10^{12}\,\mathrm{cm}^{-2}\mathrm{s}^{-1}$ (plot in picture 5.10). This strategy looks therefore very promising to improve the stability and control of the caesiation of the PG during long pulses and to avoid the Cs repulsion of positive Cs ions due to the bias voltage.

A disadvantage of this solution is the fact that having the evaporation so close to the aperture of the PG, a higher accumulation of Cs inside the extraction and acceleration system can occur, thus increasing the possibility of breakdowns.

These results suggest that this configuration is worth to test experimentally to verify if an improved temporal and spatial control of the caesiation can be achieved, towards a reduction of the Cs consumption. The Cs consumption is in fact an aspect of particular importance to reduce the maintenance requirements, both for the case of the ITER-NBI and for the DEMO-NBI systems.

6 Suggested methods for the optimization of Cs dynamics

The benchmark of the CsFlow3D with the experimental data from the prototype source at BATMAN, as well as the investigation performed for the larger source at the ELISE test facility, allowed to obtain a computational tool that can be used to make predictions about Cs fluxes and coverage in negative ion sources.

The knowledge acquired from the results of the previous investigations is necessary to identify some experimental methods for the optimization of the Cs dynamics in negative ion sources, i.e. to achieve these targets:

- **Improve the temporal instability and spatial distribution of the Cs flux onto the PG**. Due to the correlation between the Cs flux onto the PG and its workfunction [44], the strong Cs depletion observed in the simulations of long pulses at ELISE needs to be avoided, for the stability and the reliability of the source performances;
- **Reduction of Cs consumption**. This aspect is particularly relevant to limit the maintenance in the view of future industrial power plants, such as DEMO.

In this chapter the available knobs which can be tuned to achieve these targets will be identified and discussed, on the base of the results obtained from the CsFlow3D simulations. All the methods towards the improvement of negative ion source caesiation that were identified in the previous sections are summarised in figure 6.1.

6.1 Stabilisation of Cs flux onto the PG

CsFlow3D has revealed that the Cs released during the plasma phase comes from the source walls and the contribution of the direct flux from the oven is negligible, both for the case of BATMAN (figure 4.2) and ELISE (figure 5.3). The evolution of the amount and the distribution of Cs deposited on the source walls is a key parameter

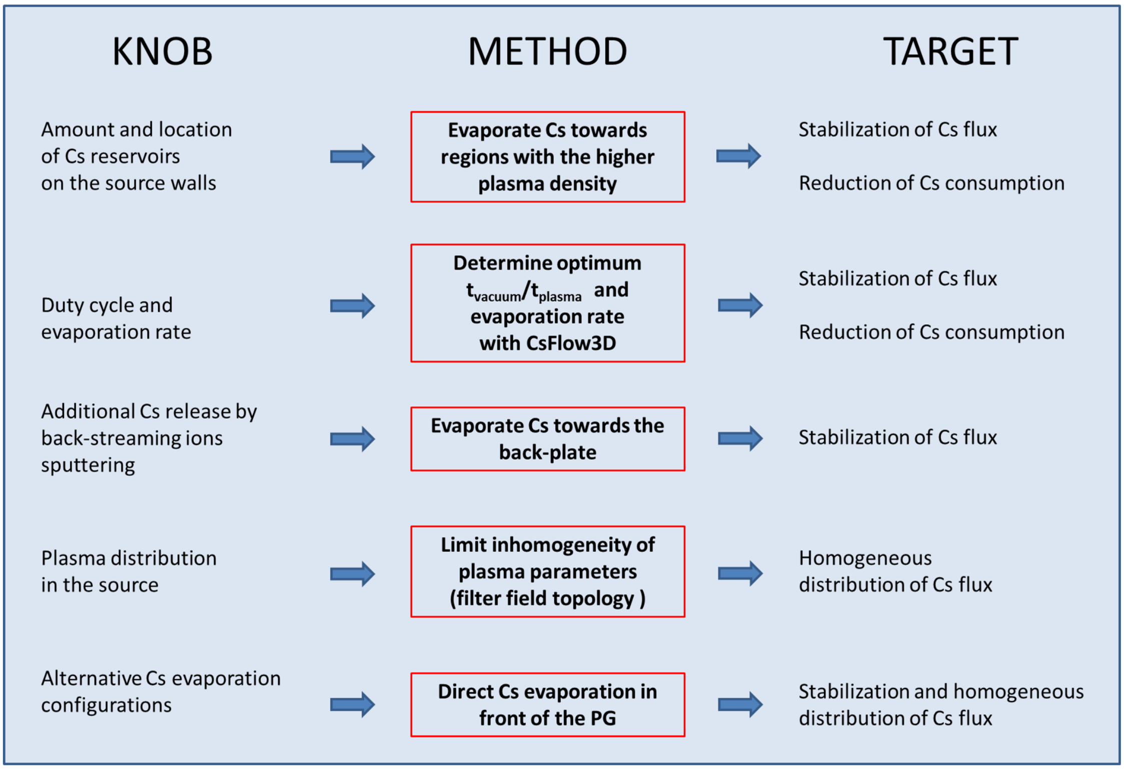

Figure 6.1: Knobs and methods that have been identified in order to optimize the Cs dynamics in negative ion sources, i.e. reaching the targets of a stable and homogeneous distribution of Cs flux as well as a reduction of Cs consumption.

for the evolution of the Cs flux. The available knobs to act on the Cs reservoirs are the orientation of the oven and the duty cycle, in relation with the evaporation rate.

The investigations performed for BATMAN by considering different orientations of the Cs oven nozzle on the top of the back-plate (figure 4.7) have shown that higher and more stable fluxes are achieved when evaporating Cs close to the driver exit, where the plasma-assisted erosion is more efficient.

The variation of the duty cycle performed in the case of the short pulses at ELISE (figure 5.8) shows that for fixed Cs oven configuration, Cs evaporation rate and plasma phase time length, there is a minimum vacuum phase time under which the instability increases. CsFlow3D can be applied to any negative ion sources in order to quantify the minimum time length of the vacuum phase needed, when keeping constant all the other parameters, to improve the stability of Cs flux onto the PG.

A contribution that can strongly help in the stabilisation is represented by the additional Cs release due to the back-streaming ion sputtering, as proved by the long pulse simulations of ELISE. For this process to be efficient, a high Cs coverage on the location where the back-streaming ions hit the back-plate of the source is needed. This translates to a requirement in the design of the Cs oven, that should provide a direct evaporation towards these areas, in order to build up the Cs reservoirs.

6.2 Spatial distribution of the Cs flux

An inhomogeneity in the Cs flux onto the PG can become an issue, because of the presence of regions of the PG where the Cs flux is not sufficient to counteract the work function degradation.

The investigations performed at BATMAN by considering vertical shifts of the plasma clearly revealed that asymmetries in the plasma parameters (i.e. plasma density, electron temperature, plasma potential) induces asymmetries in the Cs distribution. This asymmetry cannot be counteracted by changing the location of the Cs reservoirs on the source walls.

The plasma distribution in the source is strongly affected by the magnetic filter field [34], therefore an optimisation of the filter field topology is a way to limit the inhomogeneity of the plasma distribution. This is however beyond the capability of the CsFlow3D code, in which the plasma parameter map is given as input.

Another way to act on this problem is to change the Cs evaporation concept, in order to avoid relying on plasma-induced erosion of the Cs on the walls and the consequent transport of Cs towards the PG through collisions with the plasma. A system based on the direct evaporation of Cs close to the PG, such as the one investigated for the case ELISE (section 5.3), will allow to have a more uniform caesiation on the entire PG surface.

6.3 Reduction of the Cs consumption

A reduction of the Cs consumption during the source operation can be achieved by optimizing the exploitation of the Cs reservoirs on the wall. The fundamental statement that can be made is that Cs should be evaporated towards the areas of the source walls where it can be more efficiently recovered by means of plasma-induced erosion, i.e. where the plasma density is higher.

This was clearly shown in the simulations performed for the BATMAN test facility in the case of the two ovens, one in the top and one in the bottom and in which an upward shift of the plasma parameter was considered. The fastest conditioning and the highest fluxes onto the PG was achieved when using the top oven (figure 4.15), i.e.

creating the Cs reservoirs on the top, in the same direction of the plasma asymmetry. A confirmation to this fact comes also from the experiments: the same performances (extracted negative ion currents and co-extracted electrons) could be achieved with a lower evaporation rate in the case of the top oven w.r.t. the bottom oven[67].

7 Towards the simulation of the full ITER-NBI source

The next step in the size scaling towards the ITER-NBI sources is the extension of the simulations domain of the predictive code CsFlow3D to the source at the SPIDER test facility [20, 75]. The scaling from the ELISE test facility to SPIDER is shown in figure 7.1, where also the Cs oven position and geometries is indicated. For the case of SPIDER three Cs ovens are foreseen to be mounted on the back-plate of the source, differently to the ELISE case with two ovens on the side walls. In addition, the shape of the Cs oven nozzles for SPIDER is different from the ELISE one.

The modelling of the full source is based on the simulations for the ELISE test facility: the geometrical domain is in fact the vertical extension of the expansion chamber of ELISE, with a total of 8 cylindrical drivers of the same size of the ones at ELISE. The plasma parameter profiles (i.e. electron temperature, plasma density, plasma potential) and the magnetic filter field map are the vertical extension of those used to model the half-size source in ELISE,i.e. replicated for the four drivers in the top and the four in the bottom (details in the appendixes A and B).

Predictions of the Cs flux onto the PG for different evaporation rates are made for SPIDER and compared with the reference values of ELISE. An insight on the time evolution of the Cs flux in the case of a long pulse will be shown as well.

7.1 Cs evaporation in SPIDER

The source at the SPIDER test facility will be equipped with three Cs ovens, which will be positioned on the back-plate of the expansion chamber. The nozzle consists of a horizontal cylindrical injection pipe of 12 mm of diameter with 6 equidistant orifices along the circumference on the lateral surface of the pipe (figure 7.2). The diameter of the orifices is 3.5 mm. In order to avoid direct evaporation towards the plasma grid, the terminal part of the cylindrical injection tube has a larger diameter: this will screen the PG from the direct evaporation of Cs from the orifices. The presented

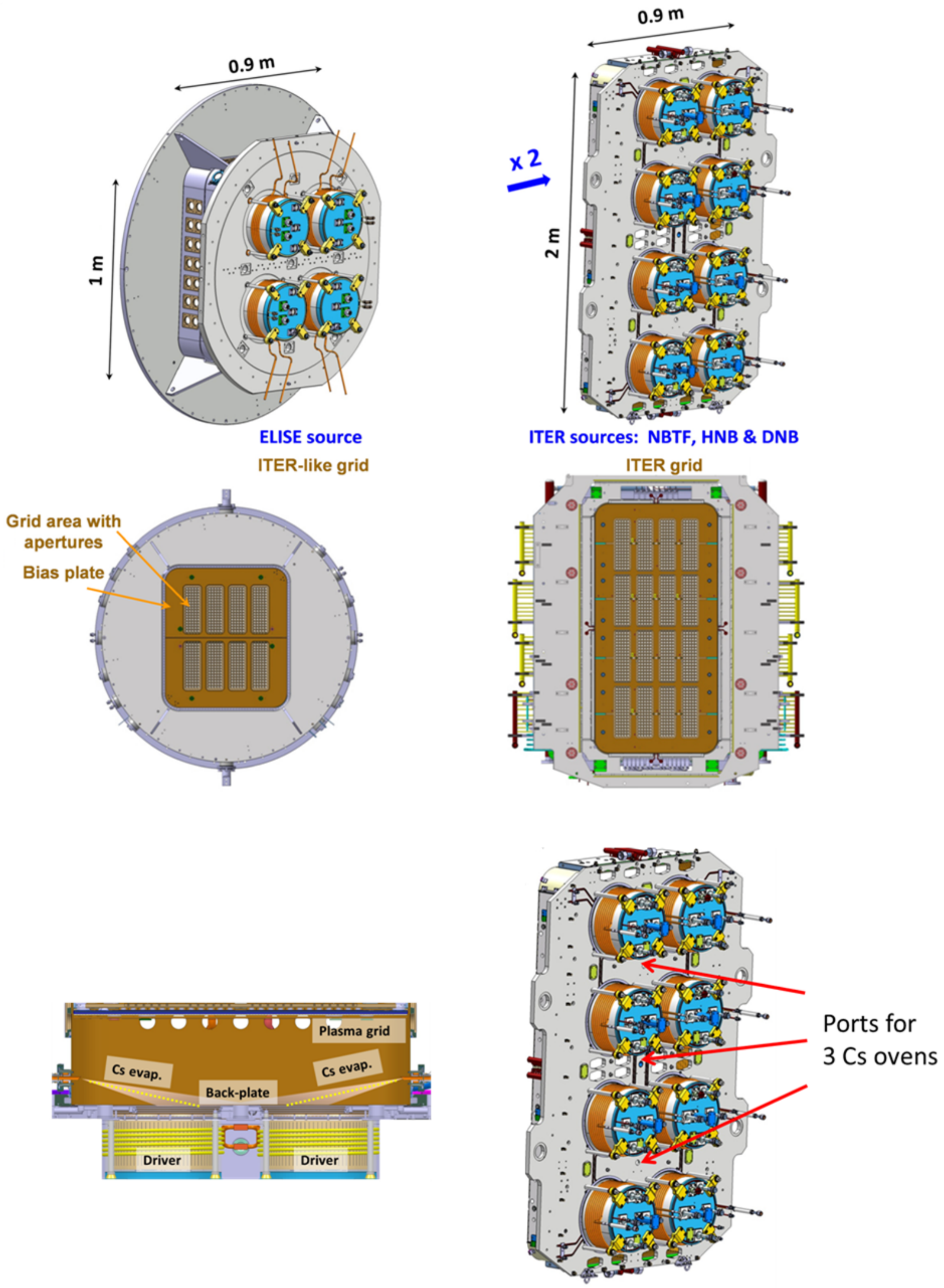

Figure 7.1: Size scaling from the half-size source at the ELISE test facility (2 pairs of drivers) and the full source at the SPIDER test facilities (4 pairs of drivers). A frontal view of the plasma grid and the Cs oven positions for the two test facilities is shown as well.

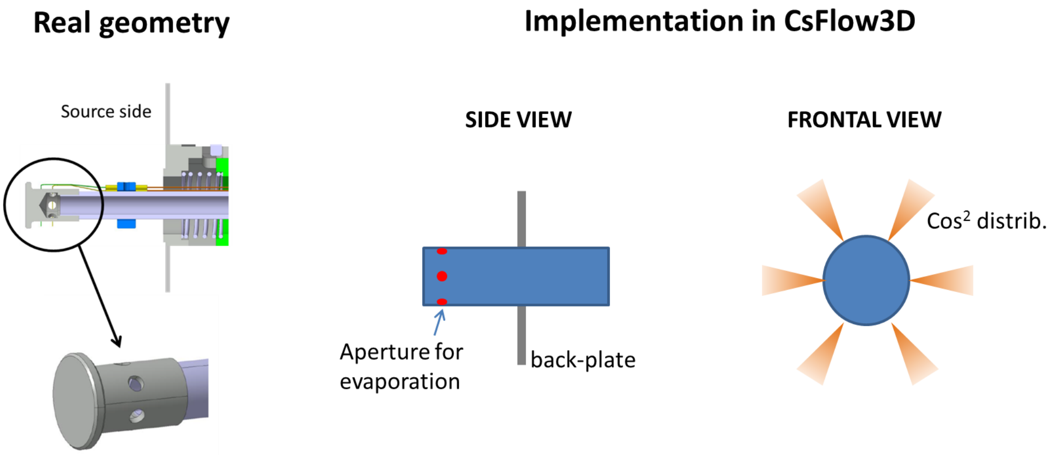

Figure 7.2: Left: Sketch of the real geometry of the Cs oven nozzle foreseen for SPIDER; right: side view and front view of the simplified geometry of the SPIDER Cs nozzles used in CsFlow3D. A squared cosine distribution is assumed for each of the six orifices.

geometry will allow for the deposition of Cs mostly on the walls of the expansion chamber and on the back-plate.

For the simulations of the Cs evaporation inside the source, a simplified version of this nozzle geometry is considered: the schematic frontal and lateral view of the Cs oven nozzle considered in the model is shown in figure 7.2. In this first approximation, the larger shape of the terminal part of the injection pipe is not taken into account. The position of the six orifices on the cylindrical surface is clearly visible on the frontal view schematic, together with the evaporation directions. The size of the pipe and of the orifices, as well as their disposition on the cylindrical surfaces, is the same as for the real design of the SPIDER nozzle. The length of the nozzle inside the source expansion chamber is set to 25 mm.

The evaporation pattern is assumed to follow the squared cosine distribution (section 3.3). A simulation of the real geometry of the Cs oven needs to be performed in the future in order to have a more accurate description of the Cs evaporation pattern. The ending part of the cylindrical pipe could perturb the evaporation pattern from the orifice leading to reflections of the evaporated Cs.

Figure 7.3 shows the Cs coverage on the side wall of the expansion chamber after the 200 s vacuum phase, by using an evaporation rate equal to 5 mg/h/oven, i.e. a total evaporation rate of 15 mg/h. The surface temperatures of the source are set in the same way as for the ELISE test facility, i.e. with the source walls at 35°C and the PG and bias plate at 125°C.

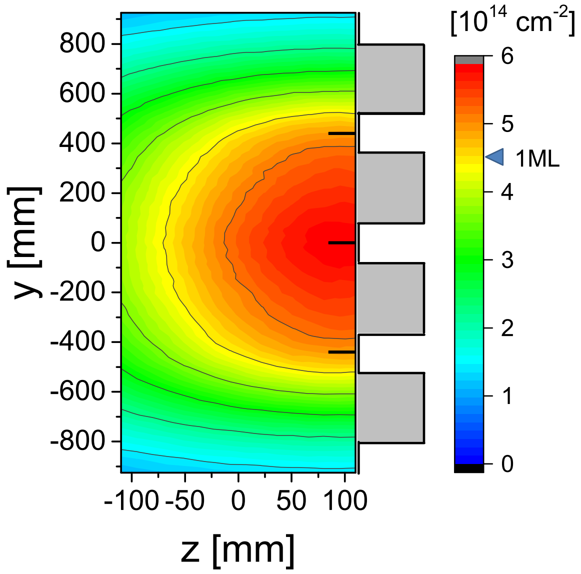

Figure 7.3: Cs coverage on one of the side walls of the expansion chamber after 200 s vacuum phase, with a total Cs evaporation rate of 15 mg/h, i.e. 5 mg/h/oven. The horizontal and vertical axis are not represented in an isometric scale for a better rendering of the plot. On the right the side view of the drivers is displayed (grey areas) and the three Cs oven injection tubes are represented in black.

The maximum value of Cs coverage is located at $y = 0$, i.e. on the vertical centre of the expansion chamber, and it is equal to $\sim 6{\cdot}10^{14}\,\mathrm{cm}^{-2}$. The Cs reservoirs on the wall are vertically symmetric due to the vertical symmetry of the oven nozzles. The hereby presented Cs oven nozzle configuration was used to perform a set of simulations of the source conditioning for different values of Cs evaporation rate: the results will be presented in the following section.

7.2 Scaling of the evaporation rate in comparison with ELISE

The simulation of the standard conditioning phase at SPIDER was performed in the same way as it was done for the ELISE test facility, i.e. with 20 cycles of vacuum phase (200 s) and plasma phase (20 s). In these first simulations, the effect of back-streaming ions was not taken into account, due to the very different acceleration energy which may change the generation of the positive ions as well as the sputtering yield of Cs.

The conditioning phase was simulated for different values of the total evaporation rate, namely 10, 15, 20, 25 and 30 mg/h, equally divided among the three oven nozzles (i.e. for the 18 orifices in total). Figure 7.4 shows the total Cs flux averaged on the area of one beamlet group (highlighted in red) and on the time of the plasma phase, as a function the consecutive pulse number. It can be seen that the Cs flux increases pulse by pulse due to the population and redistribution of the Cs reservoirs during the conditioning phase, as already found for BATMAN and ELISE.

The saturation value of the total Cs flux increases with increasing evaporation rate: for the lowest simulated evaporation rate, i.e. 10 mg/h, an averaged flux of $\sim 9 \cdot 10^{12}\,\mathrm{cm^{-2}s^{-1}}$ is achieved, while for the maximum evaporation rate tested, i.e. 30 mg/h, the flux is above $20 \cdot 10^{12}\,\mathrm{cm^{-2}s^{-1}}$. As a reference the typical value of total Cs flux onto one of the central beamlet group of ELISE for a total evaporation rate of 10 mg/h was taken into account: the reference value resulted $\sim 17 \cdot 10^{12}\,\mathrm{cm^{-2}s^{-1}}$. In order to obtain a value of the flux to the PG close to the one obtained at ELISE, a

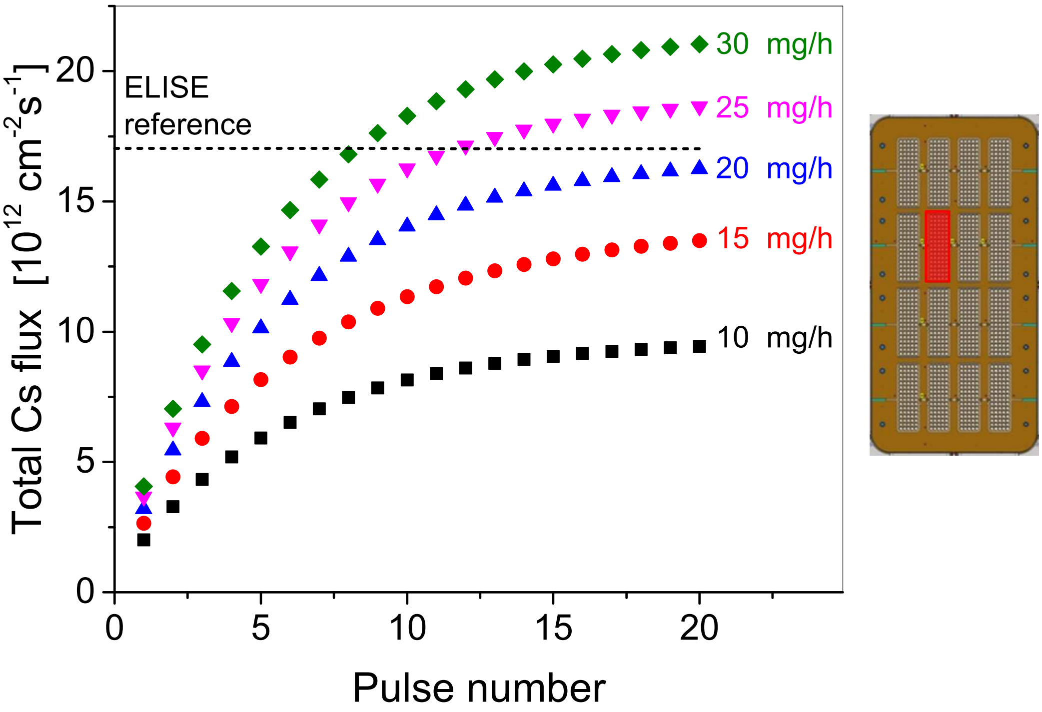

Figure 7.4: Total Cs flux averaged on the area of one beamlet group (highlighted in red) and on the plasma phase time (20 s) as a function of the consecutive pulse number and of the Cs evaporation rate. The vacuum phase between the pulse is 200 s in all the cases.

total Cs evaporation rate of 20 mg/h, corresponding to an evaporation rate for each oven of 7 mg/h/oven, is needed. This is twice as higher as the Cs evaporation rate used in the simulations of ELISE.

This difference much probably relies on the specific geometry and position of the Cs oven nozzle and there might still be margin to optimise in this situation. Also an optimisation of the duty cycle has to be performed.

7.3 Evolution of Cs flux in a long pulse

A long pulse for the SPIDER test facility was simulated after the standard conditioning process with a total evaporation rate of 20 mg/h. The length of the simulated pulse was 400 s, without taking into account the contribution of the back-streaming ion sputtering.

In figure 7.5 the time trace of the total Cs flux averaged on the area of one beamlet group (highlighted in red) is shown. Immediately before the pulse, the Cs flux onto the considered beamlet group is $\sim 10^{12}\,\mathrm{cm^{-2}s^{-1}}$ while at the beginning of the plasma pulse the flux increases more than one order of magnitude up to $18 \cdot 10^{12}\,\mathrm{cm^{-2}s^{-1}}$, due to the plasma assisted removal of Cs from the wall. However, a strong decrease of the flux is visible during the pulse: the behaviour looks very similar to depletion

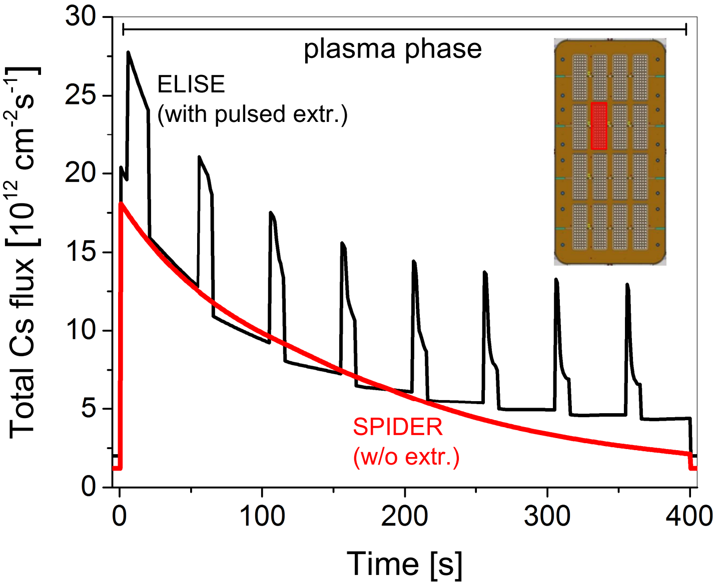

Figure 7.5: Time trace of the total Cs flux onto the highlighted beamlet group for a long pulse (400 s) at the SPIDER test facility.

of the Cs reservoirs already observed also in the long pulse simulations at the ELISE test facility.

A first strategy to improve the stability is acting on the duty cycle of the conditioning phase, which proved to have an effect on the simulations for ELISE in short pulses and that needs to be optimised.

Moreover, the effect of the back-streaming ions needs to be included. It needs to be understood if the Cs sputtered by back-streaming ions can have a relevant stabilisation effect for the Cs flux and eventually identify other factors that can improve the Cs redistribution and reduce the Cs consumption, either in a similar or different way with respect to the prototype source and the half-size source.

The next step will be to have a more realistic definition of the geometry of the Cs oven nozzle as well as a more accurate description of the plasma parameters and the magnetic filter field map. These factors might relevantly change the Cs dynamics, with an impact on the absolute value of the flux and on its distribution and time evolution during the pulse.

8 Summary and conclusions

The neutral beam injection system for the heating and current drive in ITER relies on large and powerful RF driven negative hydrogen ion sources. The RF prototype source in operation at the BATMAN test facility has a size of 1/8 of the full ITER-NBI source size and a single cylindrical driver, where the plasma is generated by inductive coupling. This source became the reference design for the ITER-NBI source (which has a size of $1\,\mathrm{m} \times 2\,\mathrm{m}$ and consists of 8 drivers). An intermediate step towards the ITER-NBI source has been done by developing a half size source ($\sim$1 m ×1 m), which is in operation at the ELISE test facility (IPP Garching) since 2013. The 1:1 prototype of the ITER-NBI source is under construction at the PRIMA test facility, which consists of the SPIDER and MITICA experiments (at Consorzio RFX, Padova, Italy).

The typical duty cycle for BATMAN is 7 s plasma phase (4.5 s beam extraction) and 4 minutes of vacuum phase, while for ELISE the plasma phase can be up to one hour, but with pulsed extraction (10 s every 150 s). In the case of the ITER-NBI source a CW extraction for one hour is foreseen.

The target of the ITER-NBI source will be to deliver an accelerated negative ion current density of $23\,\mathrm{mA/cm^2}$ in hydrogen and $20\,\mathrm{mA/cm^2}$ in deuterium for an overall extraction surface area of $2000\,\mathrm{cm^2}$ and the amount of co-extracted electrons limited below that of negative ions. These values need to be maintained for up to one hour with a spatial homogeneity of the extracted negative ion current density better than 90% over the entire extraction area.

In these sources, negative hydrogen ion generation relies on the surface conversion of atomic hydrogen or positive hydrogen ions on a caesiated surface (plasma grid). Cs is evaporated inside the source to reduce the work function of the plasma grid and to increase the negative ion production efficiency. Cs is however a very reactive element and the reactions on the source surfaces need to be taken into account. The material used for the converter surface is Mo coated Cu; the materials for the other surfaces of the source are Mo, Cu, Ni (the latter in the case of the source walls at ELISE). Cs can create strong bonding with the impurities present on the surfaces and form very stable compounds. The background gas pressure in the source during the vacuum phase is in the range $p \sim 10^{-5} - 10^{-4}\,\mathrm{Pa}$: this leads to a flux of impurities on the source surfaces which is comparable or even larger than that of Cs. The presence of Cs compounds leads to a degradation (i.e. increase) of the work function of the plasma grid, where the formation of negative ions takes place. For this reason a sufficient Cs flux onto the plasma grid during the source operation needs to be maintained. An increase of the surface work function is correlated to a lower production yield of negative ions: for the quasi neutrality principle this will lead to an increase of the electron density and therefore to an undesired increase of the co-extracted electrons.

Cs is seeded inside the source through one or more nozzles by heating up a Cs reservoir and the evaporated Cs can deposit on the source inner surfaces. During the plasma pulse, in addition to the evaporation from the oven, Cs can be released from the surfaces by means of several processes, such as thermal desorption and physical or chemical sputtering. The released Cs is then transported through the source volume and undergoes collisions with the plasma particles and with the background gas.

The Cs evaporation rate cannot be increased indefinitely, because an excessive amount of Cs can create problems for the source operation. It was experimentally observed that an excessive amount of Cs inside the driver (where the plasma is generated) can change the plasma parameters, as detected by a reduction of the H_α light emission in the driver. This correlates experimentally with a reduction of the extracted negative ion current. The leakage of Cs through the plasma grid apertures from the source to the grid system can be harmful for the high voltage holding.

The dynamics of Cs is a very complex process, since it involves many factors, such as the pattern of evaporation from the Cs oven, the sticking probability of Cs on the source surfaces (which depends on the temperatures and on the flux of impurities) and on the plasma distribution, which can strongly affect the transport of Cs inside the source volume. The interaction of these factors and their relevance to Cs dynamics can be investigated by numerical simulations.

The CsFlow3D code was developed in 2009 at IPP Garching in order to numerically model the Cs dynamics in negative ion sources. The code is a Monte Carlo test particle code which models the entire geometrical domain of the source. It is able to calculate the coverage of Cs on the source inner surfaces and the fluxes of the Cs atoms and ions onto the surfaces. Some important insight on Cs dynamics were already gained from preliminary simulations applied to the prototype source, such as the role of the accumulation of Cs reservoirs on the source walls for the temporal evolution of Cs dynamics. However, a direct and quantitative benchmark of the code against experimental data was not possible at that time since neither fluxes nor coverage, which were the only outputs of the code, can be measured in the test facilities.

The goal of this work was to develop a predictive code for the optimization of the caesiation of the ITER-NBI sources, as well as the reduction of the Cs consumption, which is of particular importance for the DEMO NBI-sources, in order to minimise their maintenance requirement.

In a first stage the benchmark of the CsFlow3D code against the experimental data of the prototype source at BATMAN has been carried out. In order to allow for direct comparisons between experimental measurements and code results, CsFlow3D has been updated with the possibility of calculating the neutral Cs density along specific lines of sight, i.e. those used by the experimental diagnostic TDLAS (Tunable Diode Laser Absorption Spectroscopy), which can detect the line averaged neutral Cs density.

A fundamental input parameter needed is the evaporation pattern of Cs from the oven nozzle, which can be different from the cosine distribution of an ideal orifice, depending on the nozzle geometry. The molecular flow of Cs from different nozzle geometries used at the IPP test facilities BATMAN and ELISE has been modelled with DSMC (Direct Simulation Monte Carlo) methods. The evaporation pattern results to be narrower w.r.t. the ideal orifice condition and it can be reproduced by a squared cosine function, which is therefore implemented in the CsFlow3D code. The evaporation rate for the Cs oven in the prototype source was chosen in agreement with experimental observation, i.e. 10 mg/h.

The application of the code to BATMAN shows values of the Cs flux (neutral Cs) onto the plasma grid during the vacuum phase of the order of $10^{12}\,\mathrm{cm}^{-2}\mathrm{s}^{-1}$. During the plasma phase of 8 s the Cs flux, which consists mostly of positive Cs ions, is up to 40 times higher than the flux during the vacuum phase. The code confirmed the preliminary investigations: most of the Cs flux ($\sim 90\%$) reaching the plasma grid during the pulse is the one released by plasma contact with the source walls and not by the direct evaporation from the oven. A repetition of the cycle of plasma phase (8 s for the prototype source) and vacuum phase (4 minutes) results in an increase of the Cs flux due to the progressive population of the Cs reservoirs on the surfaces of the source walls.

The investigations performed at the BATMAN test facility have revealed that the distribution of Cs inside the source is strongly dependent on the plasma distribution. This was proved by implementing in the code a vertical shift of plasma parameters (i.e. plasma density, electron temperature, plasma potential): the larger this shift is, the higher the vertical asymmetry of Cs distribution. The role of the position of the Cs ovens, i.e. of the Cs reservoirs on the walls, is much less relevant for the Cs distribution during the plasma phase, as shown by comparing the simulations for the position of the oven on the top and on the bottom of the back-plate. The effect of the oven position is mainly in the speed of the conditioning process towards a stable value of Cs flux. The conditioning process is in fact faster when the Cs is evaporated towards the region of the inner surfaces where plasma is more intense and thus the plasma assisted removal of Cs from the surface.

The results of the simulations have been compared with the experimental time traces of TDLAS (Tunable Diode Laser Absorption Spectroscopy), for the two horizontal lines of sight used at the prototype source. The value of line averaged neutral Cs density calculated by the code are of the order of $10^{15}\,\mathrm{m}^{-3}$ and the simulated time traces result quantitatively in agreement with the experimental measurements.

The benchmark of the code at the prototype source can therefore be considered successful, since the experimental data are reproduced by the simulations: CsFlow3D can then be used to make predictions about Cs dynamics and distribution in negative ion sources.

The predictive capability of the code has been used to optimize the position of the Cs oven at BATMAN with a modified driver shape, i.e. a race-track driver. The constraints of the optimization were the limitation of the Cs deposited on the driver and of the Cs lost through the apertures of the grid system. The best compromise has been achieved by positioning the Cs oven nozzle on the centre of the driver back-plate, so that it evaporates horizontally towards the plasma grid. This configuration was tested experimentally and the source could be operated up to high performances, comparable to those obtained with the previous cylindrical driver.

When extending the code to ELISE, a new aspect was revealed by the simulations, i.e. the high relevance of the back-streaming positive ion sputtering of Cs from the source back-plate. For BATMAN this contribution can be neglected, mostly for geometrical reasons, while it plays a very important role for the source at ELISE (and for the ITER sources), due to the higher footprint area of the plasma grid apertures on the back-plate. An increased value of neutral Cs density is measured by TDLAS when switching on the extraction: the simulated time traces show the same effect and are in good agreement with the experimental ones. In addition, a correlation has been identified between the beam optics and the increase of Cs density measured by TDLAS during the beam extraction, thus proving experimentally that the back-streaming ions act as an additional Cs source term during the beam-extraction phase.

The short pulse simulations (i.e. 20 s plasma phase) of ELISE have shown that the duty cycle influences both the absolute value of Cs flux and its stability. For a total evaporation rate of Cs equal to 10 mg/h, at least a vacuum phase time of 400 s is necessary in order to improve the stability of the Cs flux during the plasma phase.

The temporal stability of Cs flux is a particular issue during long pulses (in the order of hundreds of seconds), since it is related to the stability of the plasma grid work function. The experiments show that the long pulse operation in ELISE is limited by the rapid increase of the co-extracted electrons in time, which is an indication of the degradation of the work function of the plasma grid. Simulations confirm that a strong reduction of the total Cs flux (i.e. neutrals and ions) occurs in a long pulse: from $\sim 30 \cdot 10^{12}\,\mathrm{cm}^{-2}\mathrm{s}^{-1}$ to $\sim 5 \cdot 10^{12}\,\mathrm{cm}^{-2}\mathrm{s}^{-1}$, i.e. a factor of 6 within 400 s. This reduction is related to the depletion of the Cs reservoirs.

For every simulated beam extraction phases, an increased Cs flux is observed, suggesting a beneficial effect due to the back-streaming ion sputtering. A simulation for a continuous extraction has been therefore performed, but this additional release of Cs is not enough to stabilise the Cs flux onto the plasma grid during the entire pulse: also the Cs reservoirs on the back-plate are depleted during a long pulse. However, the situation changes drastically when an unlimited amount of Cs on the entire back-plate is implemented in the simulations: the sputtered Cs in this condition can significatively contribute in stabilising and maintaining a higher Cs flux (up to 7 times higher than the case with the normal coverage). This is a proof of principle that back-streaming ions can be exploited to avoid the Cs flux reduction, provided that enough Cs is deposited on the entire back-plate surface.

An alternative Cs evaporation configuration has been tested with the simulations, with the purpose of achieving a better control of the caesiation of the plasma grid. The idea is to evaporate Cs very close to the plasma grid, by creating a kind of *Cs shower*: the Cs flux onto the plasma grid is basically determined by the direct evaporation and it is independent on plasma redistribution and on the depletion of the Cs reservoirs. Another advantage of this configuration is that most of the Cs flux onto the grid consists of atomic hydrogen and not of positive ions, as in the case of the standard configurations, relying on plasma redistribution. During the experiments in fact the plasma grid is positively biased w.r.t. the source body, in order to attract the electrons towards the plasma grid surfaces and reduce the amount of co-extracted electrons. This electron attracting sheath, however, acts as a positive ion repeller. With the standard oven configuration, most of the Cs flux consists of positive ions, which can be reflected by the repelling potential. By using this alternative evaporation configuration instead, the Cs flux onto the grid mostly consists of neutral Cs and it will not be affected by the plasma grid bias potential.

As a further step towards the simulations of Cs dynamics in the full size ITER-NBI source, predictions of the Cs fluxes onto the plasma grid for SPIDER have been made: the geometry of the ELISE has been vertically extended, by considering four pairs of drivers, and all the input parameters (e.g. plasma parameters profile, magnetic filter field) are deduced from those used for the ELISE simulations. The predictions show that in order to achieve the same flux as those measured at the ELISE test facility during a short pulse of 20 s, the total evaporation rate of Cs in the source needs to be 20 mg/h (i.e. 7/,mg/h/oven), which is almost the double as the one assumed for ELISE. The simulation for a long pulse in which a conditioning phase of 20 pulses with 20 mg/h is assumed, show a similar behaviour as in ELISE, i.e. a strong and fast reduction of the Cs flux in time. However, the effect of the back-streaming ion sputtering is not included in these simulations of SPIDER operation: this might change significantly the amount and stability of the Cs redistribution and therefore further investigations are planned.

The knowledge achieved during this PhD thesis by comparing the predictions obtained by the CsFlow3D code and the experimental observations at the test facilities BATMAN and ELISE, allows the identification some methods for the optimization of the Cs management in the NBI sources for ITER as well as for DEMO:

- The Cs oven nozzles should be designed and positioned to evaporate Cs towards the regions where it can be more efficiently recovered by the plasma. If a plasma drift is present in the source, it is advisable to evaporate the Cs in the same direction of the plasma drift. This allows for a reduction of Cs consumption by achieving a faster conditioning process.

- The evaporation towards the source back-plate is also beneficial, in order to exploit the additional Cs release due to back-streaming ion sputtering in long pulses.

- If the plasma in the source is highly inhomogeneous, with the standard evaporation configurations used in BATMAN and ELISE, there is no efficient way to avoid inhomogeneity of Cs distribution. In such cases, an alternative Cs evaporation configuration, such as a direct and distributed evaporation in front of the plasma, should be considered, to achieve a caesiation independent on the plasma.

A Plasma parameters

The modelling of the collisions inside the source volume needs a 3D map of the plasma parameters, i.e. plasma density, electron temperature, plasma potential as well as the hydrogen gas density and temperature profiles.

A.1 Prototype source

Coordinate system

Figure A.1 shows the coordinate system used to model the source: x and y axis are in the vertical plane, while z axis is along the source axis. The zero of the coordinate system corresponds to the geometrical centre of the expansion region, i.e. positive

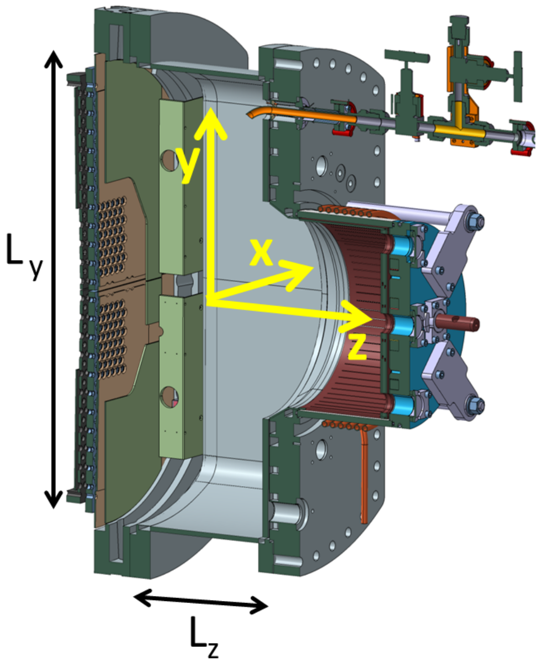

Figure A.1: Schematic view of the coordinate system for the prototype source: the origin is in the centre of the expansion chamber.

values of z are in the direction of the driver. $L_y = 59\,\mathrm{cm}$ and $L_z = 24\,\mathrm{cm}$ indicates length of the expansion chamber respectively in the y and z direction. A radial coordinate is used for the 3D map of the plasma parameters and it is defined as the distance from a general point (x,y,z) inside the source from the source axis, i.e.:

$$r = \sqrt{(x^2 + y^2)}. \tag{A.1}$$

Plasma density

The 3D map of the plasma density used in CsFlow3D is based on experimental measurements [76, 77]. The profile is axi-symmetric w.r.t. the driver axis. Inside the expansion chamber the plasma density is calculated as:

$$n\left(r,z\right) = n_0 \exp\left[2\frac{z}{L_\mathrm{z}} - 1\right] \cdot p_\mathrm{radial}(z,r) \quad \left[\mathrm{m}^{-3}\right]. \tag{A.2}$$

Eq. (A.2) indicates an exponential decay along the z direction from the driver towards the plasma grid. The value of n_0 is the maximum plasma density inside the driver, for the case of the prototype source it is set to $15 \cdot 10^{17}\,\mathrm{m}^{-3}$. The radial profile $p_\mathrm{radial}(z,r)$ is given by:

$$p_\mathrm{radial}(z,r) = \frac{1}{1 + 1.49\left(\frac{r - r_\mathrm{c}(z)}{\lambda(z)}\right)}. \tag{A.3}$$

The parameters $r_\mathrm{c}\left(z\right)$ and $\lambda\left(z\right)$ depend on the axial position z and define the shape of the radial profile. They are defined as:

$$r_\mathrm{c}\left(z\right) = 0.15 - 0.015\left(2\frac{z}{L_\mathrm{z}} + 1\right), \tag{A.4}$$

$$\lambda\left(z\right) = 0.05 - 0.01\left(2\frac{z}{L_\mathrm{z}} + 1\right). \tag{A.5}$$

Inside the driver volume only a radial dependence is considered:

$$n\left(r\right) = \frac{n_0}{1 + 1.49\left(\frac{r - 0.12}{0.03}\right)} \quad \left[\mathrm{m}^{-3}\right]. \tag{A.6}$$

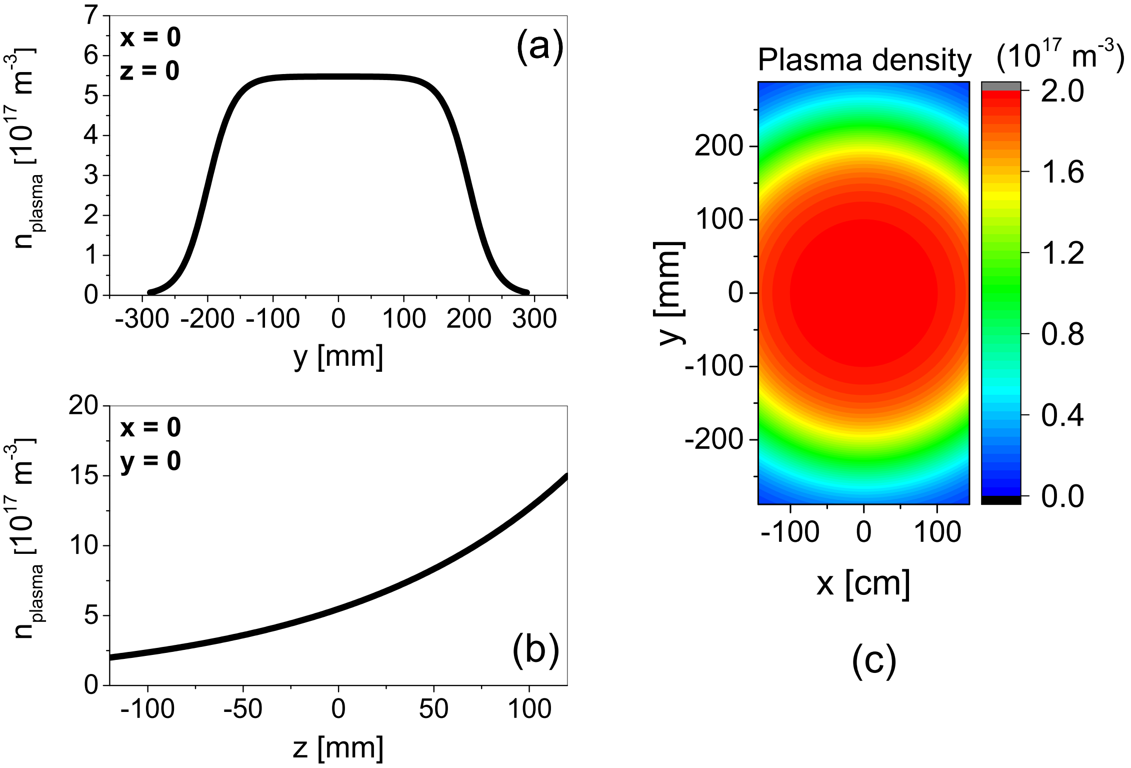

Figure A.2: Profiles of plasma density used by CsFlow3D for the prototype source: (a) Vertical profile at $x = 0$, $z = 0$; (b) axial profile at $x = 0$ and $y = 0$; (c) 2D plot profile in front of the plasma grid.

Figures A.2 (a) and (b) show the radial profile of the plasma density at $z = 0$ and its axial profile at $r = 0$. Figure A.2 (c) shows a 2D plot of the plasma density in front of the plasma grid as calculated from eq. (A.2).

Electron temperature

The 3D map of the electron temperature is generated by using the same radial profile used for the plasma density. Absolute values are retrieved from experimental probe measurements [78]. For the expansion region, the following equation is used:

$$T_{\mathrm{e}}\left(r,z\right) = T_0 \exp\left[\frac{1}{0.52}\left(2\frac{z}{L_{\mathrm{z}}} - 1\right)\right] \cdot p_{\mathrm{radial}}(z,r) \quad [\mathrm{eV}]\,. \tag{A.7}$$

where $p_{\mathrm{radial}}(z,r)$ is the radial profile described previously in eq. (A.3) and $T_0 = 20\,\mathrm{eV}$. T_{e} decays exponentially along the expansion chamber, as shown in figure A.3. Inside the driver a constant electron temperature of 20 eV is used.

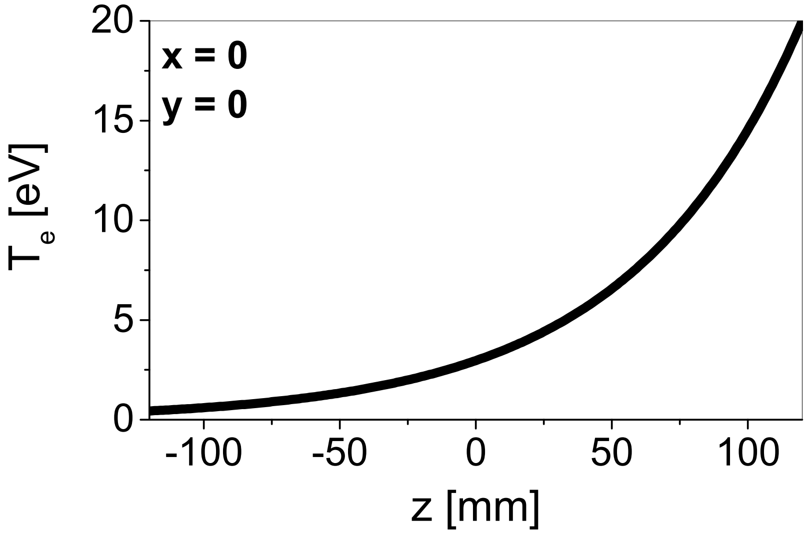

Figure A.3: Axial profile of the electron temperature in the prototype source according to equation (A.7)

Plasma potential

A map of the plasma potential was derived from Langmuir probe measurements performed in different position inside the source [78, 76]. In the expansion region a parabolic dependence on the radial coordinate and an exponential decay along the z axis are used:

$$\phi\left(r,z\right)=\phi_0\left(z\right)\cdot\left(1-a\left(z\right)r^2\right)\quad[V] \tag{A.8}$$

$$a\left(z\right)=0.1\left(1-2\frac{z}{L_\mathrm{z}}\right)\frac{1}{L_\mathrm{y}^2} \tag{A.9}$$

$$\phi_0\left(z\right)=40\exp\left[0.5\left(1-2\frac{z}{L_\mathrm{z}}\right)\ln\left(\frac{1}{2}\right)\right] \tag{A.10}$$

Inside the driver a linear scaling with z is used:

$$\phi\left(r,z\right)=40+14.28\left(\frac{z-z_\mathrm{PG}}{L_\mathrm{z}}\right)\quad[V] \tag{A.11}$$

The value of plasma density, electron temperature and plasma potential used in the code for the positions close to the PG and in the driver are summarized in table A.1.

	Driver	PG
Plasma density	$15{\cdot}10^{17}\,\mathrm{m}^{-3}$	$2.5{\cdot}10^{17}\,\mathrm{m}^{-3}$
Electron temperature	20 eV	0.7 eV
Plasma potential	50 V	20 V

Table A.1: Plasma parameter in value in the driver and in the PG at x=0 at the BATMAN test facility.

Modelling of the plasma drift Experimental measurements performed with Langmuir probes in the prototype source [34, 35] as well as numerical simulations [36] showed the presence of vertical plasma drift due to the magnetic filter filed. In order to take into account this vertical asymmetry due to plasma drift in the CsFlow3D code, a vertical displacement of the plasma parameters (i.e. plasma density, electron temperature and plasma potential) is considered. The shift of the plasma parameters depends on the axial coordinate z, being maximum close to the plasma grid, where the magnets are located, and zero in the driver. By defining $q\,(x, y, z)$ as the map of a generic plasma parameter without drift, the vertically shifted map inside the expansion chamber can be expressed as:

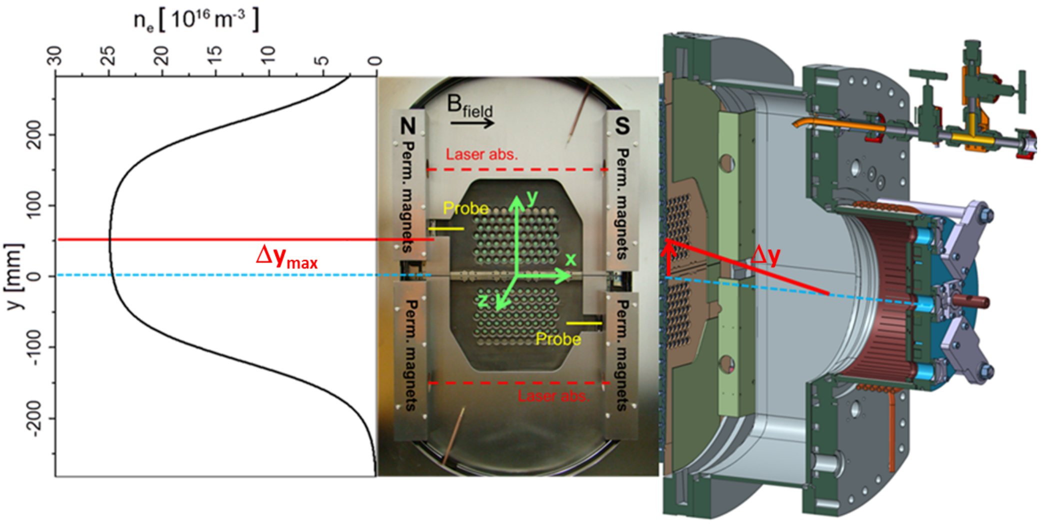

Figure A.4: Sketch of the prototype source at the BATMAN test facility: the location of permanents magnets and of the Langmuir probes is highlighted and a shifted profile of plasma density is shown on the left.

$$q_{\mathrm{withdrift}}\left(x,y,z\right)=q\left(x,y-\Delta y\left(z\right),z\right) \tag{A.12}$$

where the vertical displacement of $\Delta y\left(z\right)$ is a linear function of the axial coordinate z:

$$\Delta y\left(z\right)=\Delta y_{\mathrm{max}}\left(\frac{1}{2}-\frac{z}{L_{\mathrm{z}}}\right) \tag{A.13}$$

From eq. (A.13) it results that Δy is zero ad the driver exit ($z=L_{\mathrm{z}}/2$) and equals Δy_{max} at the plasma grid position ($z=-L_{\mathrm{z}}/2$). Figure A.4 shows a sketch of the prototype source with the axial dependence of the parameter $\Delta y\left(z\right)$ and the corresponding shifted profile of the plasma density in front of the plasma grid for a $\Delta y_{\mathrm{max}}=5\,cm$.

A.2 ELISE test facility

The coordinate system used for ELISE is analogues to that used for the prototype source, i.e. x and y on the vertical plane and the zero positioned in the geometrical centre of the expansion chamber (figure A.5). Four radial coordinates can be defined,

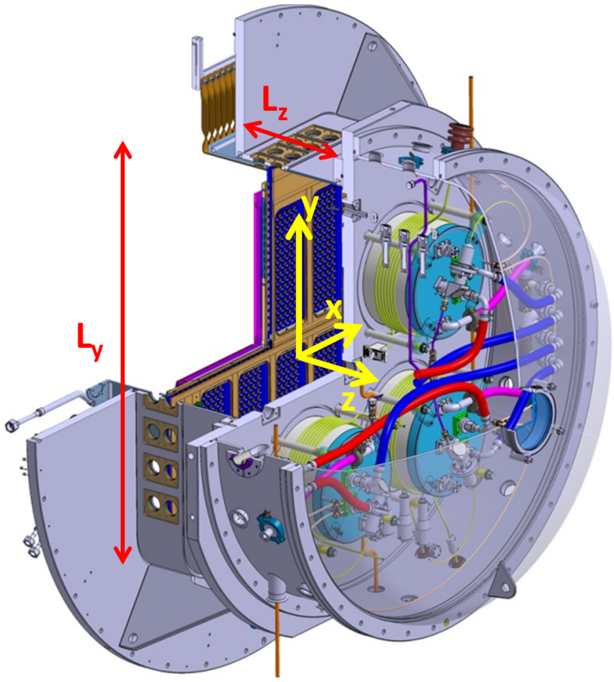

Figure A.5: Schematic view of the coordinate system for the source at ELISE: the origin is in the centre of the expansion chamber.

with respect to the four drivers, i.e.:

$$r_i\left(x,y\right)=\sqrt{\left(x-x_i\right)^2+\left(x-x_i\right)^2} \tag{A.14}$$

where (x_i, y_i) with $i = 1, ..., 4$ are the coordinates of the center of the four drivers.

The 3D map of the plasma parameters inside the expansion chamber were modelled by considering the sum of four radial profiles (as in eq. (A.3)) for each driver. The resulting profile is therefore expressed as:

$$p_{\text{radial,ELISE}}\left(x,y,z\right)=\frac{\sum_{i=1}^{4}p_{\text{i}}\left(r_{\text{i}},z\right)}{\int_{L_{\text{x}},L_{\text{y}}}\left(p_i\left(r',z\right)\right)2\pi r'dr'} \tag{A.15}$$

where p_i is the radial profile relative to the axis of the i-th driver as calculated for the prototype source (eq. (A.3)) and the integral is a normalisation factor.

The plasma density inside the expansion chamber for ELISE is given by the formula:

$$n\left(x,y,z\right)=n_0\exp\left[0.8\left(2\frac{z}{L_{\text{z}}}-1\right)\right]\cdot p_{\text{radial,ELISE}}(z,r)\quad\left[\text{m}^{-3}\right] \tag{A.16}$$

	Driver	PG
Plasma density	$10{\cdot}10^{17}\,\text{m}^{-3}$	$2{\cdot}10^{17}\,\text{m}^{-3}$
Electron temperature	20 eV	0.7 eV
Plasma potential	50 V	20 V

Table A.2: Plasma parameter in value in the driver and in the PG at x=0 at the ELISE test facility.

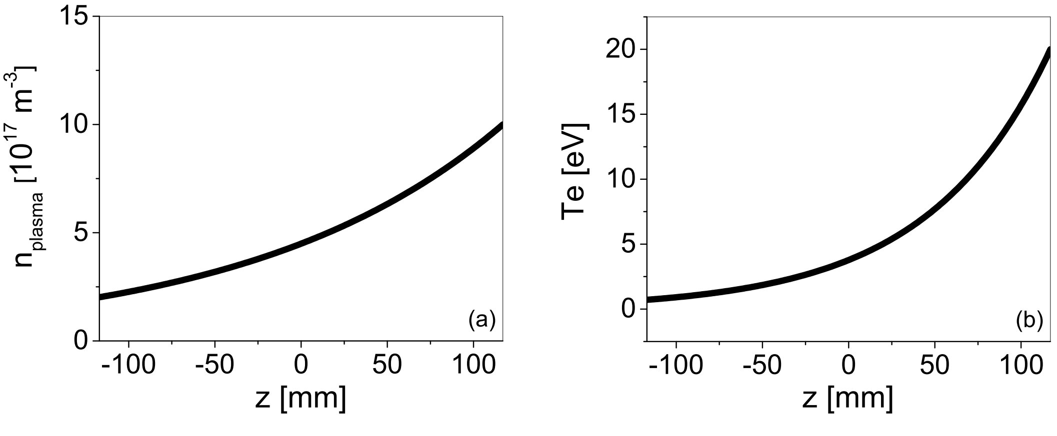

Figure A.6: Axial profile of the plasma density and electron temperature for ELISE.

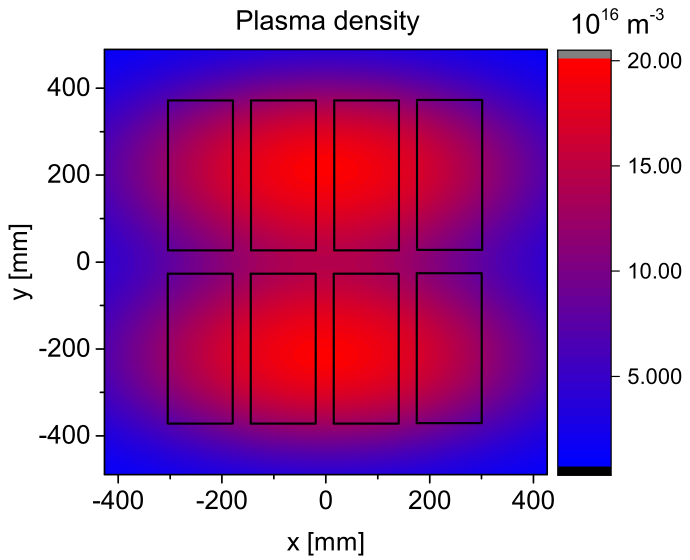

Figure A.7: Plasma density profile at the PG for the source at the ELISE test facility.

where n_0 is the maximum plasma density inside the driver, for the case of ELISE the value $10 \cdot 10^{17}\,\mathrm{m}^{-3}$. Inside the driver i only the radial dependence is considered, i.e.:

$$n(r_i) = \frac{n_0}{1 + 1.49\left(\frac{r_i - 0.12}{0.03}\right)} \quad \left[\mathrm{m}^{-3}\right]. \tag{A.17}$$

The electron temperature in the expansion chamber is calculated with the equation:

$$T_\mathrm{e}(x, y, z) = T_0 \exp\left[\frac{1}{0.6}\left(2\frac{z}{L_\mathrm{z}} - 1\right)\right] \cdot p_{\mathrm{radial,ELISE}}(x, y, r) \quad [\mathrm{eV}] \tag{A.18}$$

with $T_0 = 20\,eV$, i.e. the electron temperature in the driver.

Similarly to eq. (A.15), the profile of the plasma potential inside the expansion chamber is determined by the sum of four parabolic profiles and by the exponential decay along the source axis z:

$$\phi(r, z) = \phi_0(z) \cdot \frac{\sum_{i=1}^{4}\left(1 - a(z)\, r_i^2\right)}{\int_{L_\mathrm{x}, L_\mathrm{y}}\left(1 - a(z)\, r_i^2\right) 2\pi r dr} \quad [V] \tag{A.19}$$

where a(r) is calculated similarly to equation A.9 and the exponential decay along the z axis is given by:

$$\phi_0\left(z\right) = 40\exp\left[0.5\left(1-2\frac{z}{L_{\mathrm{z}}}\right)\ln\left(\frac{1}{2}\right)\right] \tag{A.20}$$

The axial profile of plasma density and electron temperature at $x = 0$ and $y = 0$ is given in figure A.6 (a) and (b) respectively. The 2D plot of the plasma density in front of the plasma grid is shown in figure A.7. The value of plasma density, electron temperature and plasma potential for the region close to the PG and for the driver are summarized in table A.2.

B Electric and Magnetic Field

B.1 Prototype source

In order to calculate the Lorentz force acting on Cs ions, the 3D map of the electric and magnetic fields inside the source is needed. Electric fields can be calculated as the gradient of the plasma potential described in A. The magnetic filter field in the case of the prototype source at the BATMAN test facility is generated by permanent magnets: the 3D map can be calculated by using Permag code [79]. In

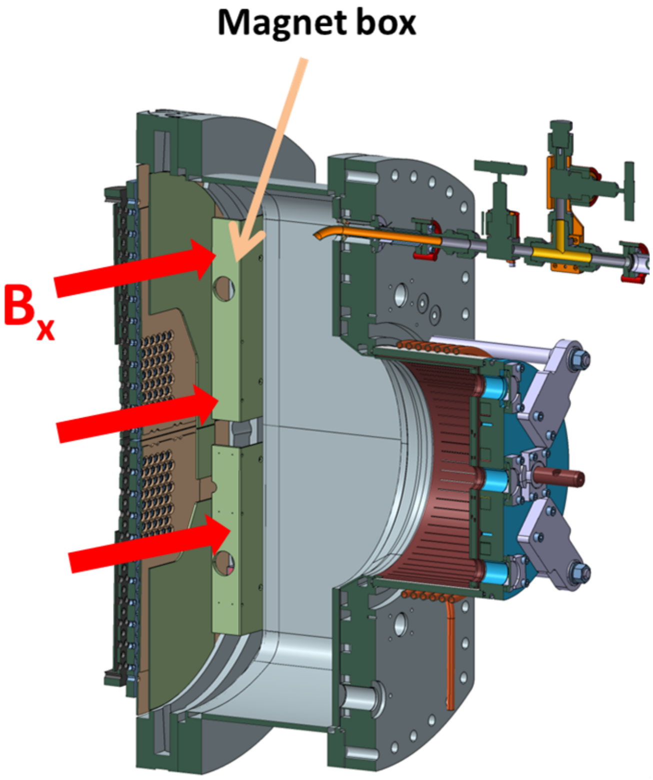

Figure B.1: Schematic of the source showing the position where permanents magnets are located and the direction of the generated magnetic field in the horizontal direction.

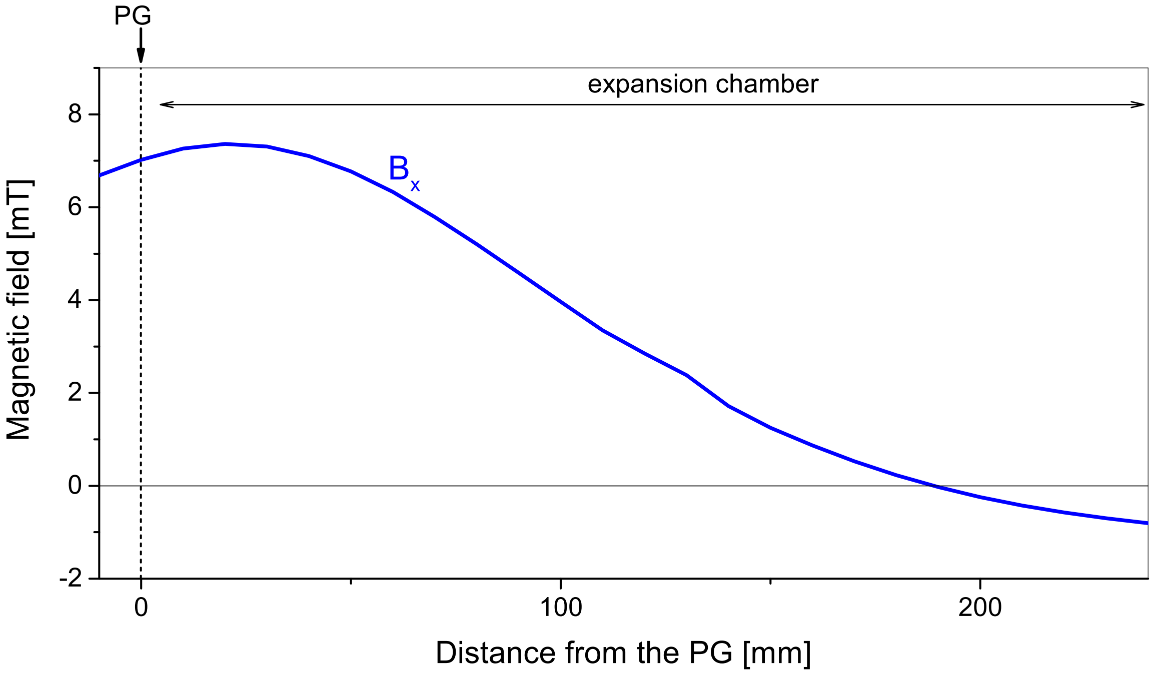

Figure B.2: Profile of the horizontal component of the magnetic filter field (standard configuration) as function of the distance from the plasma grid at the prototype source [81].

the standard configuration the rods of permanent magnets are mounted inside the diagnostic flange [80], at a distance of 3 cm from the plasma grid, as indicated in figure B.1. Figure B.2 shows the horizontal component B_{x} (which is the predominant component) along the axis of the source as a function of the distance from the plasma grid. The maximum magnetic field strength in the standard configuration in front of the PG is equal to ~ 7 mT.

B.2 ELISE test facility

At the ELISE test facility, the horizontal magnetic filter field is generated by means of a current flowing through the plasma grid [32].

Simulations with ANSYS [82] were performed in order to obtain a 3D map of the magnetic filter field inside the source volume. Figure B.3 shows the 3D representation of the results of the ANSYS simulations performed for a current of 1 kA. With this value of plasma grid current a magnetic field intensity of ~ 1 mT can be achieved in front of the PG.

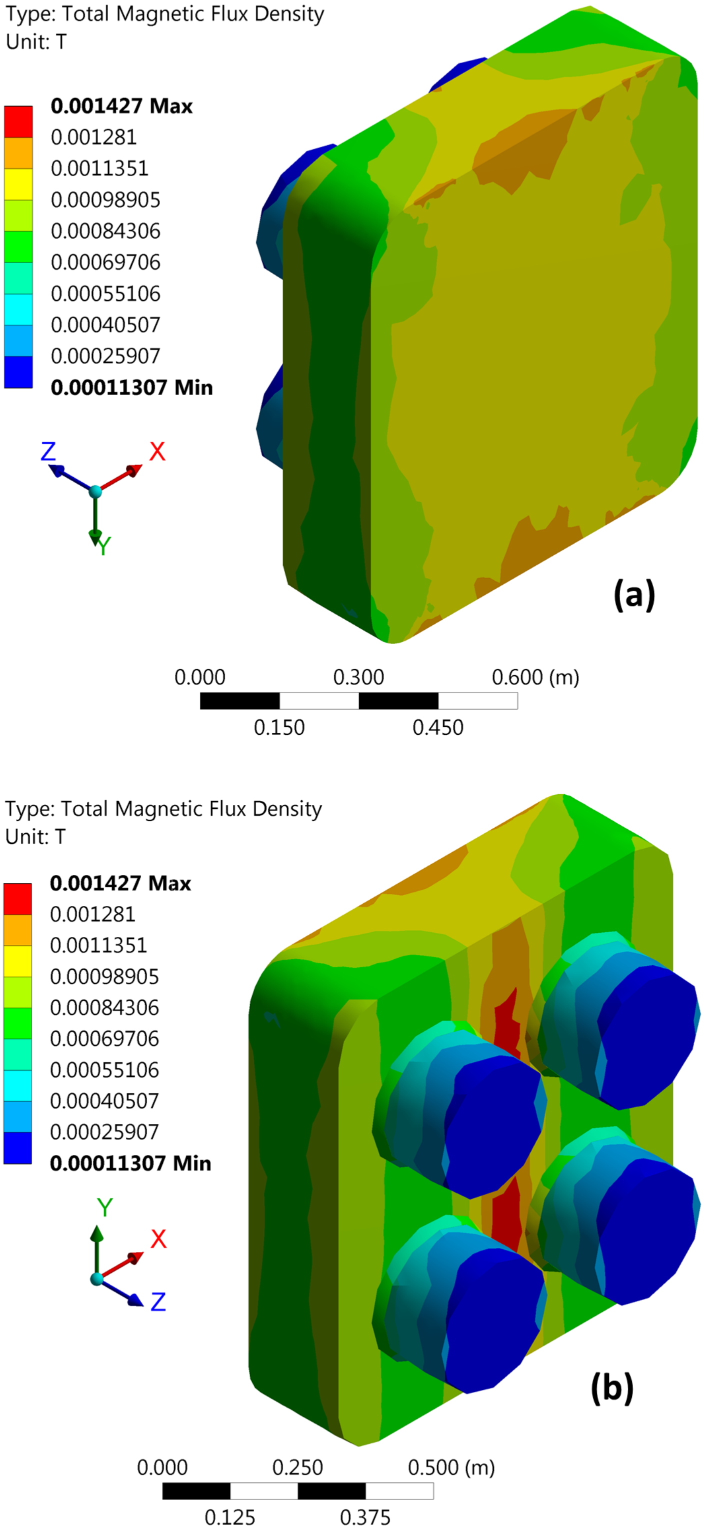

Figure B.3: 3D magnetic filter field map calculated for ELISE by ANSYS simulations: (a) view of the plasma grid side; (b) view of the driver side [83].

B.3 SPIDER test facility

For the preliminary modelling of SPIDER, the magnetic filter calculated for ELISE was considered. In particular the magnetic field on the horizontal plane passing through the centre of the source was considered, i.e:

$$\mathbf{B}_{\text{SPIDER}}\left(x,y,z\right)=\mathbf{B}_{\text{ELISE}}\left(x,0,z\right) \tag{B.1}$$

This allows to avoid the edge effects that can appear at the boundaries of the magnetic field calculation domain of ELISE.

Bibliography

[1] J. Wesson, *Tokamaks (Oxford engineering science series)*, Oxford University Press, 1997.

[2] M. Shimada, D.J. Campbell, V. Mukhovatov et al., *Chapter 1: Overview and summary*, Nuclear Fusion **47** (2007), no. 6, S1–S17.

[3] G. Federici, R. Kemp, D. Ward, C. Bachmann, T. Franke, S. Gonzalez, C. Lowry, M. Gadomska, J. Harman, B. Meszaros, C. Morlock, F. Romanelli, and R. Wenninger, *Overview of EU DEMO design and R&D activities*, Fusion Engineering and Design **89** (2014), no. 7-8, 882–889.

[4] R. Hemsworth, H. Decamps, J. Graceffa, B. Schunke, M. Tanaka, M. Dremel, A. Tanga, H.P.L. De Esch, F. Geli, J. Milnes, T. Inoue, D. Marcuzzi, P. Sonato, and P. Zaccaria, *Status of the ITER heating neutral beam system*, Nuclear Fusion **49** (2009), no. 4, 045006.

[5] Yu.I. Belchenko, G.I. Dimov, and V.G. Dudnikov, *A powerful injector of neutrals with a surface-plasma source of negative ions*, Nuclear Fusion **14** (1974), no. 1, 113–114.

[6] E. Speth, H.D. Falter, P. Franzen, U. Fantz, M. Bandyopadhyay, S. Christ, A. Encheva, M. Fröschle, D .Holtum, B. Heinemann, W. Kraus, A. Lorenz, Ch. Martens, P. McNeely, S. Obermayer, R. Riedl, R. Süss, A. Tanga, R. Wilhelm, and D. Wünderlich, *Overview of the RF source development programme at IPP Garching*, Nuclear Fusion **46** (2006), no. 6, S220–S238.

[7] R. S. Hemsworth, A. Tanga, and V. Antoni, *Status of the ITER neutral beam injection system*, Review of Scientific Instruments **79** (2008), no. 2, 02C109.

[8] R. Gutser, *Experiments and simulations for the dynamics of cesium in negative hydrogen ion sources for ITER N-NBI*, Ph.D. thesis, 2010.

[9] R. Gutser, U. Fantz, and D. Wünderlich, *Simulation of cesium injection and distribution in RF-driven ion sources for negative hydrogen ion generation*, Review of Scientific Instruments **81** (2010), no. 2, 02A706.

[10] J. P. Freidberg, *Plasma physics and fusion energy*, Cambridge University Press, 2007.

[11] C Gormezano et. al., *Chapter 6: Steady state operation*, Nuclear Fusion **47** (2007), no. 6, S285–S336.

[12] K.H. Berkner, R.V Pyle, and J.W Stearns, *Intense, mixed-energy hydrogen beams for CTR injection*, Nuclear Fusion **15** (1975), no. 2, 249–254.

[13] A. R. P. Rau, *The negative ion of hydrogen*, Journal of Astrophysics and Astronomy **17** (1996), no. 3-4, 113–145.

[14] Y. Okumura, Y. Fujiwara, A. Honda, T. Inoue, M. Kuriyama, K. Miyamoto, N. Miyamoto, K. Mogaki, A. Nagase, Y. Ohara, K. Usui, and K. Watanabe, *Development of a 500 keV, 22 A* D^- *ion source for the neutral beam injector for JT-60U*, Review of Scientific Instruments **67** (1996), no. 3, 1018–1020.

[15] E. Speth, M. Ciric, J.H. Feist, P. Frank, B. Heinemann, W. Kraus, F. Probst, R. Riedl, R. Trainham, O. Vollmer, and R. Wilhelm, *RF ion sources for fusion applications: design, development and performance*, Fusion Engineering and Design **46** (1999), no. 2-4, 383–388.

[16] Y Takeiri, O Kaneko, K Tsumori, Y Oka, K Ikeda, M Osakabe, K Nagaoka, E Asano, T Kondo, M Sato, and M Shibuya, *High-power and long-pulse injection with negative-ion-based neutral beam injectors in the Large Helical Device*, Nuclear Fusion **46** (2006), no. 6, S199–S210.

[17] A. Kojima, M. Hanada, Y. Tanaka, T. Inoue, K. Watanabe, M. Taniguchi, M. Kashiwagi, N. Umeda, H. Tobari, and L. R. Grisham and, *Achievement and improvement of the JT-60u negative ion source for JT-60 super advanced*, Review of Scientific Instruments **81** (2010), no. 2, 02B112.

[18] N. Umeda, J. Hiratsuka, A. Kojima, M. Ichikawa, M. Yoshida, H. Yamanaka, H. Tobari, K. Watanabe, and M. Kashiwagi, *Long pulse and high power density* H^- *ion beam acceleration for ITER*, AIP Conf. Proc. **1869** (2017), 030008.

[19] U. Fantz, C. Hopf, D. Wünderlich, R. Friedl, M. Fröschle, B. Heinemann, W. Kraus, U. Kurutz, R. Riedl, R. Nocentini, and L. Schiesko, *Towards powerful negative ion beams at the test facility ELISE for the ITER and DEMO NBI systems*, Nuclear Fusion **57** (2017), no. 11, 116007.

[20] V. Toigo et al., *The PRIMA test facility: SPIDER and MITICA test-beds for ITER neutral beam injectors*, New Journal of Physics **19** (2017), no. 8, 085004.

[21] M. Bacal, E. Nicolopoulou, and H. Douset, Proc. Int. Symp. Production and Neutralization of Negative Ions and Beams, **26** (New York), BNL, 1977.

[22] M. Bacal, *Physics aspects of negative ion sources*, Nuclear Fusion **46** (2006), no. 6, S250–S259.

[23] J. M. Wadehra and J. N. Bardsley, *Vibrational- and rotational-state dependence of dissociative attachment in e-H_2 collisions*, Phys. Rev. Lett. **41** (1978), no. 26, 1795–1798.

[24] J. N. Bardsley and J. M. Wadehra, *Dissociative attachment and vibrational excitation in low-energy collisions of electrons with H_2 and D_2*, Physical Review A **20** (1979), no. 4, 1398–1405.

[25] K. N. Leung, G. J. DeVries, W. F. DiVergilio, R. W. Hamm, C. A. Hauck, W. B. Kunkel, D. S. McDonald, and M. D. Williams, *RF driven multicusp H^- ion source*, Review of Scientific Instruments **62** (1991), no. 1, 100–104.

[26] J. Peters, *The HERA RF-driven multicusp H^- ion source*, AIP Conf. Proc. **925** (2007), 79.

[27] B. Rasser, J.N.M. Van Wunnik, and J. Los, *Theoretical models of the negative ionization of hydrogen on clean tungsten, cesiated tungsten and cesium surfaces at low energies*, Surface Science **118** (1982), no. 3, 697–710.

[28] G.D. Alton, *Semi-empirical mathematical relationships for electropositive adsorbate induced work function changes*, Surface Science **175** (1986), no. 1, 226–240.

[29] H. B. Michaelson, *The work function of the elements and its periodicity*, Journal of Applied Physics **48** (1977), no. 11, 4729–4733.

[30] W. M. Haynes, *CRC handbook of chemistry and physics, 93rd edition*, CRC Press, 2012.

[31] Ratko K. Janev, William D. Langer, Douglass E. Post, and Kenneth Evans, *Elementary processes in hydrogen-helium plasmas*, Springer Berlin Heidelberg, 1987.

[32] B. Heinemann, U. Fantz, W. Kraus, L. Schiesko, C. Wimmer, D. Wünderlich, F. Bonomo, M. Fröschle, R. Nocentini, and R. Riedl, *Towards large and powerful radio frequency driven negative ion sources for fusion*, New Journal of Physics **19** (2017), no. 1, 015001.

[33] P. McNeely and D. Wünderlich and, *Neutral depletion in an* H^- *source operated at high RF power and low input gas flow*, Plasma Sources Science and Technology **20** (2011), no. 4, 045005.

[34] L. Schiesko, P. McNeely, P. Franzen, and U. Fantz, *Magnetic field dependence of the plasma properties in a negative hydrogen ion source for fusion*, Plasma Physics and Controlled Fusion **54** (2012), no. 10, 105002.

[35] U. Fantz, L. Schiesko, and D. Wünderlich, *Plasma expansion across a transverse magnetic field in a negative hydrogen ion source for fusion*, Plasma Sources Science and Technology **23** (2014), no. 4, 044002.

[36] S. Lishev, L. Schiesko, D. Wünderlich, and U. Fantz, *Influence of the configuration of the magnetic filter field on the discharge structure in the RF driven negative ion source prototype for fusion*, AIP Conf. Proc. **1869** (2017), 030042.

[37] U. Fantz, P. Franzen, W. Kraus, M. Berger, S. Christ-Koch, M. Fröschle, R. Gutser, B. Heinemann, C. Martens, P. McNeely, R. Riedl, E. Speth, and D. Wünderlich, *Negative ion RF sources for ITER NBI: status of the development and recent achievements*, Plasma Physics and Controlled Fusion **49** (2007), no. 12B, B563–B580.

[38] L Schiesko, P McNeely, U Fantz, and P Franzen and, *Caesium influence on plasma parameters and source performance during conditioning of the prototype ITER neutral beam injector negative ion source*, Plasma Physics and Controlled Fusion **53** (2011), no. 8, 085029.

[39] U. Fantz, *Basics of plasma spectroscopy*, Plasma Sources Science and Technology **15** (2006), no. 4, S137–S147.

[40] M Berger, U Fantz, and S Christ-Koch and, *Cavity ring-down spectroscopy on a high power RF driven source for negative hydrogen ions*, Plasma Sources Science and Technology **18** (2009), no. 2, 025004.

[41] U. Fantz, B. Heinemann, D. Wünderlich, R. Riedl, W. Kraus, R. Nocentini, and F. Bonomo, *Towards 20 A negative hydrogen ion beams for up to 1 h: Achievements of the ELISE test facility (invited)*, Review of Scientific Instruments **87** (2016), no. 2, 02B307.

[42] W. Kraus, U. Fantz, B. Heinemann, and D. Wünderlich, *Concepts of magnetic filter fields in powerful negative ion sources for fusion*, Review of Scientific Instruments **87** (2016), no. 2, 02B315.

[43] B. Heinemann, U. Fantz, W. Kraus, D. Wünderlich, F. Bonomo, M. Froeschle, I. Mario, R. Nocentini, R. Riedl, and C. Wimmer, *Latest achievements of the negative ion beam test facility ELISE*, Fusion Engineering and Design **to be published**.

[44] R. Gutser, C. Wimmer, and U. Fantz, *Work function measurements during plasma exposition at conditions relevant in negative ion sources for the ITER neutral beam injection*, Review of Scientific Instruments **82** (2011), no. 2, 023506.

[45] Yu. Belchenko, G. Abdrashitov, A. Ivanov, A. Sanin, and O. Sotnikov, *High voltage holding in the negative ion sources with cesium deposition*, Review of Scientific Instruments **87** (2016), no. 2, 02B120.

[46] P. W. Van Amersfoort, Y. Tong, and E. H. A. Granneman, *A model for the stationary cesium coverage on a converter surface in a cesium seeded hydrogen discharge*, Journal of Applied Physics **58** (1985), no. 6, 2317–2325.

[47] C. Wimmer, A. Mimo, M. Lindauer, and U. Fantz, *Improved understanding of the Cs dynamics in large* H^- *sources by combining TDLAS measurements and modeling*, AIP Conf. Proc. (to be published).

[48] D. Wünderlich, Private Communication (2017).

[49] Landolt-Börnstein, *Group IV physical chemistry*, Springer, 2008.

[50] U. Fantz, R. Gutser, and C. Wimmer, *Fundamental experiments on evaporation of cesium in ion sources*, Review of Scientific Instruments **81** (2010), no. 2, 02B102.

[51] R. Friedl and U. Fantz, *Fundamental studies on the Cs dynamics under ion source conditions*, Review of Scientific Instruments **85** (2014), no. 2, 02B109.

[52] S. Cristofaro, R. Friedl, and U. Fantz, *Simultaneous measurements of work function and H density including caesiation of a converter surface*, AIP Conf. Proc. **1869** (2017), 030036.

[53] S. König and U. Fantz, *Untersuchungen der Eigenschaften cäsierter Oberflächen in Wasserstoff Plasmen*, 2007.

[54] L. Schiesko, C. Hopf, P. Franzen, W. Kraus, R. Riedl, and U. Fantz and, *A study on backstreaming positive ions on a high power negative ion source for fusion*, Nuclear Fusion **51** (2011), no. 11, 113021.

[55] J. P. Biersack and J. F. Ziegler, *The stopping and range of ions in solids*, Ion Implantation Techniques, Springer Berlin Heidelberg, 1982, pp. 122–156.

[56] C. Hopf, A. von Keudell, and W. Jacob, *Chemical sputtering of hydrocarbon films*, Journal of Applied Physics **94** (2003), no. 4, 2373–2380.

[57] M Balden and J Roth, *New weight-loss measurements of the chemical erosion yields of carbon materials under hydrogen ion bombardment*, Journal of Nuclear Materials **280** (2000), no. 1, 39–44.

[58] Erhard W. Rothe and Richard B. Bernstein, *Total collision cross sections for the interaction of atomic beams of alkali metals with gases*, The Journal of Chemical Physics **31** (1959), no. 6, 1619–1627.

[59] C.K. Birdsall, *Particle-in-cell charged-particle simulations, plus Monte Carlo collisions with neutral atoms, PIC-MCC*, IEEE Transactions on Plasma Science **19** (1991), no. 2, 65–85.

[60] S. Ma, R.D. Sydora, and J.M. Dawson, *Binary collision model in gyrokinetic simulation plasmas*, Computer Physics Communications **77** (1993), no. 2, 190–206.

[61] John Bradshaw Taylor and Irving Langmuir, *The evaporation of atoms, ions and electrons from caesium films on tungsten*, Physical Review **44** (1933), no. 6, 423–458.

[62] M. Fröschle, R. Riedl, H. Falter, R. Gutser, and U. Fantz, *Recent developments at IPP on evaporation and control of caesium in negative ion sources*, Fusion Engineering and Design **84** (2009), no. 2-6, 788–792.

[63] G. A. Bird, *The DSMC method*, CreateSpace Independent Publishing Platform, 2013.

[64] D. Wünderlich, C. Wimmer, and R. Friedl, *A collisional radiative model for caesium and its application to an RF source for negative hydrogen ions*, AIP Publishing LLC, 2015.

[65] G.H. Dieke, *The molecular spectrum of hydrogen and its isotopes*, Journal of Molecular Spectroscopy **2** (1958), no. 1-6, 494–517.

[66] U. Fantz and C. Wimmer, *Optimizing the laser absorption technique for quantification of caesium densities in negative hydrogen ion sources*, Journal of Physics D: Applied Physics **44** (2011), no. 33, 335202.

[67] C. Wimmer, U. Fantz, E. Aza, J. Jovović, W. Kraus, A. Mimo, and L. Schiesko, *Investigation of plasma parameters at BATMAN for variation of the Cs evaporation asymmetry and comparing two driver geometries*, AIP Conference Proceedings **1869** (2017), 030021.

[68] B. Heinemann, M. Fröschle, H.D. Falter, U. Fantz, P. Franzen, W. Kraus, R. Nocentini, R. Riedl, and B. Ruf, *Upgrade of the BATMAN test facility for H- source development*, AIP Conf. Proc. **1655** (2015), 060003.

[69] E. Speth and NBI-Team, *Development of powerful RF plasma sources for present and future NBI systems*, Plasma Science and Technology **6** (2004), no. 1, 2135–2140.

[70] P. Franzen, U. Fantz, D. Wünderlich, B. Heinemann, R. Riedl, W. Kraus, M. Fröschle, B. Ruf, and R. Nocentini, *Progress of the ELISE test facility: results of caesium operation with low RF power*, Nuclear Fusion **55** (2015), no. 5, 053005.

[71] C.F. Barnett, J.A. Ray, E. Ricci, M.I. Wilker, E.W. McDaniel, E.W. Thomas, and H.B. Gilbody, *Atomic data for controlled fusion research*, Tech. report, feb 1977.

[72] C. D. Child, *Discharge from hot cathods*, Physical Review (Series I) **32** (1911), no. 5, 492–511.

[73] F. Bonomo, M. Barbisan, U. Fantz, A. Hurlbatt, I. Mario, and D. Wünderlich, *Overview of the beam physics investigation at the ELISE test facility*, AIP Conf. Proc. (to be published).

[74] K. Ikeda, M. Kisaki, H. Nakano, K. Nagaoka, M. Osakabe, S. Kamio, K. Tsumori, S. Geng, and Y. Takeiri, *Study of back streaming ion using a slot-type grounded grid in hydrogen negative-ion source*, AIP Conf. Proc. **1869** (2017), 050004.

[75] D. Marcuzzi, P. Agostinetti, M. Dalla Palma, F. Degli Agostini, M. Pavei, A. Rizzolo, M. Tollin, and L. Trevisan, *Detail design of the beam source for the SPIDER experiment*, Fusion Engineering and Design **85** (2010), no. 10-12, 1792–1797.

[76] P. McNeely, S. V. Dudin, S. Christ-Koch, and U. Fantz, *A Langmuir probe system for high power RF-driven negative ion sources on high potential*, Plasma Sources Science and Technology **18** (2008), no. 1, 014011.

[77] A. Tanga, M. Bandyopadhyay, and P. McNeely, *Measurement of ion flow in a negative ion source using a mach probe*, Applied Physics Letters **84** (2004), no. 2, 182–184.

[78] S. Dietrich, *Messungen von Plasmaparameterprofilen mittels der Janus-Sonde*, Technology Meeting (Ringberg), IPP, Technology Division (2007).

[79] Ciric D., *PerMag Manual*, Abingdon: UKAEA Fusion/Euratom Association, Culham Science Centre) (2007).

[80] P. Franzen, L. Schiesko, M. Frschle, D. Wnderlich, and U. Fantz, *Magnetic filter field dependence of the performance of the RF driven IPP prototype source for negative hydrogen ions*, Plasma Physics and Controlled Fusion **53** (2011), no. 11, 115006.

[81] D. Wünderlich, Private Communication (2015).

[82] ANSYS, *Engineering simulation & 3-d design software*, http://www.ansys.com.

[83] R. Nocentini, Private Communication (2015).

Acknowledgements

It's now time to express my gratitude to all the people who gave me the possibility of carrying on this work and who supported me during these past three years.

First of all I would like to thank **Prof. Dr.-Ing. Ursel Fantz**, for her outstanding supervision during the entire period of my PhD at the Max-Plank-Institut für Plasmaphysik: thanks to her experience I had the possibility of growing as a scientist in this wonderful community.

I would like to thank **Prof. Dr. Achim Wixforth** for having accepted to be the second reviewer of my PhD thesis.

A big "thank you" goes to **Dr. Christian Wimmer**, who led me through the world of negative ion sources by spending a lot of time beside me during the operations at the test facilities and by answering to my endless (sometimes silly, sometimes tricky) questions about Cs and Cs diagnostics. I thank him for numerous discussions we had: they strongly stimulated my interest for the topic and my desire to dive deeper into the scientific challenges of Cs dynamics.

I received a strong support for the computational side of my work by **Dr. Dirk Wünderlich**, who helped me in some frustrating moments in which I was lost inside the CsFlow3D code. The discussions with him, thanks also to the friendly environment, always led me to the light at the end of the tunnel of thousands of lines of code... I would like to thank him also for having given me the possibility of joining the operation at the ELISE test facility: it was very important to develop an experimental feeling of the source behaviour. I enjoyed this not only as a scientist, but also as a person.

I would like then to thank **Dr. Loïc Schiesko**, operator at the BATMAN test facility: he had always the right answer to my questions during the BATMAN operation, even before I asked them...

My work would not have been possible without the support of the many other people of the group: I would like to mention here all the "neighbours of the corridor", i.e. **Dr. Federica Bonomo, Dr. Niek Den Harder, Dr. Christian Hopf, Dr. Andrew Hurlbatt, David Rittich, Dr. Eleni Aza, Isabella Mario and Mauricio Montellano**, together with all the people of the ITED division.

The nice thing of science is that science is not only work but also fun: I sincerely enjoyed every minute in which I was following the operations at the test facilities, in

which I was sharing the happiness for having reached the target of the day, of the week or of the month, for having understood also only 0.001% more of the physics behind, as well as the less happy moments in which something was not working properly (many exclamations are still resounding in my mind, such as *"Ach, so ein Käse"* or *"Ach klump!"*).

I cannot forget the help of my friends from the university studies in Padova, now spread all around Europe. In particular I would like to mention **Sofia Cristofaro** and **Antonio Pimazzoni**, who are also following the way of plasma physics. Their presence, their support, no matter if nearby or further away is always in my mind as well as in my heart and so it will be forever.

All this experience would not have been possible without the love of all my family back in Italy. A very huge thank you to **my parents, my brother and his wife**: you were always with me and cheering for me in the many good moments I had as well as in the sporadic sad ones.

Last but not least: many great "thanks!" to all my "old" friends back in Italy and my "new" friends here in Germany. I cannot avoid saying "a huge thank you" to my friends from the German course, which I attended in the evening after work. They were fundamental for recharging my batteries after some stressful days and they, the *monkey group*, were and are always beside me: thank you!